12-2018

Discrete Element Modeling of the Grading- and Shape-Dependent Behavior of Granular Materials

Zhengshou Lai

Clemson University, zlai@clemson.edu

Follow this and additional works at: https://tigerprints.clemson.edu/all_dissertations

Discrete element modeling of the grading- and shape-dependent behavior of granular materials

A Dissertation
Presented to
the Graduate School of
Clemson University

In Partial Fulfillment
of the Requirements for the Degree
Doctor of Philosophy
Civil Engineering

by
Zhengshou Lai
December 2018

Accepted by:
Dr. Qiushi Chen, Committee Chair
Dr. Ronald D. Andrus
Dr. Stephen Moysey
Dr. Hai Huang

Abstract

Granular materials, such as sand, biomass particles, and pharmaceutical pills, are widespread in nature, industrial systems, and our daily life. Fundamentally, the bulk mechanical behavior of such materials is governed by the physical and morphological features of and the interactions among constituent particles at the microscopic scale. From a modeling standpoint, the particle-based discrete element method (DEM) has emerged as the most prevalent numerical tool to model and study the behavior of granular materials and the systems they form. A critical step towards an accurate and predictive DEM model is to incorporate those physical and morphological features (e.g., particle size, shape, and deformability) pertaining to the constituent particles.

The main objective of this dissertation is to approach an accurate characterization and modeling of the grading- and shape-dependent behavior of granular materials by developing DEM models that incorporate realistic physical and morphological features of granular particles. Revolving around this objective, three studies are presented: image-based particle reconstruction and morphology characterization, grading and shape-dependent shearing behavior of rigid-particle systems, and granular flow of deformable irregular particles.

The first study presents a machine learning and level-set based framework to reconstruct granular particles and to characterize particle morphology from X-ray computed tomography (X-ray CT) imaging of realistic granular materials. Images containing detailed microstructure information of a granular material are obtained using the X-ray CT technique. Approaches such as the watershed method in two dimensions (2D) and the combined machine learning and level set method in three dimensions (3D) are then utilized and

implemented to segment X-ray CT images and to numerically reconstruct individual particles in the granular material. Based on the realistic particle shapes, particle morphology is characterized by descriptors including aspect ratio, roundness, circularity (2D) or sphericity (3D). The particle shapes or morphology provide important constraints to develop DEM models with particle physical and morphological features conforming to the specific granular material of interest.

In the second study, DEM models incorporated with realistic particle sizes and shapes are developed and applied to study the shearing behavior of sandy soils. The particle sizes and shapes are obtained from realistic samples of JSC-1A Martian regolith simulant. Irregular-shape particles are represented by rigid clumps based on the domain overlapping filling method. The effects of particle shape irregularity on the shearing behavior of granular materials are investigated through direct shear tests, along with the comparisons from spherical particles with or without rolling resistance. The micro-mechanisms of shape irregularity contributing to the shear resistance are identified.

The last study investigates the effects of particle deformability (e.g., compression, deflection or torsion), together with particle sizes and shapes, on the granular flow of flexible granular materials. A bonded-sphere DEM model is implemented with the capability of embodying various particle sizes and irregular shapes, as well as capturing particle deformability. This approach is then applied to simulate and study the behavior of flexible granular materials in cyclic compression and hopper flow tests. The effects of particle size, shape and deformability on the bulk mechanical behavior are investigated on the basis of the DEM simulation results. The importance of particle deformability to the DEM simulations of flexible granular materials is demonstrated.

Dedication

To my beloved family.

Acknowledgments

First and foremost, I would like to express my sincerest gratitude to my advisor, Dr. Qiushi Chen, for his continuous support to my Ph.D. study with great patience, motivation, and encouragement. His guidance has helped me to develop my academic and research skills, and more importantly, to become a critical and independent researcher. I have been imperceptibly influenced by his rigorous academic behavior, which will be a great treasure in my future research life.

Besides my advisor, I would like to thank the rest of my dissertation committee: Dr. Ronald D. Andrus, Dr. Stephen Moysey, and Dr. Hai Huang, for their insightful comments and inspiring questions which stimulated me to enhance my research from various perspectives. I value the knowledge learned from the classes of Dr. Andrus, and thank Dr. Moysey for generously providing me the access and guidance to the X-ray computed tomography machine. Dr. Huang offered me the precious internship opportunity in Idaho National Laboratory, during which the research work has become a main part of this dissertation. Also, I would like to thank Dr. C. Hsein Juang for serving as a committee member of my comprehensive exam and dissertation proposal defense.

My sincere thanks also go to my mentor Dr. Yidong Xia and collaborator Dr. Tyler Westover for their guidance and support during my internship in Idaho National Laboratory. Yidong has also been a great friend with whom I have shared and discussed my unconstrained-crazy research ideas quite a lot.

During the four years of Ph.D. study, I have been financially supported by the U.S. Department of Energy's Office of Energy Efficiency and Renewable Energy (EERE) under the

During these years, I have also been blessed by all the wonderful friends in my life: college friends and their family, lab and office mates, church friends, landlord and his family at Idaho Falls, visiting scholars, et. al., whom I cannot exhaustively name here, but with whom the friendship I will cherish forever. Especially, I would like to thank Prof. Linchong Huang, who recommended me to my current Ph.D. advisor, who has been a great teacher and friend since my undergraduate time, and from whom there are tons of knowledge to learn regarding the way of life.

Finally, I would like to express my deepest gratitude to the most important people in my life: my family. My parents and my sister have been supporting me spiritually throughout my Ph.D. time, as well as my entire life; and they are always my most powerful and reliable backing. My wife, Yi Pan, has been a great life companion for more than five years with her endless love and trust. Our lovely son, Eric, was born four years ago; and three years later, we had our cute daughter, Eleanora. Their arrival brought us great happiness as well as anxiousness, which has been stimulating us to learn and improve as being parents ever since. Lastly, I would like to thank my parents in law for their kind support, trust, and frequent visits to help us.

I am indebted to all the wonderful people in my life who have ever supported me or witnessed my growing up till this moment. Deep debt of gratitude is noted here but far beyond words.

Table of Contents

List of Tables

List of Figures

xiii

Chapter 1

Introduction

1.1 General background

Granular materials, such as sand, biomass particles, and pharmaceutical pills, are widespread in nature, industrial systems, and our daily life. A few examples of granular materials can be seen in Figure 1.1. Many engineering problems and applications involve the handling and processing of granular materials, such as the construction of a foundation on granular soil deposit, slope reinforcement, biomass comminution and pelletization, granular hopper flow, just to name a few. To understand and accurately predict the bulk mechanical behavior of granular materials is a challenging but essential endeavor to design and improve the handling methods of these problems.

(a) Mojave Mars simulant   (b) Pinewood chips   (c) Pharmaceutical pills

Figure 1.1: Examples of granular materials.

The solid phase of granular materials is composed of discrete particles of various sizes and complex-irregular shapes. The motions of and interactions among these constituent particles at the microscopic scale, as an assembly, forms the bulk mechanical behavior of granular materials. Therefore, the behavior of such materials is fundamentally governed by physical and morphological features, such as particle size, shape, interparticle friction, stiffness, and flexibility, etc., pertaining to the constituent particles. Due to the discrete and complex nature of granular materials, a general theoretical description of their bulk mechanical behavior remains unavailable. The particle-based discrete element method (DEM) (Cundall and Strack, 1979), from the modeling standpoint, has emerged as the most prevalent numerical tool to model granular materials and to understand their bulk behavior from the micro-mechanics among the constituent particles.

In order to approach accurate modeling of granular materials based on DEM, it is critical to precisely incorporate the particle physical and morphological features into the DEM model. With regard to the particle morphology features, two of the most salient impact factors are the particle sizes (i.e., grading) (Bui et al., 2005; Igwe et al., 2007; Vangla and Latha, 2015) and the particle shapes (Santamarina and Cho, 2004; Cho et al., 2006; Rousé et al., 2008) as observed from laboratory experiments. To study or predict the behavior of granular materials, it is necessary to take into account the effects of particle grading and shape irregularity. This dissertation will thus focus on capturing and understanding the grading- and shape-dependent behavior of granular materials from the micro-mechanics among the constituent particles based on DEM.

1.2   Scope & objectives

The research efforts of incorporating different particle sizes and irregular shapes into a DEM model and investigating their effects on the bulk mechanical behavior of granular materials have been on the rise recently. Although different particle sizes and different types of non-spherical particle shapes have been implemented in previous studies (Sitharam and

Nimbkar, 2000; Wood and Maeda, 2008; Ding et al., 2014; Liu et al., 2014b; Li et al., 2014; Dai et al., 2015; Zhou et al., 2016; Estrada, 2016; Garcia et al., 2009; Torskaya et al., 2014), most of them were artificially created for research purposes and may not necessarily reflect the sizes and shapes of realistic particles of a specific granular material. The questions then arise as: (1) *how to accurately characterize the particle sizes and shapes of a realistic granular material*; (2) *how to effectively incorporate realistic particle sizes and shapes into a DEM model*; and (3) *how do the particle sizes and shapes, together with other physical properties such as particle flexibility, affect the bulk behavior of this specific granular material*?

By addressing these questions, the main objective of this dissertation is to approach an accurate characterization and modeling of the grading- and shape-dependent behavior of granular materials by developing DEM models that incorporate realistic physical and morphological features of granular particles. Revolving around this objective, three main studies will be conducted: (1) image-based particle reconstruction and morphology characterization (see Chapter 3), (2) grading and shape-dependent shearing behavior of rigid-particle systems (see Chapter 4), and (3) granular flow of deformable irregular particles (see Chapter 5 and Chapter 6). The specific tasks include:

1. An extensive literature review of current approaches for characterizing particle sizes and shapes based on imaging techniques, and representing irregular-shape and deformable particles in DEM models.

2. Development of a framework to reconstruct particle shapes from realistic samples of granular materials based on imaging techniques.

3. Quantitative characterization and analysis of particle morphology using different shape descriptors, including aspect ratio, roundness, circularity (2D) or sphericity (3D).

4. Development of DEM models with the incorporation of realistic particle sizes and shapes.

5. To investigate the effects of particle size, shape, along with the particle deformability,

3

on the behavior of granular materials in different situations including direct shear, cyclic compression, and hopper flow tests.

6. To study the capability of using the rolling resistance model to compensate for the effects of particle shape irregularity.

7. To identify the importance of particle deformability to the DEM simulations of flexible granular materials.

1.3 Dissertation organization

This dissertation is organized into seven chapters. The introduction is presented in Chapter 1, followed by Chapter 2 that presents the DEM basics and review. The main chapters (3, 4, 5 and 6) are self-contained studies with literature reviews on its own related research topics and have been or will be published in technical journals. The summary of these main chapters is listed as following:

Chapter 3 presents a machine learning and level set based framework to segment X-ray computed tomography (X-ray CT) images and numerically reconstruct individual particles of a granular material. The proposed framework is applied to reconstruct three-dimension realistic particle shapes of the Mojave Mars Simulant soil, and quantitative morphology analyses are also performed.

Chapter 4 studies the grading and shape-dependent sharing behavior of rigid-particle systems. X-ray CT technique is exploited to obtain particle imaging of the JSC-1A Martian regolith simulant, from which particle sizes and shapes are characterized and used to develop numerical clump (e.g., rigid particle) based DEM models. The effects of particle shape irregularity on the shearing behavior are investigated through direct shear simulations with comparisons from spherical particles with or without rolling resistance.

Chapter 5 conducts the DEM modeling of complex-shape, deformable particles with a case study of flexible pinewood chips. A bonded-sphere DEM model is implemented with the capability of embodying various particle sizes, irregular shapes, and capturing particle

deformability. The mechanical behavior of bulk pinewood chips in cyclic compression test is studied.

Chapter 6 applies the previous bonded-sphere DEM model to a practical problem, granular hopper flow tests. Different simulation scenarios, including spherical particles, rigid-irregular particles, and deformable-irregular particle of different shapes and stiffness, are considered. The effects of particle size, shape, as well as particle deformability, on the hopper flow behavior are investigated.

As a conclusion of this dissertation, Chapter 7 summarizes the main findings of this dissertation, discusses the limitations of the current work, and outlines the possible directions of future research.

Chapter 2

Discrete element method basics and review

This chapter presents a brief introduction and review of the discrete element method (DEM). The intention is to introduce the main components and basic computational workflow of a DEM model, providing necessary background information to the research presented in this dissertation.

2.1   Overview

DEM is a particle-based numerical model that is particularly suitable for describing the mechanical behavior of bulk granular materials. It was first proposed by Cundall and Strack (1979) for the analysis of geotechnical materials. Since then, DEM has been applied to model all kinds of granular materials and to simulate the problems ranging from solids handling to powder flowing in a variety of different engineering branches (Cleary, 2009; Tijskens et al., 2003; O'Sullivan, 2011). In DEM, all individual particles in the bulk granular material are explicitly modeled and a DEM model directly captures the interactions between particles and tracks the motions of each particle. The bulk behavior of a granular material is

presented as an assembly of the actions (i.e., the interactions and motions) of all constituent particles.

As a particle-based numerical model, DEM exhibits several advantages compared to the classical continuum theory-based numerical models. First, it bypasses the phenomenological constitutive models for describing the bulk behavior of a granular material within a representative volume (Andrade and Avila, 2012; Andrade et al., 2012a; Guo and Zhao, 2016). Second, it is straightforward for the DEM to simulate the problems involving large deformation or material failure, such as granular flow, penetration, or strain localization (Chen, 2011). The major drawback of DEM is also obvious. As DEM tracks the interactions and motions of all particles, DEM simulations are quite computationally expensive, which makes it difficult to scale up (Liu and Hrenya, 2014; Berger and Hrenya, 2014). Nevertheless, with the advent of computer hardware and parallel capabilities, the DEM has become an increasingly powerful numerical tool that can provide valuable information of and shed lights upon the microscopic behavior of granular materials, which is often difficult or impossible to obtain from classical continuum-based numerical models or from physical experiments.

2.2 Key components of DEM

2.2.1 Basic elements

In general, there are two types of basic elements in a DEM model: particles and boundaries. The basic elements are assumed to be rigid but can have overlaps with each other. A particle is a body that has a closed surface. It may be represented by a simple geometry (e.g., sphere or ellipsoid) or a composition of several simple geometries that make up the body surface (see further discussions in Section 2.3). A review on the particle geometric representations can be found in (Zhong et al., 2016). Particles have mass and their motion (i.e., position, velocity, and acceleration) is always tracked during a DEM simulation. Boundaries are also referred to as walls in the DEM literature. They may as well be represented by simple geometries (e.g., triangles) or their combinations, but they

do not necessarily have closed surfaces. Boundaries do not have mass and their position and velocity are usually prescribed to provide the desired constraints to the particles in the model.

2.2.2 Contacts and contact models

Contacts describe the interactions between basic elements. Contact occurs when the surfaces of two basic elements overlap with each other (to model collisions), or when the surfaces are within a specified distance (to model long-range bond or cohesion). Detecting the contacts between basic elements is a mathematical geometry problem and is one of the most time-consuming parts of a DEM simulation. One important task associated with contact detection is to characterize the contact geometric features, which are needed by a contact model to calculate the contact forces and moments. The contact features may include the overlapping (or indentation) distance, relative shear displacement, contact point, contact branch vectors, and so on.

Contact models are used to calculate the contact forces and moments between the two elements in contact. Commonly used contact models include the linear elastic model (Cundall and Strack, 1979), the rolling resistance model (Jiang et al., 2005), the Hertz-Mindlin model (Hertz, 1882; Mindlin, 1953; Di Renzo and Di Maio, 2005), and the linear parallel bond model (Potyondy and Cundall, 2004). The formulation of these contact models will be presented in Section 2.4.

2.2.3 Newton-Euler equations of motion

In DEM, the motion of a particle can be described by the Newton-Euler equations of motion. For any arbitrarily-shaped particle, the Newton-Euler equations of motion are

written as

$$ma = F \tag{2.1}$$

$$I\alpha + \omega \times L = M \tag{2.2}$$

where m is the mass of the particle; I is the inertia tensor of the particle; a and α are the translational and rotational acceleration; F and M are the overall external forces and moments acting on the particle; ω is the vector of the angular velocities about the principal axes. Herein, the variable in bold-symbol indicates a vector or a tensor. For spherical particles, the Newton-Euler equations of motion reduce to

$$ma = F \tag{2.3}$$

$$I\alpha = M \tag{2.4}$$

In order to resolve the motion of each particle, all the forces and moments acting on the particle need to be evaluated and summed, which may include gravity, damping, contact forces and moments, and prescribed external forces and moments. Herein, the damping refers to the global damping, which is sometimes (artificially) introduced in a DEM model to facilitate energy dissipation and enhance a quasi-static simulation (Chung, 2006; Itasca Consulting Group, Inc, 2014). There is another type of damping called local damping, which is usually incorporated into a contact model as dash-pot forces to account for the realistic energy dissipation due to particle interactions.

2.2.4   Time integration

To fully resolve the particle motion (e.g., the position and velocity) governed by Equation 2.1 and Equation 2.2 involves the time integration scheme, where the second-order Velocity Verlet algorithm (Verlet, 1967) is commonly adopted. For spherical particles, suppose that the current state is indexed by time t and the time increment to the next state

9

is Δt, Velocity Verlet algorithm first calculates the particle velocities at time $t+\Delta t/2$ by

$$v^{t+\Delta t/2} = v^t + a^t \Delta t/2 \tag{2.5}$$

$$\omega^{t+\Delta t/2} = \omega^t + \alpha^t \Delta t/2 \tag{2.6}$$

where v and ω are translational and angular velocities, respectively. The superscripts (e.g., t and $\Delta t/2$) indicate the time indexes. Then, the position and orientation of the particle at time $t+\Delta t$ are calculated as

$$x^{t+\Delta t} = x^t + v^{t+\Delta t/2} \Delta t \tag{2.7}$$

$$\theta^{t+\Delta t} = \theta^t + \omega^{t+\Delta t/2} \Delta t \tag{2.8}$$

where x is the vector of position and θ is the vector of orientation. Correspondingly, the translational velocity and angular velocity at time $t + \Delta t$ are updated by

$$v^{t+\Delta t} = v^{t+\Delta t/2} + a^{t+\Delta t/2} \Delta t/2 \tag{2.9}$$

$$\omega^{t+\Delta t} = \omega^{t+\Delta t/2} + \alpha^{t+\Delta t/2} \Delta t/2 \tag{2.10}$$

For non-spherical particles, the original Newton-Euler equations of motion cannot be simplified, and the calculation of the orientations and angular velocity will be much more complicated. A more detailed discussion on the time integration for non-spherical particles will not be included here but can be found in the work of Chung (2006) and the PFC user manual (Itasca Consulting Group, Inc, 2014).

2.2.5 Critical timestep

The time integration based on the second-order Velocity Verlet algorithm is numerically stable only when the time increment being used is less than a threshold value, i.e. the critical timestep (Otsubo et al., 2017). If a time increment greater than the critical timestep

is used, particles may move too much in one increment, which will result in spuriously infinite overlapping (i.e., abnormally large contact forces).

A summary and empirical assessment of different approaches to estimate the critical timestep for DEM simulations can be found in Otsubo et al. (2017). Basically, there are two categories of approaches to estimate the critical timestep: the oscillation period of a single degree of freedom system (SDOF) based approaches (Cundall and Strack, 1979; Hart et al., 1988), and the Rayleigh wave speed based approaches (Thornton, 2000; Li et al., 2005b). The former approaches consider the DEM system to be consist of rigid bodies connected by springs, while the latter ones consider the particles themselves to be springs.

In the category of the SDOF-based approaches, Cundall and Strack (1979) proposed the following expression to estimate the critical timestep Δt_{crit}

$$\Delta t_{\text{crit}} = \min(\sqrt{m/k^{\text{tran}}}, \sqrt{I_i/k_i^{\text{rot}}}) \tag{2.11}$$

where m is the mass of the particle; I_i is the moment of inertia of the particle; k^{tran} and k_i^{rot} represent the translational and rotational stiffness, and the subscript i indicates the index of principal components.

In the category of the Rayleigh wave speed based approaches, Li et al. (2005b) proposed that

$$\Delta t_{\text{crit}} = \frac{\pi R \sqrt{\rho/G}}{0.1631\nu + 0.8766} \tag{2.12}$$

where R is the average particle radius; ρ is the particle density; G the particle shear modulus; and ν the Poisson's ratio of the particle.

2.2.6 Computational workflow

DEM-based numerical simulations require cyclic calculations. Figure 2.1 shows the workflow and calculations that are involved in one typical cycle of a DEM simulation.

The workflow and calculations for one DEM cycle can be summarized as follows:
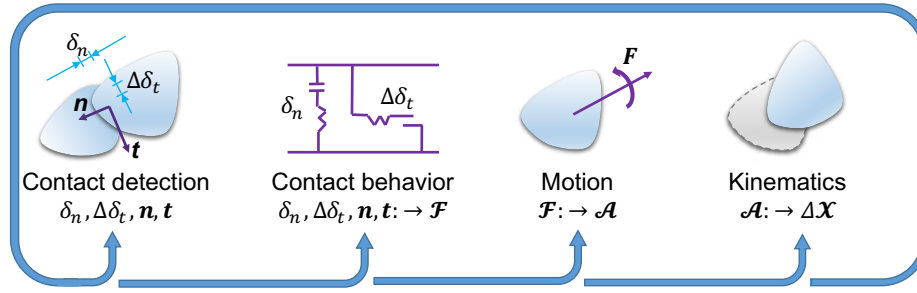
Figure 2.1: The workflow and calculations that are involved in one typical cycle of a DEM simulation. $\mathcal{F}$, $\mathcal{A}$ and $\mathcal{X}$ indicate the general forces, accelerations, and positions of a particle.

1. At the current state, the positions and velocities of all particles are known: based on the geometries of all particles, identify the inter-particle contacts and evaluate contact features;

2. Calculate the external forces and moments of all particles, while the contact forces and moments are calculated based on selected contact models and the corresponding contact features;

3. Calculate the motion (i.e., the accelerations) of all particles;

4. Update the positions and velocities of all particles following the selected time integration scheme.

2.3 Particle representation

There are basically two groups of methods to represent an irregular particle in DEM (Zhong et al., 2016): single-particle method and composite-particle method.

2.3.1 Single-particle method

The single-particle method utilizes closed geometries to represent particle shapes. Many single-particle-based DEM models have been proposed and developed with the adoption of some specific closed geometries, such as cylinder (Feng et al., 2017b), polyhedron

(or polygon in 2D) (Nassauer et al., 2013; D'Addetta et al., 2002), ellipsoid (or ellipse in 2D) (Lin and Ng, 1997; Ting et al., 1993), superquadrics (Williams and Pentland, 1992; Podlozhnyuk et al., 2017), Non-Uniform Rational Basis Spline (NURBS) (Andrade et al., 2012a), as well as their combinations (e.g., poly-ellipsoid (Peters et al., 2009; Zhang et al., 2018a)).

Each of these methods has its own advantages and limitations. The application of the cylinder-based or ellipsoid-based DEM models is limited, due to the particular particle shapes they can represent. The superquadric can be considered as an extension of the ellipsoid and can be used for modeling of spheres, ellipsoids, cylinder-like and box(dice)-like particles by varying the shape parameters. It is more flexible by being able to model larger variations of particle shapes, but also more computationally expensive than the ellipsoid-based DEM models. The polyhedron- (or polygon in 2D) based DEM model is able to replicate arbitrary particle shapes. The accuracy of the shape represented by polyhedron depends on the number of faces in a polyhedron, whereas a large number of faces would hinder the computational efficiency. Moreover, polyhedron can rarely replicate a smooth particle shape. The NURBS based granular element method, developed by Andrade et al. (2012a), is advantageous to replicate general and smooth particle shapes, whereas it is computationally expensive compared to the polyhedron-based DEM.

Recently, Kawamoto et al. (2016) developed another novel type of single-particle-based DEM, which utilizes the level set (LS) method to represent particles. The LS-DEM seamlessly utilizes the level set data of realistic particle shapes characterized from X-ray computational tomography and is computationally efficient. One issue with the LS-DEM is high memory consumption, which somewhat limits its application on large particulate systems.

2.3.2 Composite-particle method

In a composite-particle method, a particle is represented by compositions of simple geometries (usually spheres in 3D or circles in 2D (Das, 2007; Shi et al., 2015)). This group

of methods is advantageous to implementation for that the contact detection and resolution algorithms for the simple geometries can be effortlessly exploited. It should be noted that the accuracy of particle shape represented by compositions of simple geometries depends on the amount of the simple geometries, and a large number of simple geometries would lead to great computational expense though. Nonetheless, the composite-particle method (especially with spheres as the base elements) is currently the most prevalent method to model irregular particles and is supported in most commercial or open-source DEM packages such as PFC (Itasca Consulting Group, Inc, 2014) and LIGGGHTS (Kloss et al., 2012).

There are three options to represent a composite particle (Shi et al., 2015): the domain overlapping filling method, the domain non-overlapping filling method, and the boundary filling method, as shown in Figure 2.2 with discs being used as the base elements, for instance. The composite particle generated by domain overlapping filling requires the least number of particles and is, therefore, the most computationally efficient. The domain non-overlapping filling method can be promoted to model physics-based particle deformation (e.g., compression, deflection or distortion) or breakage. The boundary filling method, depending on the size of filling elements, could provide a better representation of surface roughness.

(a) Domain overlapping filling   (b) Boundary filling   (c) Domain non-overlapping filling
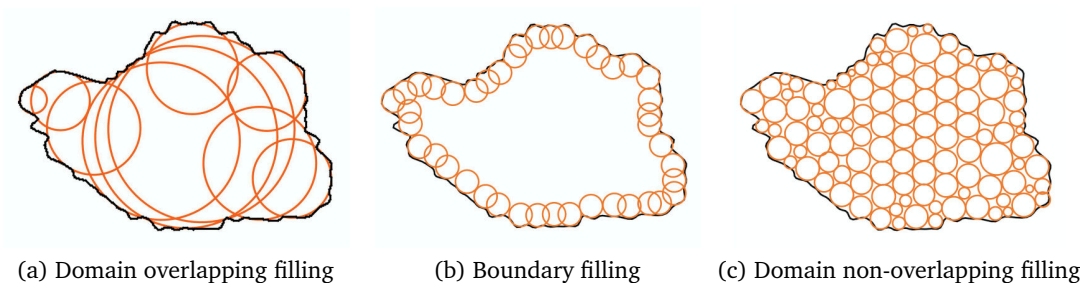
Figure 2.2: A schematic illustration of the three options to represent a composite particle with discs (modified after Shi et al. (2015)).

2.4 Contact models

A DEM contact model is normally comprised of springs, dash-pots, and sliders to describe the force-displacement behavior at the contact, where the springs account for normal and tangential forces, the dash-pots account for local damping, and the sliders account for shear failure. The formulation of contact models that will be used in this dissertation is presented in this section.

2.4.1 Linear elastic model

A linear elastic model generally consists of two elastic springs, two dash-pots, and a slider, as shown schematically in Figure 2.3.
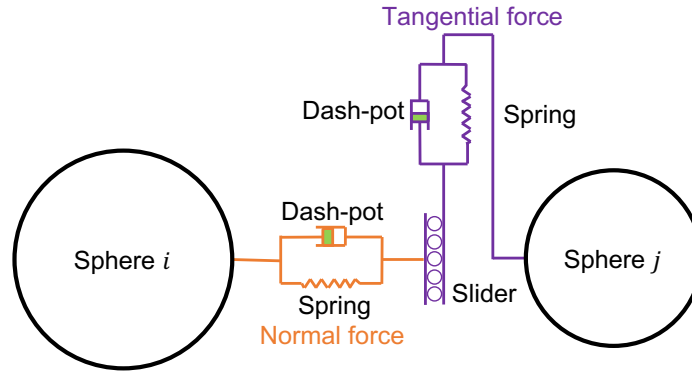
Figure 2.3: Schematic diagram of linear elastic model (adopted from (Chung, 2006)).

The contact forces F are calculated from two parts: the normal force F_n and the shear (or tangential) force F_s

$$F = F_n + F_s = F_n n_n + F_s n_s \tag{2.13}$$

where n_n and n_s are the unit vectors denoting the direction of the normal and the shear force, respectively; F_n and F_s are the magnitudes of corresponding contact forces. Assuming the relative displacement increment at the contact during a timestep Δt is given by its components $\Delta\delta_n$ (compression as a positive) and $\Delta\delta_s$, the contact law for a simple linear

15

model with local damping updates the contact forces through (Cundall and Strack, 1979; Itasca Consulting Group, Inc, 2014)

$$F_n = F_n^0 + k_n \Delta \delta_n - \eta_n \sqrt{\bar{m} k_n} \dot{\delta}_n \tag{2.14}$$

$$F_s = \min(F_s^0 + k_s \Delta \delta_s - \eta_s \sqrt{\bar{m} k_s} \dot{\delta}_s, \mu_c F_n) \tag{2.15}$$

where F_n^0 and F_s^0 are the normal and the shear forces at the beginning of the current timestep, respectively; k_n and k_s are the corresponding stiffness; η_n and η_s are the corresponding damping coefficients; $\dot{\delta}_n$ and $\dot{\delta}_s$ are the relative normal and shear velocity; μ_c is the contact friction coefficient; and $\bar{m} = m_i m_j / (m_i + m_j)$ is the effective mass of particles i and j associated with the contact, while $\bar{m} = m_i$ for the case of particle-boundary contact.

2.4.2   Rolling resistance model

The rolling resistance model is built upon the linear elastic model by adding a term of rolling resistance moment to the contact moment. The formulation to calculate the additional rolling resistance moment can be written as Iwashita and Oda (1998); Jiang et al. (2005); Itasca Consulting Group, Inc (2014)

$$M = \min(M^0 + k_r \Delta \theta_b, \mu_r \bar{R} F_n) \tag{2.16}$$

where M^0 is the contact moment at the beginning of the current timestep; $\Delta \theta_b$ is the relative bending-rotation increment; μ_r is the rolling resistance coefficient; k_r is the rolling resistance stiffness defined as:

$$k_r = k_s \bar{R}^2 \tag{2.17}$$

where $\bar{R}$ is the contact effective radius defined as $\bar{R} = R_i R_j / (R_i + R_j)$, in which R_i and R_j are the radii of the contact particles. If one side of the contact is a wall, the corresponding radius $R_j \to \infty$.

This model uses a simplified formulation for the rolling kinematics, and the particle

size effects on the rolling resistance are implicitly incorporated in the rolling stiffness term. The interested reader is referred to Luding (2008); Wang et al. (2015) for examples of improved and more advanced rolling resistance models.

2.4.3   Hertz-Mindlin model

The Hertz-Mindlin model is a complete frictional contact model based upon the Hertz theory (Hertz, 1882) for contact normal forces and the Mindlin theory (Mindlin, 1953) for contact tangential forces. It takes into account the stiffness variation due to the change of contact areas during the collision of two elastic spheres.

Similar to the linear elastic model, the Hertz-Mindlin model also consists of two springs, two dash-pots, and a slider. There are, however, two major differences. First, the normal and shear stiffness in the Hertz-Mindlin model are functions of the contact overlapping distance. Second, the normal contact force in the Hertz-Mindlin model is calculated via the cumulative overlapping distance, while the linear elastic model uses either the cumulative or incremental overlapping distance. To update the contact forces, the Hertz-Mindlin model follows

$$F_n = k_n \delta_n - \eta_n \sqrt{\bar{m} k_n} \dot{\delta}_n \tag{2.18}$$

$$F_s = \min(F_s^0 + k_s \Delta \delta_s - \eta_s \sqrt{\bar{m} k_s} \dot{\delta}_s, \mu_c F_n) \tag{2.19}$$

where δ_n is the cumulative overlapping distance, while k_n and k_s are calculated as (Di Renzo and Di Maio, 2005):

$$k_n = \frac{4}{3} \bar{E} \sqrt{\bar{R} \delta_n} \tag{2.20}$$

$$k_s = 8 \bar{G} \sqrt{\bar{R} \delta_n} \tag{2.21}$$

in which

$$\frac{1}{\bar{E}} = \frac{(1 - v_i^2)}{E_i} + \frac{(1 - v_j^2)}{E_j} \tag{2.22}$$

$$\frac{1}{\bar{G}} = \frac{2(2 - v_i)(1 + v_i)}{E_i} + \frac{2(2 - v_j)(1 + v_j)}{E_j} \tag{2.23}$$

where $\bar{E}$ and $\bar{G}$ are the effective Young's modulus and shear modulus of the particles in contact; E_i is the Young's modulus and v_i is the Poisson's ratio of the ith particle.

2.4.4   Linear parallel bond model

The linear parallel bond model describes the contact behavior of two bonded particles, as shown schematically in Figure 2.4.
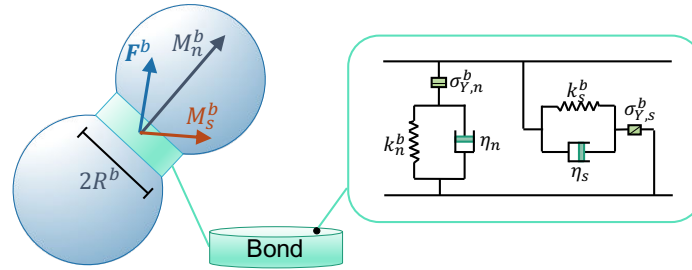
Figure 2.4: Sketch of bonded particles and rheological components of the bond behavior. Symbols in the figure will be explained in the text.

In the linear parallel bond model, the bond between two spheres is assumed to be a cylinder of finite radius and thickness. Each point in the bond is imposed by two linear elastic springs providing normal and shear resistances, respectively. The overall bonding force and moment are the integral of the normal and shear stresses at a cross-section of the

18

bond, which can be calculated as (Potyondy and Cundall, 2004)

$$\Delta F_n^b = k_n^b A \Delta \delta_n \tag{2.24}$$

$$\Delta F_s^b = k_s^b A \Delta \delta_s \tag{2.25}$$

$$\Delta M_n^b = k_s^b J \Delta \theta_n \tag{2.26}$$

$$\Delta M_s^b = k_n^b I \Delta \theta_s \tag{2.27}$$

where F_n^b, F_s^b, M_n^b and M_s^b are the bond normal force, shear force, twisting moment, and swinging moment, respectively; δ_n, δ_s, θ_n, and θ_s are the relative normal displacement, shear displacement, twisting rotation, and swinging rotation between the two bonded spheres, respectively; A, I, and J are the area, moment of inertia, and polar moment of inertia of the bond (i.e., the circular cross-section with radius R^b), respectively; and Δ indicates the increment of each variable in each time step. It should be pointed out that, while the damping is not included in the current formulation, damping terms similar to those in the linear elastic model can be incorporated in a straightforward manner.

The bonded-sphere model is also capable of modeling the particle breakage behavior. As an example of a common bond breakage criterion, it can be assumed that a bond would break if the maximum normal or shear stress at the bond exceeds the corresponding normal or shear strength. In the linear parallel bond model, both the normal force and swinging moment contribute to the normal stress, while both the shear force and twisting moment contribute to the shear stress. In this regard, the bond breakage criterion can be written as

$$\sigma_{\max}^b = \frac{F_n^b}{A} + \frac{M_s^b R^b}{I} < \sigma_{Y,n}^b \tag{2.28}$$

$$\tau_{\max}^b = \frac{F_s^b}{A} + \frac{M_n^b R^b}{J} < \sigma_{Y,s}^b \tag{2.29}$$

where $\sigma_{Y,n}^b$ and $\sigma_{Y,s}^b$ are the normal and shear strength, respectively.

2.5 Model calibration

As most of the contact parameters in a DEM model are difficult if not impossible to be measured directly from physical tests, a calibration process is often needed to obtain the contact parameters for a specific material of interest. There are some researches available on the procedures to calibrate contact parameters for a DEM model (Plassiard et al., 2009; Chehreghani et al., 2017; Coetzee, 2017). Usually, the calibration process is accomplished by performing parametric studies on each of contact parameters and selecting values of the contact parameters with which the DEM simulation can reproduce the benchmark matrices of laboratory experiments. Commonly used laboratory experiments for calibration of DEM parameters include compression test, direct and ring shear test, and angle of repose test. Descriptions of these tests can be found in (Schulze, 2008; Coetzee, 2017).

There are some challenges and problems associated with the model calibration. First, to obtain reasonable and realistic contact parameters via calibration, it is necessary that the setup and procedures in the DEM models are to the most extent similar to those in the laboratory experiments. However, in order to get the DEM simulations performed within affordable computational resources, adjustments or tolerances in the particle size, shape or testing speed may exist in a DEM model. As a result, the calibrated contact parameters may deviate from their actual values to some degree. In addition, the contact features and contact models are usually quite simple and conceptual compared to the actual complex contact behavior. The physical meaning of the contact parameters may be lost due to the use of conceptualized contact features and contact models. Lastly, as pointed out in (Coetzee, 2017), the solution of contact parameters might not be unique since all contact parameters may affect the results of a DEM simulation in a complex and highly nonlinear manner. There is no guarantee that the contact parameters for a material calibrated for one experiment will be workable for another. In this regard, it would be necessary to perform the calibration with one experiment and validate the calibration results via another.

2.6 Summary

A brief review of DEM has been presented in this chapter. A general DEM model involves the following components: basic elements, contacts and contact models, Newton-Euler equations of motion, time integration (i.e., the Velocity Verlet algorithm). Timestep is a critical parameter affecting the numerical stability of DEM simulations and the approaches to estimating the critical timestep have been discussed. The general computational workflow of DEM simulations has also been described.

The single-particle methods and composite-particle methods are two basic groups of methods to represent an irregular particle in DEM. Their corresponding advantages and limitations have been discussed. Later in this dissertation, the composite-particle method will be employed following the domain overlapping and domain non-overlapping filling schemes. The former scheme considers rigid particles (see Chapter 4), while the latter one provides particles the ability to deform or break (see Chapter 5 and Chapter 6).

This chapter also presented the formulations of four commonly used contact models: linear elastic model, rolling resistance model, Hertz-Mindlin model, and linear parallel bond model. While the linear elastic model is a simplistic model, it can still reproduce the most characteristic behaviors of a material when properly calibrated(Zhao et al., 2018a). The Hertz-Mindlin model has a similar form as the linear elastic model but takes into account the stiffness variation at different particle overlapping distances. The rolling resistance model can be applied on spheres to replicate the effects of particle shape irregularity (comparisons will be reported in Chapter 4). The linear parallel bond model is used to characterize the contacts between base particles, which are bonded together to form a deformable-irregular particle (the model will be used in the studies presented in Chapter 5 and Chapter 6).

As most of the contact parameters are difficult if not impossible to be measured directly from physical tests, a calibration process is often needed to obtain the contact parameters. The general approach for model calibration, as well as the challenges and problems associated with the calibration, has been also discussed in this chapter.

Chapter 3

Reconstructing granular particles from X-ray computed tomography using the TWS machine learning tool and the level set method

X-ray computed tomography (CT) has emerged as the most prevalent technique to obtain three-dimension morphological information of granular geomaterial. A key challenge in using the X-ray CT technique is to faithfully reconstruct particle morphology based on the discretized pixel information of CT images. In this work, a novel framework based on the machine learning technique and the level set method is proposed to segment CT images and reconstruct particles of granular geomaterials. Within this framework, a feature-based machine learning technique termed Trainable Weka Segmentation (TWS) is utilized for CT image segmentation, i.e., to classify material phases and to segregate particles in contact. This is a fundamentally different approach in that it predicts segmentation results based

on a trained classifier model that implicitly includes image features and regression functions. Subsequently, an edge-based level set method is applied to approach an accurate characterization of the particle shape. The proposed framework is applied to reconstruct three-dimension realistic particle shapes of the Mojave Mars Simulant. Quantitative accuracy analysis shows that the proposed framework exhibits superior performance over the conventional watershed-based method in terms of both the pixel-based classification accuracy and the particle-based segmentation accuracy. Using the reconstructed realistic particles, particle size distribution is obtained and validated against experiment sieve analysis. Quantitative morphology analysis can also be performed, showing promising potentials of the proposed framework in characterizing granular geomaterials.

3.1   Introduction

The study of particle morphological features of granular geomaterials, including their form, sphericity, roundness, and roughness, has been a subject of interest in the geotechnical engineering and geomechanics community for decades. These morphological features can help researchers and engineers understand the forming, weathering and aging process of geomaterials (Gilkes and Suddhiprakarn, 1979; Papoulis et al., 2004). They are also among the fundamental and the most salient factors that govern the material's macroscopic properties and engineering behavior, such as compressibility, shear strength, and critical state parameters (Santamarina and Cho, 2004; Guo and Su, 2007; Tsomokos and Georgiannou, 2010; Stark et al., 2014; Zheng et al., 2017). Moreover, the understanding of the link between particle morphology and its engineering behavior is of importance to design and optimize innovative geomaterials, such as bio-improved and bio-cemented granular soils (Tagliaferri et al., 2011; Cheng et al., 2013; DeJong et al., 2013; Dadda et al., 2017; Gleaton et al., 2018).

Experimental techniques commonly used to obtain the morphological features of granular geomaterials include photography (Zheng et al., 2017), scanning electron mi-

croscopy (Cox and Budhu, 2008), and X-ray computed tomography (CT) (Desrues et al., 2010). The first two techniques provide two-dimension (2D) morphological information (i.e., 2D images) that can be used to approximate or infer three-dimension (3D) morphological features, e.g., through a virtual 3D surface method (Mollon and Zhao, 2013b) or through enhancing the illusion of the depth of 2D images (Zheng and Hryciw, 2017b). The X-ray CT, on the other hand, can be used to directly obtain 3D morphological information, and therefore, has been the most prevalent technique in recent years (Matsushima et al., 2009; Garboczi, 2011; Andò et al., 2013; Hashemi et al., 2014; Vlahinić et al., 2014; Viggiani et al., 2015; Zhou et al., 2018). The particle-level morphological information can be integrated into numerical methods, such as the discrete element method (DEM) (Cundall and Strack, 1979), to develop more realistic and predictive numerical models for granular geomaterials (Matsushima et al., 2009; Andrade et al., 2012c; Zheng and Hryciw, 2017a; Lai and Chen, 2017).

3.1.1 Motivation of the proposed framework

Reconstructing particle morphology from discretized pixel information of X-ray CT images poses three main challenges. The first challenge is to classify pixel in a raw CT image into different material constituents or phases (e.g., soil particles, voids). Thresholding is a commonly used method for such a purpose in image processing, which has been successfully applied to separate objects from the background (Bruchon et al., 2013). The performance and effectiveness of the thresholding method, however, is greatly complicated by various factors, such as the nonstationary and correlated noise, ambient illumination, busyness of gray levels within the object and its background, inadequate contrast, and object size not commensurate with the scene (Sezgin and Sankur, 2004). Granular geomaterial is typically a composition of various minerals, organic matters, fluids, and internal voids. Each of the constituents has its intrinsic X-ray attenuation, leading to a large variance of pixel intensity in raw CT images (Ketcham and Carlson, 2001). In addition, the perturbation of tomography environment, the practical scanning procedure and the limitation of CT optical apparatus

could bring in significant noises that further aggravate the intensity variance (Sleutel et al., 2008). As such, there is oftentimes no clear demarcation between the pixel intensity of different phases in geomaterials, which makes phase classification using the thresholding method very challenging. Some more advanced energy-based techniques for constituents classification, such as the graph cut and the region-based level set algorithms, are sensitive to the selection of weights on the various terms in the energy functional (Al-Kofahi et al., 2010). These weights are usually tuned beforehand by the developer via trial and error, and can only achieve reasonable results for certain types of images.

The second challenge is to accurately identify particle boundaries and segregate particles in contact. Several well-known methods for object segregation include the watershed method (Matsushima et al., 2009), the concave curvature segmentation method (Hobson et al., 2009; Wang et al., 2012), the edge detection method (Gao and Chae, 2010; Vlahinić et al., 2014), and the region growing method (Hashemi et al., 2014). Each of these methods has its strengths and limitations, and sometimes, several methods are used in combination to achieve better performance. The watershed method is perhaps the most widely used method but has the over-segmentation issue (Meijering, 2012). Its performance, to a great extent, depends on well-defined markers that are typically difficult to determine. The concave curvature segmentation method examines the curvature of the shape boundary and draws segmenting *split line* through the *split points* with a concave curvature, thus to split the contacting particles at the point of contact (Hobson et al., 2009). This method requires *a prior* shape information and might not be applicable to particles with concave surfaces as it would mistakenly split a particle if a concave surface is detected. The edge detection-based method utilizes some filters, such as the difference of Gaussian or the Laplacian of Gaussian, to identify object boundaries. These filters alone usually do not produce definitive object boundaries, but may provide useful cues to be used in subsequent algorithms, such as the edge-based level set method (Gao and Chae, 2010; Vlahinić et al., 2014). The edge-based level set method depends upon well-defined edge indicator, and its performance is sensitive to the initialization and model parameters.

The last challenge is to approach an accurate characterization of the particle shape based on the discretized pixel matrix of CT images. The marching cubes (MC) method proposed by Lorensen and Cline (1987) is a popular isosurface algorithm to reconstruct particle surface. However, in most literature, the MC method operates on binarized images for surface reconstruction and the reconstructed surfaces generally have artificial stair steps (Zhao and Wang, 2016). Hence, some smoothing manipulations are necessary to remove the jagged stair steps (Gibson, 1998). A more accurate approach is to utilize the edge-based level set method, which is capable of achieving a sub-pixel accuracy of the object boundary (Liu et al., 2016). As aforementioned, the edge-based level set method suffers from the edge indicator, initialization, and model parameter issues when handling image segmentation.

In this paper, a novel framework is developed to identify and reconstruct realistic 3D particle shapes from discretized pixel information of X-ray CT images. The proposed framework takes a fundamentally different approach compared to previous works in that a trainable machine learning technique is innovatively integrated with the edge-based level set method. The machine learning technique is utilized to segment raw CT images of granular geomaterials, i.e., to classify different constituents and to segregate particles in contact. In the machine learning process, the segmentation algorithms are not explicitly programmed. Instead, the method predicts segmentation results based on the weighted combination of various image features at different image scales (Jaccard, 2015). The image features and regression functions are implicitly encoded in the classifier model and are determined through a training process. The machine learning-based method, with well-trained classifier model (e.g. the feature weights and regression functions), can provide logical and knowledge-based image segmentation results comparable to experienced engineers or to human's recognition and perception. It has already brought in some successful applications of image segmentation in the biology and medical areas (Sommer and Gerlich, 2013; Avendi et al., 2016). Once the raw images are segmented, edge indicators can be evaluated from the processed images. A 3D edge-based level set method is then developed to approach an accurate shape representation of real particles.

3.2 Overview of the framework

Figure 3.1 shows a schematic illustration of the proposed framework. In this figure, key components of the methodology are shown in the top row and the expected outputs are listed in the bottom row. The framework starts with a specimen of granular soil scanned using an X-ray CT scanner to produce a set of 3D raw CT images. A machine learning tool termed Trainable Weka Segmentation (TWS) is then utilized to classify image pixels and segment particles in contact. The outputs of the TWS-based segmentation are probability maps showing the probability of the pixels belonging to a specified class (e.g., solid or void). Using the probability maps as inputs, a 3D edge-based level set method is implemented to capture particle boundaries and reconstruct realistic particles. These particles can be used for subsequent analysis such as characterizing shapes or particle size distributions. In the following sections, the TWS-based segmentation, the level set method and the particle shape analysis will be presented in details.
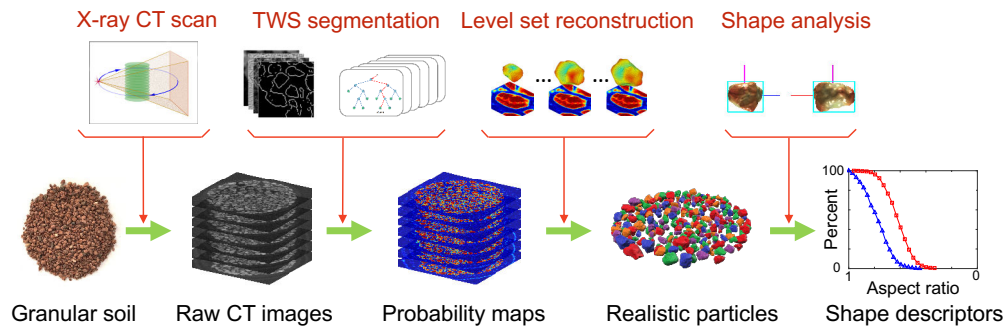
Figure 3.1: Schematic illustration of the proposed framework. The top row includes key components of the methodology and the bottom row includes the expected outputs. TWS stands for Trainable Weka Segmentation.

3.3 Image segmentation by the TWS machine learning tool

In this section, the Trainable Weka Segmentation (TWS) (Arganda-Carreras et al., 2017) is introduced for image segmentation. TWS is a pixel-based image classification and segmentation tool, where each pixel in an image is treated as an individual object that

possesses a vector of image features. A combination of image features is then used to classify a pixel into different classes. The basic idea of the machine learning-based approach is to regress the weights of different image features through a training process using manual annotations of image features. The result of the training process is a trained classifier model that can be applied to segment other similar image data.

TWS leverages the state-of-the-art machine learning algorithms provided in the data mining and machine learning toolkit Waikato Environment for Knowledge Analysis (Weka) (Hall et al., 2009). TWS acts as a bridge between the image processing and machine learning toolkit, where it extracts the features of an image (e.g., an X-ray CT image) and converts them into the format that is expected by the Weka toolkit. By default, TWS uses random forest (RF) as the machine learning algorithm. In a recent study by Fernández-Delgado et al. (2014), RF is shown to yield best overall performance and is recommended for new problems involving machine learning.

3.3.1   Decision tree and random forest

Random forest is built on an ensemble of decision trees. Decision trees are a nonparametric supervised learning method used for classification and regression. The goal is to create a flowchart-like structure that predicts the outcome of a target object (e.g., an X-ray image pixel) by learning simple decision rules inferred from the data features (e.g., various image features).

Figure 3.2 shows an example of a decision tree. In this example, there are 100 objects taken as training inputs, where each object possesses 3 features. 40 of the 100 objects are labeled as the foreground objects and 60 of them are labeled as the background objects. At the first level of division, the 100 objects are split into two groups based on the value of their second feature. The selection of a feature for the division is based on the information entropy theory (Quinlan, 1986), and the feature that achieves the most information gain after the division will be selected. According to the test results on the second feature, the 100 objects are classified into two groups. For instance, 10 of the 40 foreground objects fall

into the first group as their second feature is smaller than 0.5, while 30 of them fall into the second group as their second feature is greater than 0.5. The second and third level of division follows the same strategy. Eventually, the 100 objects are classified into 8 groups. For each of the 8 groups, if the foreground objects are dominating that group, it is considered as a foreground group and vice versa. The decision tree is constructed during the training process to determine the division parameters.

Once the decision tree is constructed, it can be used to predict the outcome of a new object. A new object will go through the branches of the decision tree following values of its features, eventually falling into an end group. The label of that group is the predicted outcome of the new object.
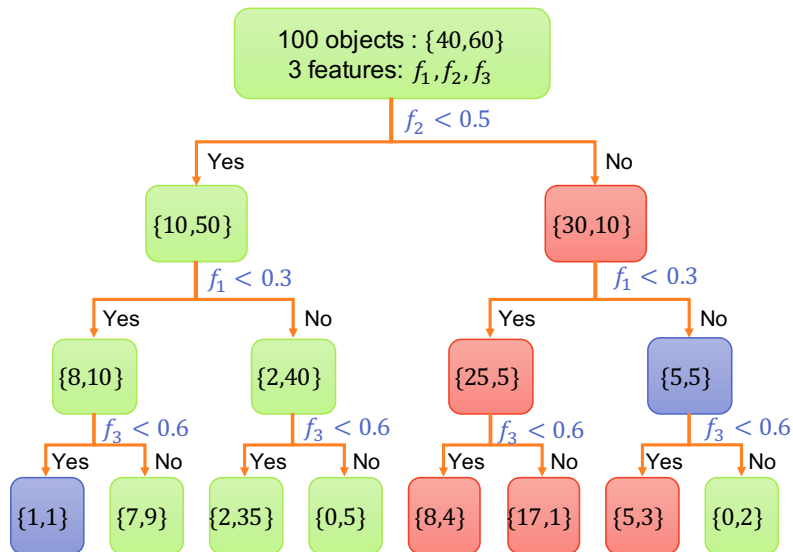
Figure 3.2: Example of a decision tree with 3 levels of division. The features and division parameters are determined during the training process.

A single decision tree has the issue of over-fitting and is sensitive to the input data. Random forest is an ensemble of decision trees that can mitigate such disadvantages. Assuming that a training sample contains N objects and each object has M features, a decision tree can be constructed using a random subset of the N objects with a random subset of the M features. By repeating this process, one can obtain a set of decision trees.

The prediction of a new object is based on the overall votes of all decision trees. Figure 3.3 shows an example of the random forest and its prediction strategy.
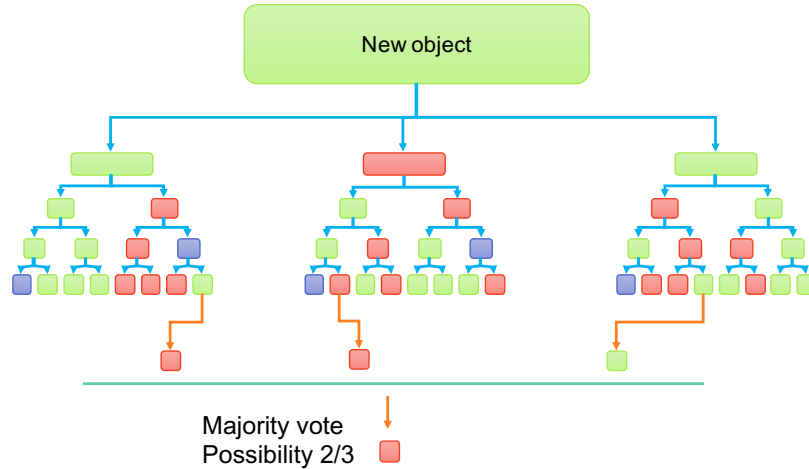
Figure 3.3: Example of a random forest consisting of 3 decision trees (modified from (Jaccard, 2015)).

3.3.2 Image features

When applying the random forest algorithm to segmenting X-ray CT images, the objects are image pixels and the features are image features determined by the user. In this section, selected image features for segmentation are presented. Table 3.1 summarizes various image features grouped by their purpose that can be included in a classifier model. In this table, the noise reduction aims to mitigate the negative impact of intensity noises, e.g., those resulting from the CT scanning system. The texture filter is used to extract texture information. The edge indicator is used to detect object boundaries. Membrane detector is specialized in identifying membrane-like structures of a certain size and thickness.

Table 3.1: Various image features and the corresponding purpose in the classifier model.

Image features	Purpose
Gaussian blur, Bilateral filter, Anisotropic diffusion, Kuwahara, Lipschitz	Noise reduction
Minimum, Maximum, Median, Variance, Entropy, Structure tensor	Texture filter
Laplacian, Hessian, Sobel filter, Difference of Gaussian, Gabor	Edge indicator
Membrane projection	Membrane detector

A detailed explanation of different image features can be found in Arganda-Carreras et al. (2017). Five of the image features from Table 3.1 are selected for this study, and they are briefly explained in this section.

Gaussian blur convolves an image with a Gaussian kernel distribution. It mitigates the noise and smooths the image. The standard deviation controls the shape of the Gaussian kernel, and a larger standard deviation increases the *blur* effect. Performing Gaussian blur with n different standard deviations results in a vector of n Gaussian blur features.

Sobel filter is to approximate the gradient of an image using a finite difference scheme. In practice, the Sobel filter is usually applied after a prior Gaussian blur. n Gaussian blur gives a vector of n Sobel filter features.

Hessian calculates the second derivatives of an image and results in a Hessian matrix at each pixel. The module, trace, determinant, first eigenvalue, second eigenvalue, orientation, Gamma-normalized square eigenvalue difference, and the square of Gamma-normalized eigenvalue difference will be used as Hessian features. A prior Gaussian blur is also applied before the Hessian operation. n Gaussian blur gives a vector of $8n$ Hessian features.

Difference of Gaussians calculates two Gaussian blur images from the original image and subtracts one from the other. Performing Difference of Gaussians with n different standard deviations gives a vector of $n(n-1)/2$ difference of Gaussians (DoGs) features.

Membrane projection first convolves an image with a set of hardcoded matrix kernel. The original matrix kernel is in $n \times n$ size, with the middle m columns set as 1s, and the remaining elements set as 0s. Then, the matrix kernel is rotated by 6 degrees up to a total rotation of 180 degrees, giving 30 kernels. The sum, mean, standard deviation, median, maximum and minimum of the 30 images are taken as the membrane projections features. The membrane-like structures in an image stand out after membrane projections.

An illustration of combining various images features into a classifier model is shown in Figure 3.4. It should be noted that including more image features does not necessarily yield better segmentation results as more features require more training inputs to achieve a desirable classifier. Also, more image features in the classifier mean increased computational expenses. It is found in this work that these five image features yield satisfactory segmentation results.
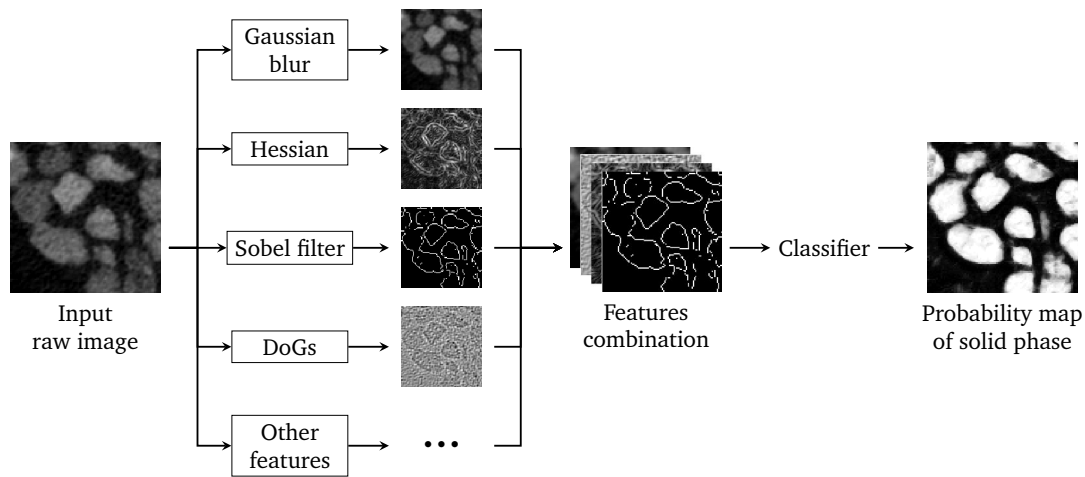
Figure 3.4: An illustration of combining various images features into the classifier model in machine learning-based image segmentation process.

3.3.3 Implementation of TWS for X-CT image segmentation

In this work, the process of using TWS to segment X-CT images are implemented in MATLAB. TWS is available as a plugin of Fiji (https://fiji.sc/). To be able to invoke Fiji and TWS methods in MATLAB, it is necessary to first install the Fiji-MATLAB interface *MIJ* (available from http://bigwww.epfl.ch/sage/soft/mij/). After installing the *MIJ* and adding the corresponding path into the MATLAB working path, the methods of TWS can be imported and invoked using MATLAB scripts. The interested reader is referred to the TWS user manual (available as the supplementary document of (Arganda-Carreras et al., 2017)) for more details of the TWS methods.

The workflow of the machine learning-based image segmentation is summarized in

Figure 3.5. The workflow consists of two main components: training classifier and applying classifier. In the training process, the raw X-CT images and their corresponding manually labeled images are required as inputs. The output is a trained classifier, where the parameters in each decision tree are obtained. By applying the trained classifier to new X-CT images, the labels of each pixel in the new images can be predicted.
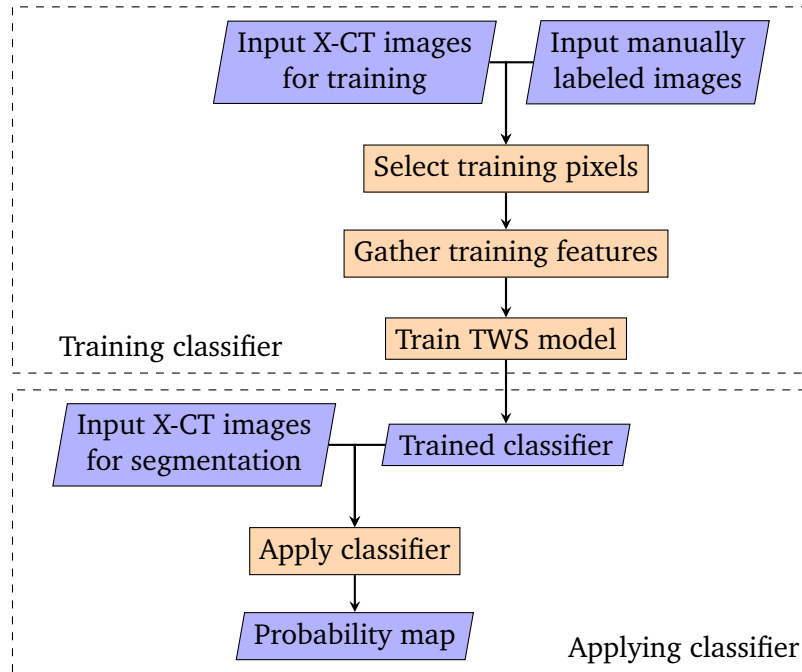
Figure 3.5: The workflow of the X-CT image segmentation via TWS machine learning technique.

To manually label an image, the values of each pixel are set to either 1 or 0, indicating whether it belongs to the constituent the labeled image represents. An example set of input images is shown in Figure 3.6. In this example, the image is intended to be classified into two phases (e.g., the solid phase and void phase as it is the case of this work). Two labeled images are required with one for the solid phase and one for the void phase. For the labeled image of the solid phase, the solid pixels are set to 1s, while the remaining pixels are set to 0s. To facilitate the training process and to reduce the workload of manual labeling, the TWS allows subset pixels of the raw image to be labeled and used as training inputs. After input of raw and labeled images, training features are gathered and the classifier is trained.
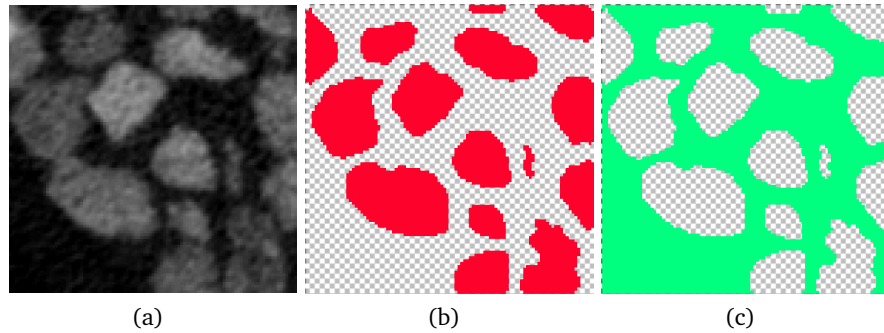
Figure 3.6: An example set of input images for training classifier: (a) raw image, (b) the labeled image of the solid phase, and (c) the labeled image of the void phase. The pixels rendered by red and green color in the labeled images (b) and (c) are set to 1s, whereas the pixels rendered by the black-white pattern are set to 0s.

After the classifier is trained, the subsequent process is to apply the trained classifier to segment new CT images. TWS provides two types of results, i.e., a label matrix and a probability map. A label matrix consists of integer values for all pixels in the image, i.e., 1s indicating the pixels belong to the constituent the label matrix represents, and 0s indicating otherwise. A probability map is a map of probability values indicating the likelihood of a pixel belonging to a particular constituent and will be adopted in this work. Edge indicators will be evaluated based on the probability map and will be used for the subsequent level set method. Also, it is worth noting that though only two constituents (solid and void) are considered in this work, the implemented TWS technique is applicable to segment multiple classes of constituents.

3.4 The level set method for shape characterization and reconstruction

The probability maps from machine learning-based image segmentation are used as inputs for particle shape characterization and reconstruction using the level set method (Osher and Sethian, 1988). In this work, the edge-based level set method is adopted. The original formulation proposed by Li et al. (2005a, 2010) is applied to 3D particles, and a

new scaling coefficient is introduced to the edge indicator function. It should be noted that a 3D version of the Li et al. (2005a) formulation has also been previously implemented by Sun et al. (2011a,b), where the authors proposed a semi-implicit integration scheme and used the level sets to determine the 3D medial axes of pore microstructures.

3.4.1 Energy functional

The shape (or boundary) of a particle can be characterized by a closed surface in 3D (or a contour in 2D). The level set method aims to capture this closed surface using an auxiliary function termed the level set function, where the closed surface is defined as the zero level set, written as

$$\Gamma = \{(x, y, z) \in \Omega | \phi(x, y, z) = 0\} \tag{3.1}$$

where ϕ is the level set function; (x, y, z) are the spatial coordinates; Ω is the domain of interest and Γ is the closed surface (i.e., the boundary of the particle). Conventionally, the level set function ϕ is assumed to take positive values inside the region delimited by Γ and negative values outside.

When applying the level set method to identify the particle boundary, the level set function ϕ is evolved by minimizing an appropriate energy functional, denoted as $\mathcal{F}(\phi)$. In this work, the following formulation proposed by Li et al. (2010) is adopted

$$\mathcal{F}(\phi) = \mu \mathcal{R}(\phi) + \lambda \mathcal{L}(\phi) + \nu \mathcal{A}(\phi) \tag{3.2}$$

where $\mathcal{R}(\phi)$ is the distance regularization term; $\mathcal{L}(\phi)$ and $\mathcal{A}(\phi)$ are the external energy related to the surface curvature and the inner volume, respectively; $\mu > 0$, $\lambda > 0$ and $\nu \in R$ are the weighting coefficients. A positive ν value drives the surface Γ inwards, while a

negative value drives Γ outwards. The energy terms are given by

$$\mathcal{R}(\phi) = \frac{1}{2} \int_{\Omega} (\|\nabla\phi\| - 1)^2 d\Omega \tag{3.3}$$

$$\mathcal{L}(\phi) = \int_{\Omega} g(I)\delta(\phi)\|\nabla\phi\| d\Omega \tag{3.4}$$

$$\mathcal{A}(\phi) = \int_{\Omega} g(I)H(-\phi) d\Omega \tag{3.5}$$

where H is the Heaviside function; δ is the Dirac delta function; $\|\cdot\|$ is the Euclidean norm; $g(I)$ is the edge indicator function defined by

$$g(I) := \frac{1}{1 + c\|\nabla I\|^2} \tag{3.6}$$

where I is the image matrix, and ∇ is the gradient operator. In this work, a scaling coefficient c is introduced to the conventional formulation of the edge indicator. In practice, it is found that this coefficient c can singularize the edge indicator (as shown in Figure 3.7), thus stabilize and facilitate the convergence of level set evolution.
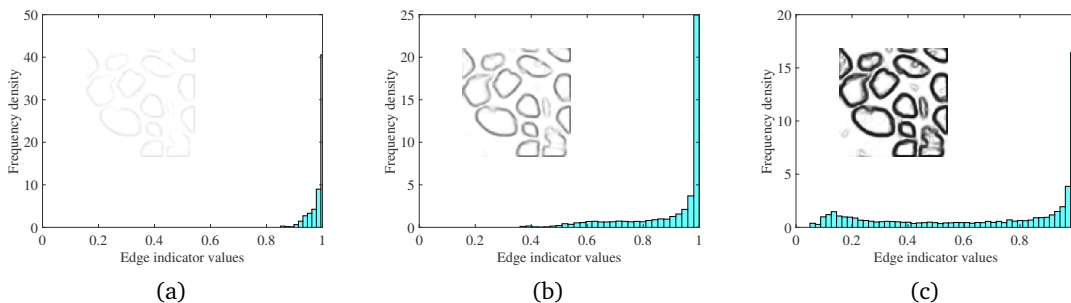
Figure 3.7: A demonstration of the edge indicator with different scaling coefficients: (a) $c=1$, (b) $c=10$, and (c) $c=100$. The histograms indicate the distribution of the edge indicator values, and the inset represents the corresponding edge indicator image.

3.4.2 Solution of the level set function

Solutions of the level set function can be obtained by minimizing the energy functional $\mathcal{F}(\phi)$ in Equation 3.2 with respect to ϕ, which leads to the associated Euler-Lagrange

equation for ϕ (Aubert and Kornprobst, 2006). Parameterizing the descent direction by an artificial time, the solution of the level set function ϕ can be obtained using (Li et al., 2005a, 2010)

$$\frac{\partial \phi}{\partial t} = -\frac{\delta \mathcal{F}}{\delta \phi} = -\left(\mu \frac{\delta \mathcal{R}}{\delta \phi} + \lambda \frac{\delta \mathcal{L}}{\delta \phi} + \nu \frac{\delta \mathcal{A}}{\delta \phi} \right) \tag{3.7}$$

where $\delta[\cdot]/\delta \phi$ denotes the functional derivative of $[\cdot]$ with respect to ϕ. The functional derivative of each term in $\mathcal{F}$ with respect to ϕ is evaluated as

$$\frac{\delta \mathcal{R}}{\delta \phi} = \nabla \cdot \nabla \phi - \nabla \cdot \left(\frac{\nabla \phi}{\|\nabla \phi\|} \right) \tag{3.8}$$

$$\frac{\delta \mathcal{L}}{\delta \phi} = \delta(\phi) \left[\nabla g(I) \cdot \frac{\nabla \phi}{\|\nabla \phi\|} + g(I) \cdot \nabla \left(\frac{\nabla \phi}{\|\nabla \phi\|} \right) \right] \tag{3.9}$$

$$\frac{\delta \mathcal{A}}{\delta \phi} = g(I) \delta(\phi) \tag{3.10}$$

To solve the minimization problem defined by Equation 3.7, a forward discretization scheme in time is implemented such that

$$\phi_{t+1} = \phi_t - \Delta t \left. \left(\mu \frac{\delta \mathcal{R}}{\delta \phi} + \lambda \frac{\delta \mathcal{L}}{\delta \phi} + \nu \frac{\delta \mathcal{A}}{\delta \phi} \right) \right|_t \tag{3.11}$$

where ϕ_{t+1} and ϕ_t are the level set function ϕ evaluated at the timestep $t+1$ and t, respectively; Δt is the timestep. As illustrated in Figure 3.8, the evolution of the level set function ϕ starts with a given initial value ϕ_0 and stops when the energy functional arrives at a stationary state, which corresponds to the surface Γ represented by ϕ matching the particle shape boundary.

Solving the level set function also requires the evaluation of spatial derivatives in Equation 3.8, Equation 3.9 and Equation 3.10, in particular, the evaluation of $\nabla \phi = [\nabla^x \phi, \nabla^y \phi, \nabla^z \phi]$. In this work, a finite difference scheme is implemented to discretize the
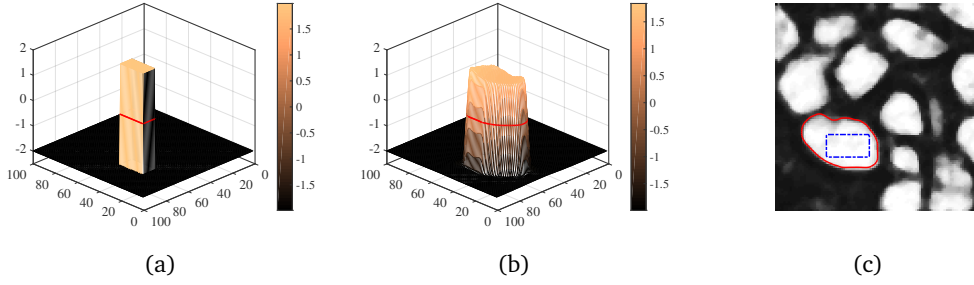
Figure 3.8: An illustration of the level set function evolution: (a) the initial level set values, (b) the final level set values, and (c) the particle shape captured by the zero level set. In (c), the blue dashed line indicates the initial shape, and the red solid line indicates the final captured particle shape.

spatial derivatives, which yields

$$
\nabla^x \phi(i,j,k) = \begin{cases} \phi(2,j,k) - \phi(1,j,k), & \text{if} \quad i = 1 \\ \left[\phi(i+1,j,k) - \phi(i-1,j,k)\right]/2, & \text{if} \quad i = 2,3,...,N_i - 1 \\ \phi(N_i,j,k) - \phi(N_i - 1,j,k), & \text{if} \quad i = N_i \end{cases} \tag{3.12}
$$

$$
\nabla^y \phi(i,j,k) = \begin{cases} \phi(i,2,k) - \phi(i,1,k), & \text{if} \quad j = 1 \\ \left[\phi(i,j+1,k) - \phi(i,j-1,k)\right]/2, & \text{if} \quad j = 2,3,...,N_j - 1 \\ \phi(i,N_j,k) - \phi(i,N_j - 1,k), & \text{if} \quad j = N_j \end{cases} \tag{3.13}
$$

$$
\nabla^z \phi(i,j,k) = \begin{cases} \phi(i,j,2) - \phi(i,j,1), & \text{if} \quad k = 1 \\ \left[\phi(i,j,k+1) - \phi(i,j,k-1)\right]/2, & \text{if} \quad k = 2,3,...,N_k - 1 \\ \phi(i,j,N_k) - \phi(i,j,N_k - 1), & \text{if} \quad k = N_k \end{cases} \tag{3.14}
$$

where i, j, and k indicate the pixel index for each dimension in the image matrix; N_i, N_j and N_k are the dimension sizes, i.e., the total number of pixels in that dimension.

The Dirac delta function $\delta(\phi)$ in Equation 3.9 and Equation 3.10 is approximated by

the following regularized function $\delta_\epsilon(\phi)$ as

$$\delta_\epsilon(\phi) = \begin{cases} \frac{1}{2\epsilon}\left[1 + \cos(\frac{\pi\phi}{\epsilon})\right], & \text{if} \quad |\phi| \leq \epsilon \\ 0, & \text{if} \quad |\phi| > \epsilon \end{cases} \tag{3.15}$$

where ϵ is the regularization coefficient; $|\cdot|$ indicates the absolution value. The regularized $\delta_\epsilon(\phi)$ will converge to $\delta(\phi)$ as ϵ approaches 0.

By minimizing the energy functional, the zeroth isosurface of the level set function eventually approximates the surface of a particle. The marching cubes method can be used to reconstruct the zeroth isosurface from the level set matrix, which returns a triangle mesh representing the particle surface.

3.5   Particle morphology descriptors

Once particles are reconstructed using the level set method, various quantitative descriptors can be calculated to characterize the particle morphology. The three commonly used descriptors are the aspect ratio, sphericity, and roundness. The definition and calculation of these descriptors are presented in this section while results of morphology analysis on the granular soil of interest will be presented in Section 3.6.

3.5.1   Aspect ratio

The aspect ratio of a particle is the ratio of its sizes in different dimensions. It characterizes the elongation extent of a particle. A 3D particle possesses two independent aspect ratios. Standard practice assigns L to the longest dimension, with I being the longest dimension perpendicular to L and S being perpendicular to both L and I. The aspect ratios are calculated as the ratios between L, I and S. However, as pointed out by Blott and Pye (2008), such definitions cannot give an appropriate description of certain shapes (e.g., cubes). An alternative is to use the Feret diameters to characterize the size of a particle along specific dimensions (Ersoy and Waller, 1995; Hentschel and Page, 2003). There are infinite

39

sets of Feret diameters for a given geometric shape. In this work, the three Feret diameters corresponding to the three principal axes are adopted. With the three Feret diameters denoted as D_1, D_2, and D_3, the aspect ratios are calculated as

$$a_{21} = \frac{D_2}{D_1} \tag{3.16}$$

$$a_{31} = \frac{D_3}{D_1} \tag{3.17}$$

where a_{21} is the aspect ratio of the medium Feret diameter (D_2) to the major Feret diameter (D_1); a_{31} is the aspect ratio of the minor Feret diameter (D_3) to the major Feret diameter (D_1). To evaluate the Feret diameters, the moment of inertia tensor is firstly calculated. A rotation matrix is obtained by converting the moment of inertia tensor to a diagonal matrix. The rotation matrix defines the directions of the principal axes of the particle. Then, the particle is rotated by multiplying the rotation matrix, so that the principal axes of the particle are aligned with the Cartesian coordinate axes. Finally, the range of the coordinates of all the vertexes on the particle surface would be the Feret diameters in each direction, respectively.

3.5.2 Sphericity

The sphericity describes the degree to which a 3D particle shape resembles a mathematically perfect sphere. This work adopts the 3D sphericity definition proposed by Wadell (1933)

$$S = \frac{(36\pi V_p^2)^{1/3}}{A_p} \tag{3.18}$$

where S is the sphericity; V_p and A_p are the volume and surface area of the given particle, respectively.

3.5.3 Roundness

The definition or calculation of roundness is subjected to the most controversy. Most authors have accepted that roundness should refer to the relative sharpness of corners

and edges of a particle rather than to the degree to which the overall outline of a particle approaches circularity (or sphericity in three dimensions). Wadell (1933) first defined the 2D roundness as the average ratio of the curvature radius of all corners to the radius of the largest inscribed circle of a particle. Following the same logic, Zhou et al. (2018) defined the 3D roundness, which is adopted in this work.

$$R = \frac{\Sigma g(k)|k_{\max}|^{-1}}{N\,R_{\text{ins}}} \tag{3.19}$$

where R denotes the roundness; N is the total number of acceptable corners; R_{ins} is the radius of the maximum inscribed sphere of the particle; $k_{\max}$ is the maximum curvature at a corner; and $g(k)$ is a function indicates whether a corner is acceptable or not, defined as

$$g(k) = \begin{cases} 1 & \text{if} \quad |k_{\max}|^{-1} < R_{\text{ins}} \\ 0 & \text{if} \quad |k_{\max}|^{-1} \geq R_{\text{ins}} \end{cases} \tag{3.20}$$

In this work, the radius of the maximum inscribed sphere R_{ins} is approximated by the minimum radial distance of all vertexes on the particle surface to the particle centroid. The practical approach proposed by Colombo et al. (2006) is adopted to evaluate the local principal curvatures at the corners of a particle. The interested reader is referred to (Colombo et al., 2006; Zhou et al., 2018) for more details about the calculation.

3.6 Results and discussions

In this section, the proposed framework is applied to characterize and reconstruct 3D irregularly-shaped particles from X-ray CT images of a particular granular material, the Mojave Mars Simulant (MMS). MMS is a Martian regolith simulant developed using a basalt mined in the western Mojave Desert and is among the suite of test rocks and soils that were used in the development of the 2007-2008 Phoenix Scout and the 2009 Mars Science Laboratory missions (Peters et al., 2008). The type of MMS used in this study has particle

sizes mainly ranging from 1 mm to 2 mm. The MMS sample is placed in a cylindrical container of 30 mm in diameter and 114 mm in length. An MILabs U-CT system with a resolution of 60 microns is used to obtain the raw CT image data, which yields a total of 500×500×1900 3D pixels data. To visualize the raw CT image data, the pixels are grouped into 1,900 slices, each being an image of 500×500 pixels. Selected images from the middle are used to demonstrate the proposed framework.

3.6.1 Results by the proposed framework

To begin with, the *classifier* in the machine learning method is determined through a training process. In this process, TWS takes a raw X-ray CT image and two training images with labeled pixels as inputs, shown in Figure 3.9. It should be pointed out that the performance of TWS depends on the quality of the training images. One can repeatedly amend the training images until satisfied with the classification results. The settings for TWS used in this study are summarized in Table 3.2.

<div align="center">(a)   (b)   (c)</div>
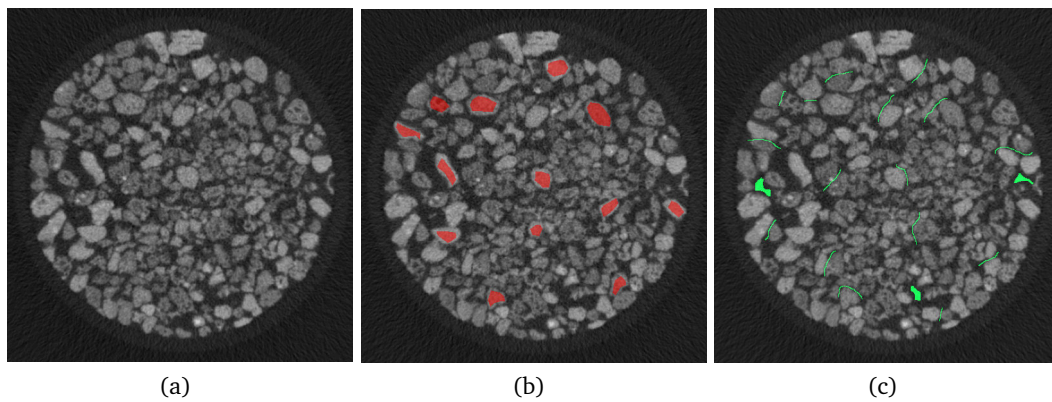
Figure 3.9: Raw and training X-ray CT images: (a) the raw image, (b) the first training image with labeled solid phase (solid pixels are highlighted in red), and (c) the second training image with labeled void phase (void pixels are highlighted in green).

The next process is to apply the trained *classifier* to the remaining raw X-ray CT images. For batch processing, this process is implemented in MATLAB through the Fiji-MATLAB interface *MIJ*, as described in Section 3.3. Figure 3.10 shows an example of the

Table 3.2: Settings for TWS used in the present study.

Entry/Feature	Parameter	Value
Gaussian blur	Standard deviation	1, 2, 4, 8, 16
Sobel filter	Standard deviation	1, 2, 4, 8, 16
Hessian	Standard deviation	1, 2, 4, 8, 16
Difference of Gaussian	Standard deviation	1, 2, 4, 8, 16
Membrane parameters	Thickness	1
	Patch size	19
Random forest	No. of decision trees	200
	No. of random features per tree	2

raw and TWS-processed images. As shown in Figure 3.10b, the TWS-processed images are valued by the probability indicating the likelihood of a pixel belonging to a designated phase (i.e., the solid phase in this study). The probability map will then be used as inputs for level set-based shape reconstruction. The performance of level set method relies heavily on well-defined edge indicators. In practice, it is found that, by applying a prior TWS process, the resultant probability map can provide better edge indicators than the raw X-ray CT image. The corresponding edge indicator map of the example CT image is shown in Figure 3.10c.
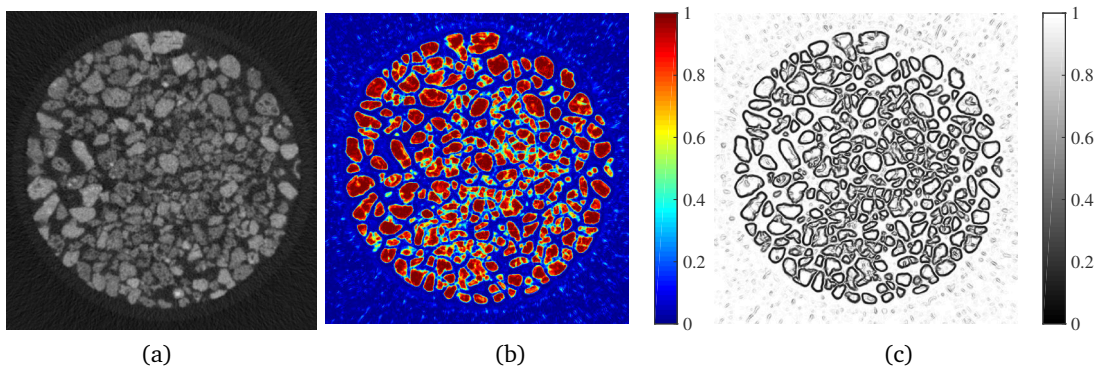
Figure 3.10: Example of (a) the raw X-ray CT image, (b) the probability map, and (b) the corresponding edge indicator calculated based on the processed image. The scaling coefficient for the edge indicator is $c = 100$.

Table 3.3 summarizes the level-set parameters used in this study. The energy coefficients μ, λ and ν, and the regularization coefficient ϵ are selected following the previous

application and recommendation by Li et al. (2010). The scaling coefficient c in the edge indicator equation Equation 3.6 is chosen such that the edge indicator values are scaled between 0 and 1. To obtain the initial level set for a particle to be reconstructed, one option is to adopt the "erosion and labeling" morphological image processing method, where pixels with the same label after the erosion process are considered to belong to the same particle and could be used as the initial level set. However, it is found that this option cannot provide good results for images with complex features as those of MMS considered in this work. Thus, the other option is to label a cuboid inside a particle manually. The cuboid is taken as the initial level set and gradually expands towards the particle boundary as level set evolves. An illustration of the surface evolution of one particle by the edge-based level set method is shown in Figure 3.11. The final 3D surface indicates the surface of the reconstructed particle.

Table 3.3: Level-set parameters used in the present study.

Δt	μ	λ	ν	ϵ	c
1	0.2	5.0	1.5	0.5	100
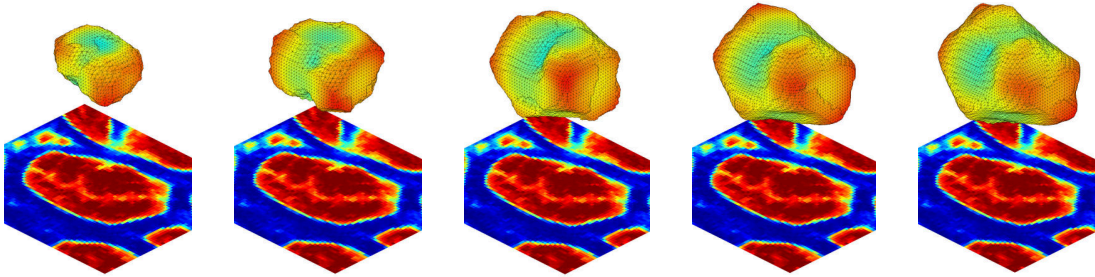
Figure 3.11: An illustration of the surface evolution of one particle by the edge-based level set method at the 100th, 200th, 300th, 400th, and 500th iterations. The 2D image, colored by the probability values evaluated by the TWS method, shows the part of the CT image containing the target particle to be constructed. The final 3D surface indicates the surface of the reconstructed particle.

The level-set process is applied to all particles in the processed CT images. In this work, the particle shape is represented and visualized using the surface triangle mesh, which is built upon the level-set matrices using the marching cubes method (Lorensen and Cline, 1987). There are other methods to represent a complex geometry, such as the orthogonal

decomposition, Fourier descriptor (Luerkens et al., 1982), and the non-uniform rational basis spline (Andrade et al., 2012c). Figure 3.12 presents one layer of the reconstructed 3D particles and the zoom-in view of several particles. It can be seen that particles of different sizes are successfully reconstructed. Some of the particles are relatively round, whereas others exhibit pretty sharp edges. The roughness of the particle surface is also well preserved, and some concave pits are captured on the particle surface. Quantitative shape and size analysis on the reconstructed particles will be presented in the following sections.

(a)   (b)
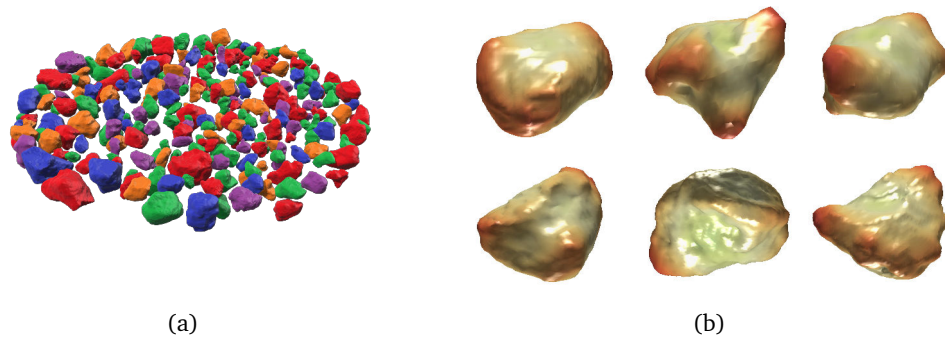
Figure 3.12: Showcases of (a) one layer of the reconstructed 3D particles, and (b) zoom-in views of several particles. Particles in (a) are rendered with different colors for better visualization.

3.6.2 Accuracy analysis and validation

To evaluate the performance of the proposed framework, accuracy analysis is conducted in this section. The same analysis is also conducted for a watershed-based method as a comparison. As an additional validation, the size distribution of the reconstructed particles is compared to that obtained from a laboratory sieve analysis.

3.6.2.1 Definitions of accuracy

Before defining the accuracy, a reference solution of image segmentation is required. In this work, a manually labeled image is taken as the reference solution (i.e., the ground truth). To manually label the image, the particle boundary is carefully traced using the

magnetic lasso tool in *Adobe Photoshop*. After that, the region inside the boundary is colored using the paint bucket tool. This process is repeated until all particles are identified and painted in different colors. It should be pointed out that the manually labeled particle shape might still deviate slightly from its *real* shape due to human error. Such deviation, however, is only a couple of pixels and would be acceptable considering that the particle sizes are of 25 pixels on average in each dimension.

This study considers two types of accuracy: pixel-based classification accuracy and particle-based segmentation accuracy. The pixel-based classification accuracy indicates the possibility that a pixel is classified into the correct phase (i.e., solid phase and void phase in this work). To quantify it, the pixel accuracy index and random accuracy index proposed by (Arganda-Carreras et al., 2015) are adopted. In particular, the joint probability p_{ij} is first defined as the probability that a randomly chosen pixel belongs to phase i in S and phase j in T, where S denotes the predicted classification and T denotes the reference solution. Then, the pixel accuracy index V_{pixel} and the random accuracy index V_{rand} are calculated as

$$V_{\text{pixel}} = p_{ii} \tag{3.21}$$

$$V_{\text{rand}} = \frac{\Sigma_{ij} p_{ij}^2}{\alpha \Sigma_k s_k^2 + (1-\alpha)\Sigma_k t_k^2} \tag{3.22}$$

where $s_i = \Sigma_j p_{ij}$ and $t_j = \Sigma_i p_{ij}$, which is the probability of a randomly selected pixel belonging to phase i or j, respectively; α is a parameter indicating the weights of split and merge errors. By definition, V_{pixel} indicates how many pixels are correctly classified. V_{rand} quantifies the probability that two randomly chosen pixels belong to the same phase in both predicted classification S and reference T. V_{rand} should be close to one if S and T are similar. It should be noted that other indices have also been proposed and used for accuracy or error analysis. For instance, Semnani and Borja (2017) used three measures to compare a simulated image with the true image: variograms, pixel-wise error histograms and visual comparisons, where continuous variables (i.e., gray values) are used as opposed to categorical variables (i.e., individual phases) adopted in the current study.

To evaluate the particle-based segmentation accuracy, the number of correctly identified particles are counted. As a particle consists of hundreds of pixels, in this study, a particle is considered to be correctly identified if more than 90% of its pixels are correctly predicted and grouped to the same particle. The 10% tolerance is set to account for the slight errors in manually labeling a particle and the acceptable tolerance in the reconstructed particle shapes. It is worth noting that, for the accuracy analysis, we are focusing on just one slice of the CT images as a demonstration. The particle shape reconstructed using the proposed framework is indeed three-dimensional, but only a cross-section of the shape is extracted and compared to the reference solution.

3.6.2.2 Compare with the watershed-based method

Watershed (Vincent and Soille, 1991) is a common tool for image segmentation. Segmentation by the watershed method requires meaningful local extrema to initiate the watershed and an appropriate threshold to stop the watershed. Otherwise, the watershed process can result in serious over-segmentation. Some variants of the original watershed method have been proposed, aiming to mitigate the over-segmentation issue (Matsushima et al., 2009; Zheng and Hryciw, 2016). The particular implementation of watershed method used in this work for the comparison is the interactive H-watershed (Lombardot, 2017), which is available as a plugin in Fiji. The interactive H-watershed consists of a threshold process to classify phases and a watershed process to segment objects. In the watershed process, it employs the so-called H-extrema as the local extrema to initiate the watershed, where the H-extrema are known to be robust to noise. The interactive H-watershed also provides an interactive way to explore local extrema and threshold, updating the resulting watershed on the fly.

The pixel-based classification accuracy of the interactive H-watershed is controlled by the threshold parameter. Histograms of pixel values for the raw CT image and the corresponding TWS-processed image are plotted in Figure 3.13. Two peaks are observed in the histogram of the raw CT image (Figure 3.13a), corresponding to the void phase

and the solid phase, respectively. The distribution of pixel intensity can be approximated by two normal distributions, and it can be seen in Figure 3.13a that the two distributions representing the void phase and the solid phase would have large areas of overlap. In this case, it becomes critical to determine a single threshold to classify the void phase and solid phase. A small change in the threshold value would result in significant changes in the resulting fraction of the void phase and the solid phase.

In the proposed TWS-based segmentation, the material phases are determined using both the pixel intensity values and various image features (e.g., those listed in Table 3.1). After the TWS process, each pixel is given a probability value indicating its likelihood to be a designated phase (e.g., the solid phase). The histogram of probability values of the corresponding TWS-processed image is shown in Figure 3.13b. It is observed that the two peaks representing the void and solid phases are more separated apart. Such a profile indicates that most of the pixels can be classified with great confidence, leaving only a small portion of the pixels (i.e., those with probability values around 0.5) with lower confidence.

(a) Raw CT image   (b) TWS processed image
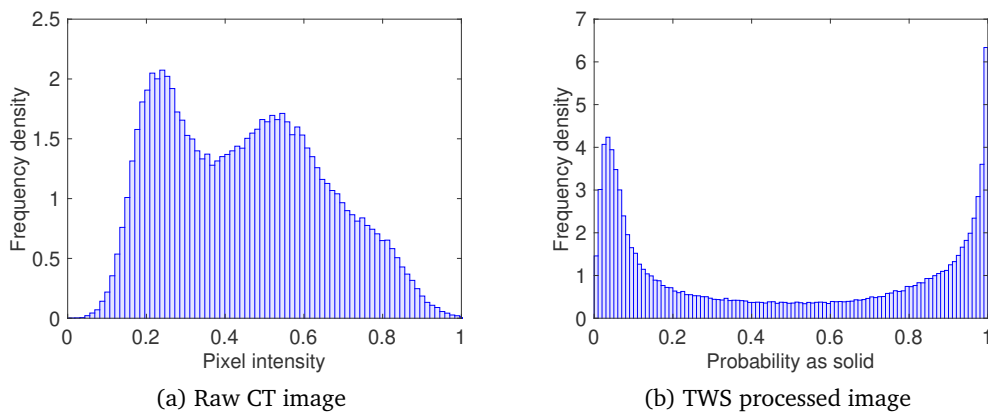
Figure 3.13: Histograms of (a) a raw CT image, and (b) the corresponding TWS processed image.

To illustrate the influence of the assumed threshold values, different threshold values are applied and the accuracy of the interactive H-watershed is summarized in Table 3.4. In TWS, pixels with a probability value greater than 0.5 (i.e., voted as the solid phase in the random forest process) are classified as the solid phase. With a reasonable choice of

a threshold value, the interactive H-watershed method can achieve a good performance that is comparable with the TWS. However, as it will be shown later, a reasonable choice of threshold values does not assure good particle segmentation. A significant limitation with the thresholding is that it cannot resolve the noises existed in the void phase or solid phase. TWS, on the other hand, has shown to be much more effective when applied to low-resolution images with noise (Madra et al., 2014).

Table 3.4: Pixel-based classification accuracy: interactive H-watershed vs. TWS-LS.

Method	V_{pixel}	V_{rand}
TWS-LS	0.86	0.76
Interactive H-watershed		
$\quad$ Threshold = 0.3	0.85	0.75
$\quad$ Threshold = 0.4	0.89	0.81
$\quad$ Threshold = 0.5	0.84	0.74

For the second type of accuracy, i.e., the particle-based segmentation accuracy, the interactive H-watershed mainly relies on the parameter called the H-extrema seed. Large seed values can help suppress local extreme used to initialize the watershed, thus minimizing the over-segmentation issue. However, an optimal choice of the seed parameter is problem dependent. The performances of the interactive H-watershed with different H-extrema seeds are investigated in this study. Table 3.5 summarizes the number of correctly segmented particles using the interactive H-watershed and the proposed TWS-LS method. For the interactive H-watershed, the number of correct particles significantly depends on the choice of the seed parameter. With regard to the particle-based segmentation accuracy, the TWS-LS shows superior performance. It is worth noting that, even if the TWS-LS cannot correctly reconstruct all the particles (i.e., reaching 100% accuracy), there will be statistically enough particles for the purpose of morphology characterization and particle size distribution calculations.

To visualize the particle-based segmentation accuracy, the correctly and incorrectly segmented particles are shown in Figure 3.14. In these figures, the incorrect particles are plotted as hollow shapes. For TWS-LS, most of the incorrect particles are the particles

Table 3.5: Particle-based segmentation accuracy: interactive H-watershed vs. TWS-LS.

Method	Correct particles	Percent
TWS-LS	234	77.7%
Interactive H-watershed		
Seed = 20	188	62.5 %
Seed = 25	163	54.2 %
Seed = 30	144	47.8 %

of smaller sizes. As aforementioned, this is partially due to the relatively insufficient CT resolution to resolve fine particles. For the interactive H-watershed, the incorrect particles have a wide size range, most of which are results from the issue of over-segmentation.

(a) Ground truth   (b) TWS-LS   (c) Interactive H-watershed
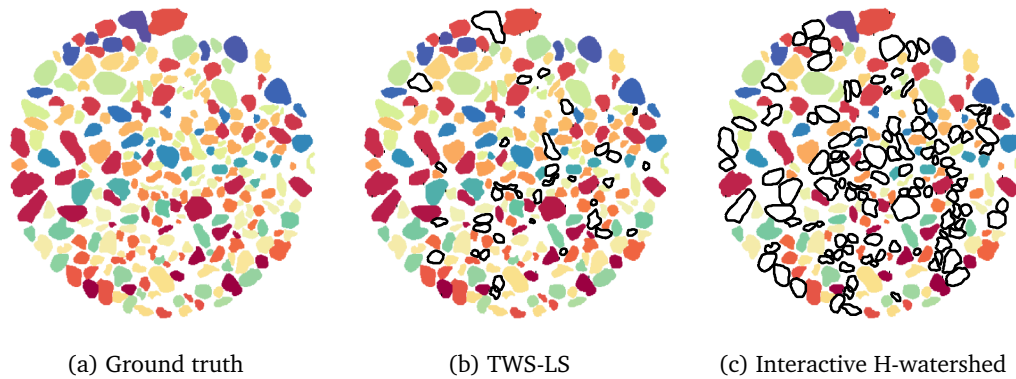
Figure 3.14: Visual comparison of segmentation accuracy of the interactive H-watershed and the proposed TWS-LS method. Incorrectly identified particles are plotted as hollow shapes.

3.6.2.3 Validation with laboratory sieve analysis

In the laboratory sieve analysis, the following sieves in the Unified Soil Classification System are used: No. 4, 10, 20, 40, 60, 100, and 200. Based on the extracted particle shapes from CT image analysis, the particle sizes can be estimated as the diameter of their equivalent sphere (e.g. a sphere of the same volume). The particle-size distribution (PSD) curves obtained from the lab and the proposed TWS-LS framework are shown in Figure 3.15. A reasonably good agreement is shown between the two curves. The PSD obtained from the proposed framework is slightly shifted to the left. Also, there is some discrepancy observed in

particle sizes smaller than 0.5 mm. Those smaller particles are missing in the PSD obtained from the X-ray CT images as the resolution of the X-ray CT scanner cannot capture those very fine particles.
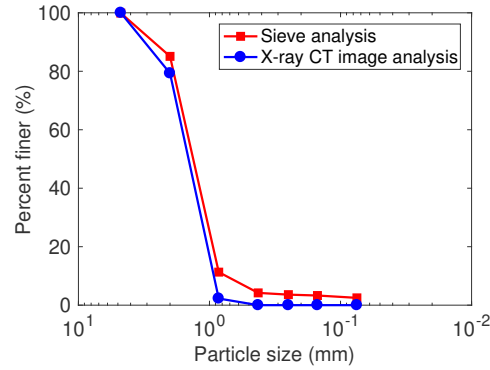
Figure 3.15: Particle size distribution.

3.6.3   Particle morphology analysis

Having the particles fully reconstructed in 3D, quantitative morphology analyses are conducted using the morphology descriptor defined in Section 3.5. Figure 3.16 showcases the calculated morphology of several example 3D particles. Among these examples, the top-left particle is more elongated in one direction, corresponding to smaller values of aspect ratio (a_{21} and a_{31}). By comparison, the bottom-right particle has similar size in each direction, which results in larger values aspect ratio. It is also observed that the particles with more *angular corners* have smaller values of sphericity (S) and roundness (R), as is the case for the three particles in the bottom row.

To provide a statistical description of the particle morphology, the histogram of the aspect ratio, sphericity, and roundness from the reconstructed particles are plotted in Figure 3.17. It is found that these descriptors can be roughly approximated by normal distributions. In this regard, their mean values and standard deviations are summarized in Table 3.6. As a comparison, the mean sphericity and roundness of the Leighton Buzzard sand are reported to be about 0.92 and 0.65 (Zhou et al., 2018). Leighton Buzzard sand is an

51

$a_{21} = 0.76$
$a_{31} = 0.59$
$S = 0.90$
$R = 0.63$

$a_{21} = 0.88$
$a_{31} = 0.78$
$S = 0.87$
$R = 0.65$

$a_{21} = 0.79$
$a_{31} = 0.69$
$S = 0.88$
$R = 0.61$

$a_{21} = 0.88$
$a_{31} = 0.77$
$S = 0.87$
$R = 0.59$

$a_{21} = 0.73$
$a_{31} = 0.58$
$S = 0.86$
$R = 0.54$

$a_{21} = 0.97$
$a_{31} = 0.82$
$S = 0.87$
$R = 0.54$
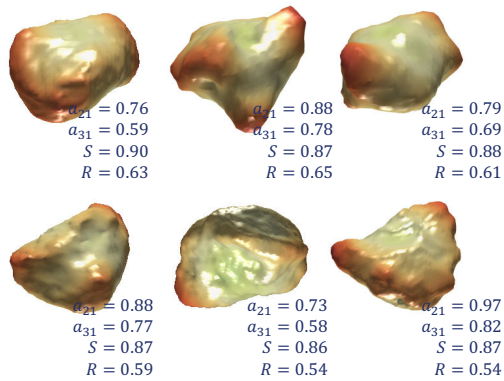
Figure 3.16: Morphology of several example 3D particles.

English sand commonly used for academic research. It can be seen that the MMS particles, made from crashes of Saddleback Basalt, is more irregular than the Leighton Buzzard sand.

Table 3.6: Statistics of the morphology descriptors of MMS soil particles.

Descriptors	Mean	Standard
Aspect ratio a_{21}	0.78	0.11
Aspect ratio a_{31}	0.61	0.11
Sphericity S	0.84	0.04
Roundness R	0.64	0.05

To classify the roundness grades of the MMS sample, the cumulative distribution of the roundness values by volume is displayed in Figure 3.18. The Powers classification (Powers, 1953) of roundness is also shown. Results indicate that there are about 4% well-rounded particles, 95% rounded particles, and less than 1% subrounded particles, following the roundness grade table of Powers (1953). The detailed morphology analysis presented in this section is not possible without the reconstructed particles using the proposed framework and the analysis can provide important insights into the microscopic features of the granular material.
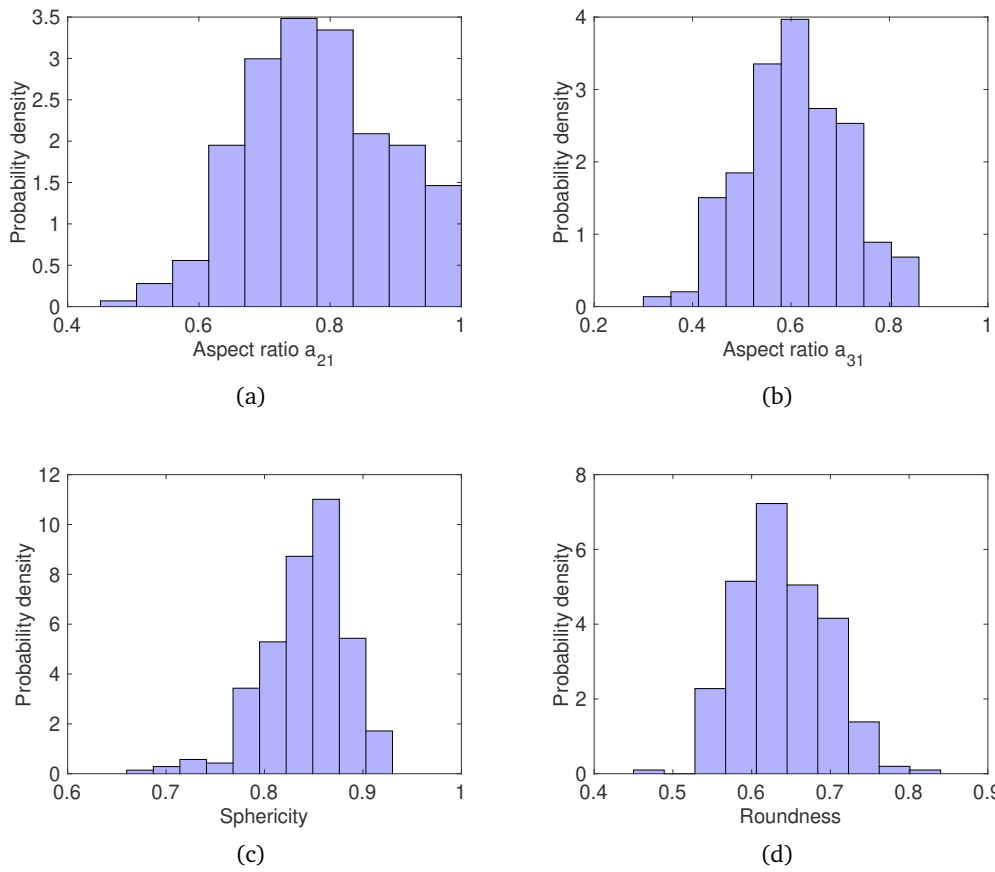
Figure 3.17: Histogram and fitted distribution of the morphology descriptors of MMS soil particles: (a) aspect ratio a_{21}, (b) aspect ratio a_{31}, (c) sphericity and (d) roundness.
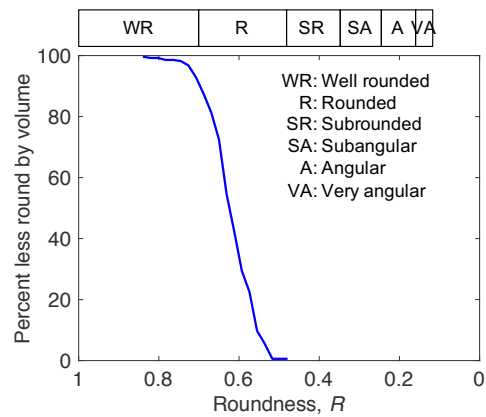
Figure 3.18: Particle roundness distribution of the MMS sample with the Powers (1953) classification.

3.7　Summary

In this work, a novel machine learning and level set-based framework is proposed to segment X-ray CT images of granular geomaterials and to reconstruct realistic 3D particle shapes. X-ray CT images of the Mojave Martian simulant (MMS) show that the intensity of various constituents exhibit significant variance and there is no clear demarcation between the solid and the void phases, making it particularly challenging for conventional binarization-watershed-based methods.

To address this challenge, a feature-based machine learning technique termed the Trainable Weka Segmentation (TWS) is implemented and utilized to segment X-ray CT images. This is a fundamentally different approach in that it predicts segmentation results based on a trained classifier model that implicitly includes image features and regression functions. Probability maps indicating the likelihood of pixels belonging to a particular phase are obtained from the segmentation process, in which the original intensity contrast feature is to the most extent preserved. Compared to the intensity values of a raw CT image, it is found that the probability values exhibit much less variance and have a more distinct demarcation between different material phases. The probability map provides excellent edge indicators that can be used as the basis for the subsequent edge-based level set method.

Using the segmented X-ray CT images (i.e., probability maps), a 3D edge-based level set method is implemented to approach an accurate shape representation of real particles. Realistic 3D particles of the MMS are successfully reconstructed from raw CT images. Quantitative accuracy analyses are performed for the proposed framework and a conventional watershed method. The analyses show that the proposed framework has superior performance in both pixel-based classification accuracy and particle-based segmentation accuracy. The particle size distribution using the reconstructed particles are also validated and compared well with results from a lab sieve analysis. In addition, the morphological features, e.g., sphericity, roundness, and roughness, of real particle shapes are well captured.

Quantitative particle morphology analyses are performed to provide more insights into the morphological features of the granular material.

The machine learning technique has shown great potentials in segmenting CT images of geomaterials with complex constituents. Future work will expand the capability and application of machine learning-based particle identification. An immediate step would be to promote the current 2D TWS into the 3D regime, where image features from the third dimension are included in the segmentation process synchronously. Another interesting and important issue would be the effect of the quantity and quality of the training sets on the accuracy of the segmentation results. It is also noticed that there are several competing machine learning-based image segmentation algorithms. It would be interesting to explore alternative methods and compare their performances when applied to granular geomaterials. Finally, the closed surface reconstructed by the edge-based level set method can be readily used for shape analysis and in a subsequent numerical model (e.g., the discrete element model) development.

Chapter 4

Characterization and discrete element simulation of grading- and shape-dependent behavior of JSC-1A Martian regolith simulant

Granular regolith simulants have been extensively used in the preparation of space missions to test rovers and scientific instruments. In this work, the physical and mechanical properties of the JSC-1A Martian regolith simulant (MRS) are characterized using conventional and advanced laboratory techniques. Particle images are obtained using X-ray computed tomography, from which particle shapes are characterized through a series of imaging processing techniques and are further used to generate irregularly-shaped numerical particles. The characterized particle size distribution and irregularly-shaped numerical particles are incorporated into a discrete element model to simulate grading and shape-dependent behavior of the JSC-1A MRS. The developed discrete element model is calibrated

and validated against laboratory direct shear tests. Simulations without the consideration of particle shapes and simulations with a rolling resistance contact model are also performed to investigate the effect of particle shapes on the behavior of the JSC-1A MRS.

4.1 Introduction

Martian regolith simulant (MRS) is an analogue developed using terrestrial soils based on the current understanding of real Martian regolith. It provides a preview of the physical environment an exploration rover may encounter in a space exploration mission. The understanding of regolith properties and the ability to predict regolith behavior would help guide the design of rovers, minimize the risk of sinkage and slippage during rover maneuver, and provide constraints for geomorphological modeling Iagnemma et al. (2005); Sullivan et al. (2011); Ding et al. (2011). Moreover, a thorough understanding of regolith properties are needed to develop new regolith-based materials for functional building blocks for future infrastructure needs on Mars Carranza et al. (2006); Sen et al. (2010); Wan et al. (2016); Moses and Bushnell (2016). There has been continuous research to develop different MRS for various applications. Table 4.1 summarizes a non-exclusive list of currently developed MRS worldwide that are suitable for physical and mechanical experiments.

MRS consists mostly of irregularly-shaped particles of various sizes. To accurately model and predict their behavior, it is important to realize that the information pertaining to such material behavior is fundamentally encoded at the grain scale Tu et al. (2009); Chen et al. (2011); Andrade et al. (2012a). In the context of mechanical responses, two of the most salient factors are the particle size distribution (i.e., grading) and particle shapes. The micromechanics-based discrete element method (DEM) Cundall and Strack (1979) is ideally suited to capture those salient features of granular materials from a fundamental level.

In the context of modeling MRS, Hopkins and co-workers Hopkins et al. (2008, 2012) are among the first researchers to develop DEM-based numerical models to simulate the soil-rover behavior and soil digging in regolith simulant. Non-spherical particle shapes

Table 4.1: Currently developed Marian regolith simulants suitable for physical and mechanical experiments.

Type	Description	Location	Reference
JSC-1A	Glassy volcanic ash and cinders	Hawaii, US	(Allen et al., 1998)
ES-1	Fine dust	Nepheline Stjernoy, UK	(Brunskill et al., 2011; Gouache et al., 2011)
ES-2	Find aeolian sand	Red Hill, UK	(Brunskill et al., 2011; Gouache et al., 2011)
ES-3	Coarse sand	Leighton Buzzard, UK	(Brunskill et al., 2011; Gouache et al., 2011)
MMS	Basalt crushing	California, US	(Peters et al., 2008)
Scott	Banks Peninsula basalts	South Island, New Zealand	(Scott et al., 2017)
JMSS-1	Basalt crushing, magnetite and hematite	Jining and Hebei, China	(Zeng et al., 2015)

are accounted for using polyhedral grains having basic shapes. In Knuth et al. (2012), a three-dimensional DEM is used to simulate regolith behavior in triaxial tests and interactions with a rover wheel. The particle shape is found to be a crucial factor in the simulated regolith behavior, and the use of ellipsoid and poly-ellipsoid particle shapes improved agreement between simulation and experiment. In a more recent work Johnson et al. (2015), a tri-sphere particle clump is developed to account for the particle interlocking effects and is used within a mono-dispersed particle assemblies to simulate MRS. As an alternative approach to account for particle shape effect, a rolling resistance contact model is integrated into the DEM model to simulate wheel-soil interaction over rough terrain Smith and Peng (2013). Although different types of non-spherical or non-disc particle shapes have been used in previous studies, the effects of realistic particle shapes and particle size distribution have yet to be included and will be the focus of this work.

In this work, physical and mechanical properties of JSC-1A MRS are characterized by a series of laboratory tests. Of particular interests are the particle size distribution and realistic particle shapes. X-ray computed tomography is used to obtain particle images, from which particle shape data is obtained and used in constructing irregularly-shaped particles. Grading and shape-dependent DEM model are developed to simulate and predict the behavior of JSC-1A MRS, which is among the first efforts to incorporate the realistic particle size distribution and particle shapes into a numerical model to simulate the behavior of MRS.

4.2   Laboratory tests on JSC-1A Martian regolith simulants

A series of laboratory tests are conducted to characterize the physical and mechanical properties of JSC-1A MRS. The type of JSC-1A MRS used in this work has particle sizes smaller than 5 mm and is distributed by Orbital Technologies Corporation. The JSC-1A MRS is a natural earthen material obtained from volcanic ashes. It approximates, within the limits of current understanding, the reflectance spectrum, mineralogy, chemical composition,

particle size, density, porosity, and magnetic properties of the oxidized soil of Mars Allen et al. (1998). It is well suitable to help understand the mechanical behavior of real Martian regolith. In addition, as the MRS is actually an earthen material, the framework and findings from this work could be applied to other earthen soils.

4.2.1 Characterization of physical and mechanical properties

Table 4.2 lists laboratory tests conducted in this study and the corresponding ASTM standards to characterize the physical and mechanical properties of the JSC-1A MRS.

Table 4.2: Laboratory tests conducted and the corresponding ASTM standards.

Test	ASTM standard
Specific gravity	ASTM D854-14
Sieve analysis	ASTM D422-63
Hydrometer analysis	ASTM D422-63
Atterberg limits analysis	ASTM D4318-10
USCS soil classification	ASTM D2487-11
Direct shear test	ASTM D3080-11

The specific gravity of the JSC-1A MRS is measured to be 1.94 ± 0.02. The maximum particle size of the soil sample is 5 mm, and the mean particle size is 0.41 mm. The particle size distribution will be detailed and further characterized in a subsequent section. The coefficient of uniformity C_u and the coefficient of gradation C_c, based on Equation 4.1 and Equation 4.2, are calculated to be 20.77 and 1.42, respectively.

$$C_u = \frac{D_{60}}{D_{10}} \tag{4.1}$$

$$C_c = \frac{(D_{30})^2}{D_{10} \times D_{60}} \tag{4.2}$$

where D_{10}, D_{30}, and D_{60} are the particle diameters corresponding to 10%, 30%, and 60% finer in the particle size distribution curve, respectively.

Atterberg limit analysis shows that the fine content of the simulant is non-plastic.

60

Based on the above information, the JSC-1A MRS is classified as well-graded sand (SW) following the Unified Soil Classification System (USCS). The bulk unit weight of the simulant is estimated from specimens of the direct shear test, and its value is evaluated to be 934 ± 30 kg/m^3.

4.2.2   Characterization of shear strength

Shear strength parameters of the MRS are characterized through the direct shear test (ASTM D3080-11). The specimen in the direct shear test is a cylindrical shape with a diameter of 63.5 mm (i.e. 2.5 inches) and a height of 25.4 mm (i.e. 1.0 inch). During preparation, the specimen is vibrated and slightly compacted with a pestle to remove the potential cavity and to improve the sample homogeneity. The specimen is firstly consolidated with specified confining pressure. Three levels of nominal confining stress are considered: 95.8, 191.5, and 383.0 kPa (i.e. 2,000, 4,000 and 8,000 psf). After consolidation, the specimen is sheared at a rate of 0.254 mm/min by applying a lateral displacement to the lower part of the shearing cell. For each level of confining stress, three specimens are prepared and tested. The averaged responses are reported and will be used to calibrate and validate numerical models.

The stress and normalized shear (lateral) displacement relations are shown in Figure 4.1a. The normalized shear displacement is the ratio of the lateral displacement of the lower part of the shear cell to its diameter. The actual contact area between the upper and lower shearing cell is used in the calculation. From the figure, it can be seen that there is no notable reduce of the shear stress after the peak value. As shown in Figure 4.1b, at a low or medium normal stress (i.e., 95.8 and 191.5 kPa), the specimen exhibits a dilative behavior. This dilative behavior is suppressed under high normal stress (383 kPa). The volumetric strain starts to decrease after the peak shear stress. This phenomenon may be contributed by the breakage of the large particles that leads to a reduction in the overall volume.

The maximum friction angle is determined by fitting the test data in the maximum shear stress vs. normal stress plot, as shown in Figure 4.2a. For the JSC-1A MRS, the
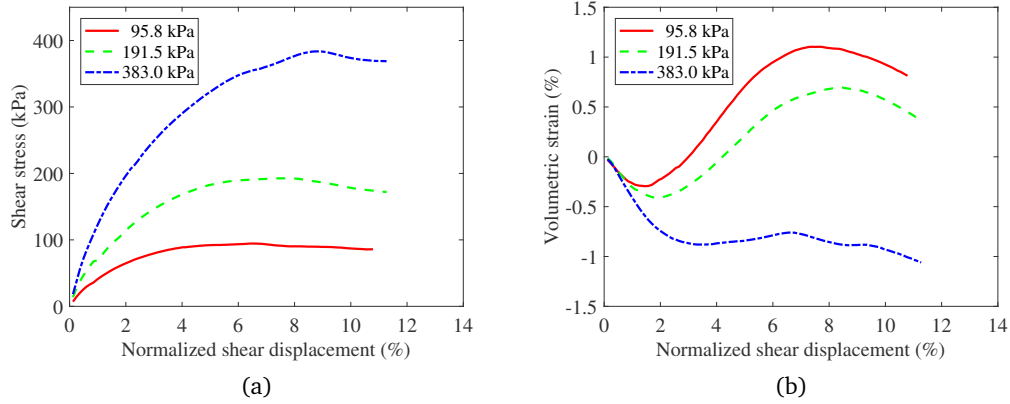
Figure 4.1: Results of laboratory direct shear test on JSC-1A MRS: (a) shear stress vs. normalized shear displacement, (b) volumetric strain vs. normalized shear displacement.

maximum friction angle is found to be $41.4° \pm 2.2°$. There is a very small cohesion strength of 94 psf, which will be neglected in this study. The phenomenon of small cohesion obseved in the bulk soil may be a fact of nonlinear failure envelope effects. For the calculation of dilation angle, the following definition is adopted Simoni and Houlsby (2006)

$$\tan \psi = -\frac{\dot{\epsilon}_{yy}}{\dot{\epsilon}_{xy}} = \frac{dv}{du} \tag{4.3}$$

where $\dot{\epsilon}_{yy}$ and $\dot{\epsilon}_{xy}$ are the time derivative of the yy (vertical) and xy (shearing) components of the strain tensor, respectively; dv and du are incremental vertical and shear displacement, respectively. Figure 4.2b shows the maximum angle of dilation evaluated by Equation 4.3 for all three normal stresses.

4.3 Characterization of particle size distribution

In this section, details on characterization and modeling of particle size distribution are presented. In the sieve analysis, the following sieves are used: No. 4, 10, 20, 40, 60, 100, and 200. Hydrometer analysis is used to further characterize the size distribution for
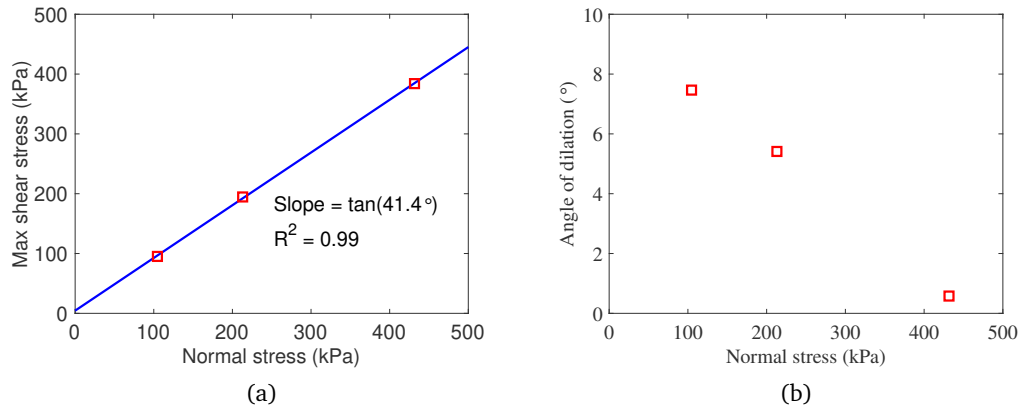
Figure 4.2: Maximum friction and dilation angles evaluated from laboratory direct shear tests: (a) maximum shear vs. normal stress; (b) maximum dilation angle.

the fraction that is finer than the No. 200 sieve size (0.075 mm). The resulting particle size distribution curve is shown in Figure 4.3a.
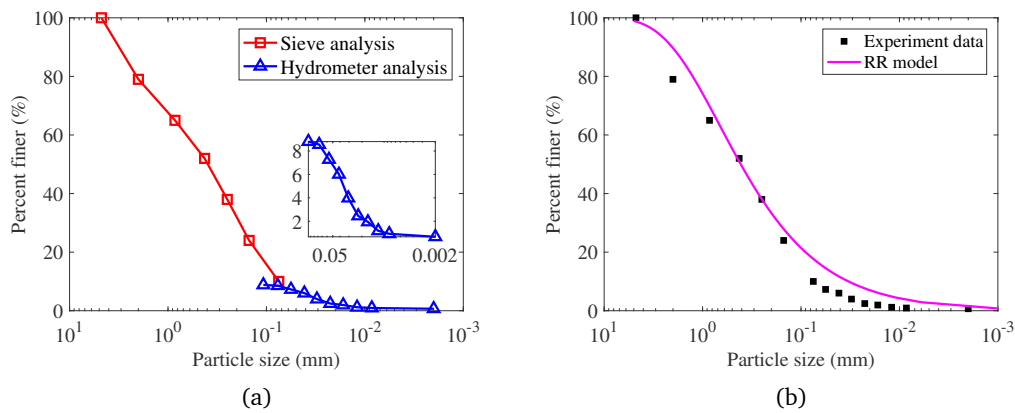
Figure 4.3: Particle size distribution of JSC-1A MRS: (a) data obtained from sieve and hydrometer analysis; (b) fitted by a Rosin-Rammler (RR) distribution model with model parameters $D_{50} = 0.41$ mm, $\beta = 0.75$.

The particle size distribution data obtained from laboratory tests could be fitted through distribution models. In this work, the Rosin-Rammler (RR) distribution model is adopted Rosin and Rammler (1933). A new form of the cumulative distribution function is proposed in this work that modifies a previous version Allaire and Parent (2003) to use the

mean particle size as a model parameter. The modified form of the RR model is given as

$$F(x) = 1 - \exp\left(\log(0.5)(x/D_{50})^\beta\right) \tag{4.4}$$

where D_{50} is the mean particles size; β is an empirical parameter that controls the shape of the function. Note that we rewrite the formulation of cumulative distribution function in Equation 4.4 based on the convention formulation Allaire and Parent (2003), to relate the fist parameter to a more physical-meaningful parameter D_{50}. A smaller β value yields a wider particle size distribution curve while a larger β value would yield a more narrow distribution. The fitted RR model to the experiment data of the JSC-1A MRS is shown in Figure 4.3b and the model parameters $D_{50} = 0.41$ mm and $\beta = 0.75$.

4.4 Characterization of particle shapes

An equivalent important factor affecting the mechanical behavior of the regolith simulant is its particle shapes. In this work, an MILabs U-CT system with an optimal resolution of 100 micron is used to obtain X-ray computed tomography (CT) image data of individual particles within the regolith simulant specimen. Imaging processing algorithms are implemented to extract, quantify and characterize particles shape data, which is then used to develop shape-dependent discrete element models.

4.4.1 X-ray computed tomography imaging and pre-processing

Figure 4.4 shows the regolith simulant, the specimen to be scanned, and a typical raw image obtained from CT scan.

The raw images obtained from CT scan require a series of pre-processing steps before they can be used to extract particle shapes. The pre-processing steps include image enhancement, vessel removal, smooth filtering and inner particle void filling (Soille, 2013).

The image enhancement is to enhance the contrast between the particle pixels and the background pixels. A contrast limited adaptive histogram equalization (CLAHE)
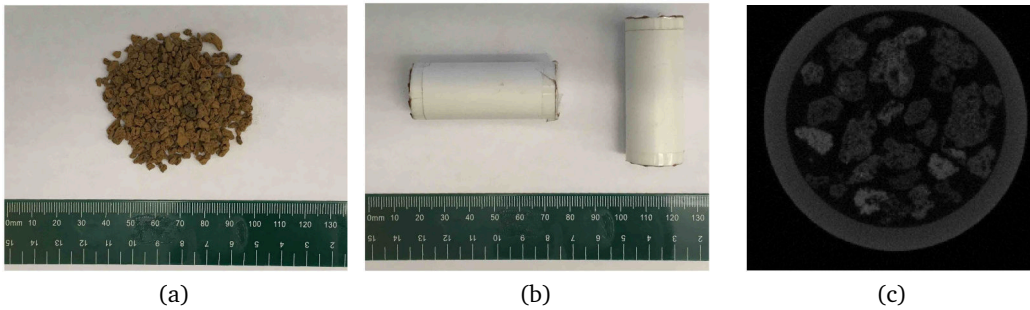
Figure 4.4: X-ray CT imaging experiment: (a) regolith simulant; (b) specimen to be scanned; (c) a tyical raw image.

Zuiderveld (1994) is implemented for this purpose. Vessel removal is to remove the column vessel containing the sample particles. Due to the perturbation of tomography environment and the limitation of CT optical apparatus, the CT image may contain significant noises. Therefore, a smooth filtering technique termed the median filter algorithm (Lim, 1990) is used to reduce the noise pixels. Finally, the inner particle voids, due to either imaging noise or actual voids within the particle, will be "filled" during pre-processing. The filling step is justified based on the fact that interactions between particles in the numerical model will be determined by the outer boundary of each particle only.

The image pre-processing steps can be used in combination to obtain optimal images for shape extraction. Figure 4.5 shows the pre-processing of a typical raw image. It should be pointed out that, no matter how advanced algorithms are used, there processed images may still pose unreasonable pixel values. Manual adjustment may be used to remove unnecessary pixels and to improve the image quality.

4.4.2 Particle shape identification

Given a processed CT image, particle shapes will be identified and extracted. Three techniques are used for this purpose: component differentiation, watershed segmentation, and shape identification.

Component differentiation Component differentiation refers to classifying individual com-

65

(a) Raw image (b) Image enhancement (c) Vessel removal

(d) Smooth filtering (e) Filling voids (f) Smooth filtering
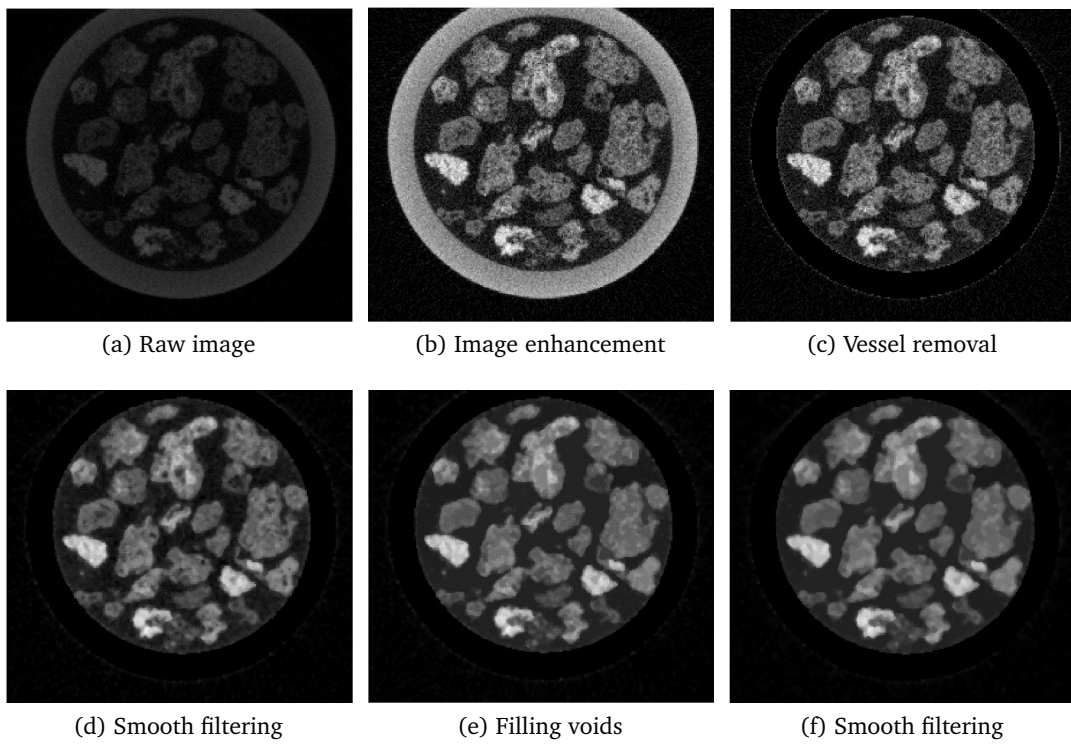
Figure 4.5: An illustration of the CT image pre-processing on a typical raw CT image.

ponent of a specimen. It is based on the fact that different types of component have different X-ray attenuation coefficients, which can be further converted to grayscale images. Clustering algorithms, such as the K-mean clustering algorithm Faber (1994); Chen et al. (1998), can be applied to distinguish each component type in a sample. A particular case of the clustering analysis is binarization, where only two components need to be identified. An example is to identify the solid and void phases within a specimen, as is the case in this work.

Watershed segmentation The watershed segmentation algorithm Meyer (1994) is commonly used to segregate individual particles. Watershed segmentation algorithm imitates a water flooding process, where water rises from a *local* minimum altitude and flows towards the *nearest* not-flooded minimum altitude. The floods rise from different *local* minimum altitude or basin would encounter and form a boundary between each basin, thus segregate each basin. In application, topographic distance field is computed from the binary image and used as the altitude in watershed segmentation.

Shape identification Shape identification is used to mark or label the segregated particles. After watershed segmentation, the particles will be segregated from each other by the watershed boundaries. Then, every particle pixels inside the same boundary can be marked and identified as a single particle. The general procedure outlined in Haralock and Shapiro (1991) is commonly used.

It should be noted that, during the watershed segmentation, the image is required to be "eroded" by a topographic structure element. The size of the topographic structure element would impact the segregated particle shapes. If the element size is too small, the algorithm may not be able to identify two particles that are in touch. On the other hand, if the element size is too large, the algorithm may miss some smaller particles. In this work, the size of the topographic structure element is gradually increased. For each size, the watershed algorithm and shape identification are performed. The resulting image is sent to the next iteration until reasonable particle shapes are identified. Figure 4.6 illustrates the effects of

each procedure in the algorithm. For this example, eight iterations are used to obtain the final image.

| (a) After pre-processing | (b) Image binarization | (c) Watershed of 5th erosion |

| (d) Watershed of 7th erosion | (e) Watershed of 8th erosion | (f) Final segments |
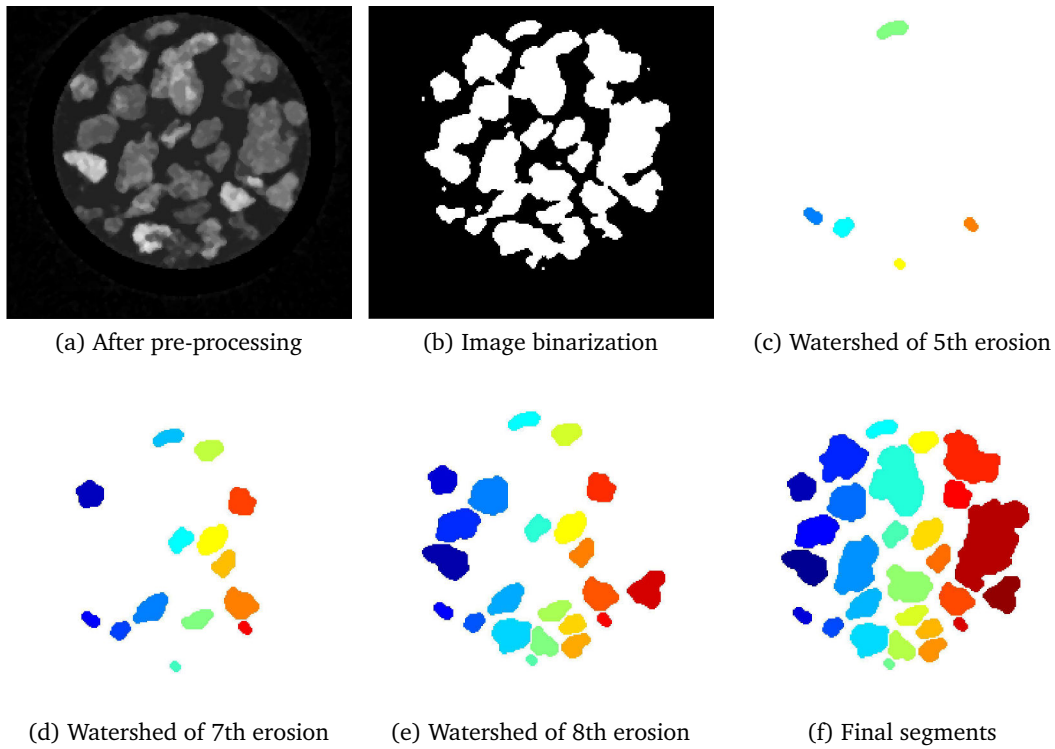
Figure 4.6: An illustration of particle identification from a pre-processed CT image.

4.4.3 Quantitative description of particle shapes

With particle shapes identified and extracted following techniques described in the previous section, it is possible to calculate quantitative descriptors of particle shapes within a specimen. In this work, three shape descriptors are calculated, i.e., the Fourier harmonic descriptor, the aspect ratio, and the circularity.

Fourier harmonic descriptor When using the Fourier harmonic descriptor, the polar radius r of a particle is written as a function of the polar angle θ through a series of Fourier

harmonic functions such that (Das, 2007; Mollon and Zhao, 2012)

$$r_N(\theta) = \frac{R_o}{2} + \sum_{n=1}^{N}[a_n\cos(n\theta) + b_n\sin(n\theta)] \qquad (4.5)$$

where R_o is the equivalent particle diameter of a spherical or circular particle that has the same area as the irregular particle; $N \geq 1$ is the Fourier series order; a_n and b_n (with $n = 1, 2, 3, ...N$) are the Fourier coefficients defined as

$$a_n = \frac{1}{\pi}\int_0^{2\pi}[r(\theta)\cos(n\theta)]d\theta \qquad (4.6)$$

$$b_n = \frac{1}{\pi}\int_0^{2\pi}[r(\theta)\sin(n\theta)]d\theta \qquad (4.7)$$

In this work, Fourier coefficients are evaluated for a total of 297 particle shapes extracted from CT images. To compare between particles of different sizes, the coefficients (a_n, b_n) are normalized by the equivalent particle diameter R_o. Furthermore, a normalized mean amplitude is calculated as the square root of the sum of the normalized coefficients squared. The normalized amplitude versus the harmonic number plot is shown in Figure 4.7, where the harmonic number $n = 1, 2, 3, ..., N$ and $N = 15$ for this study.
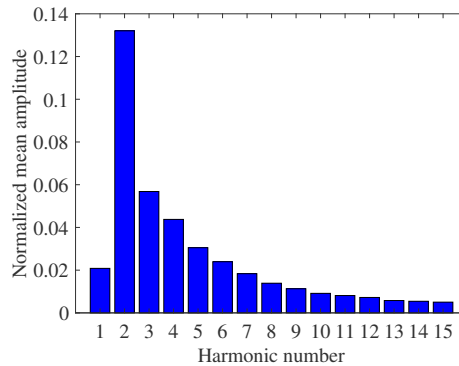
Figure 4.7: Fourier harmonic descriptor for all particle shapes extracted from CT images.

Aspect ratio Aspect ratio is defined as the ratio of the short axis to the long axis. For a circular particle, the aspect ratio would be one. Figure 4.8a shows the aspect ratio distribution of the particle shapes extracted from CT images. The mean aspect ratio is about 0.57.

Circularity Circularity describes the degree to which a particle shape is similar to a circle, and it is a measure of both the particle form and roughness (Olson, 2011). The circularity of a particle is a dimensionless quantity given as (Olson, 2011)

$$C = \sqrt{\frac{4\pi A}{P^2}} \tag{4.8}$$

where A is the area of the particle; P is the perimeter defined as the total length of the particle boundary. A higher circularity value means the particle is closer to a perfectly round and smooth particle. An ellipse with an aspect ratio of 0.57 has a circularity of about 0.92. Figure 4.8b plots the histogram of the circularities of the scanned specimen. The mean circularity is about 0.86.

(a) Aspect ratio   (b) Circularity
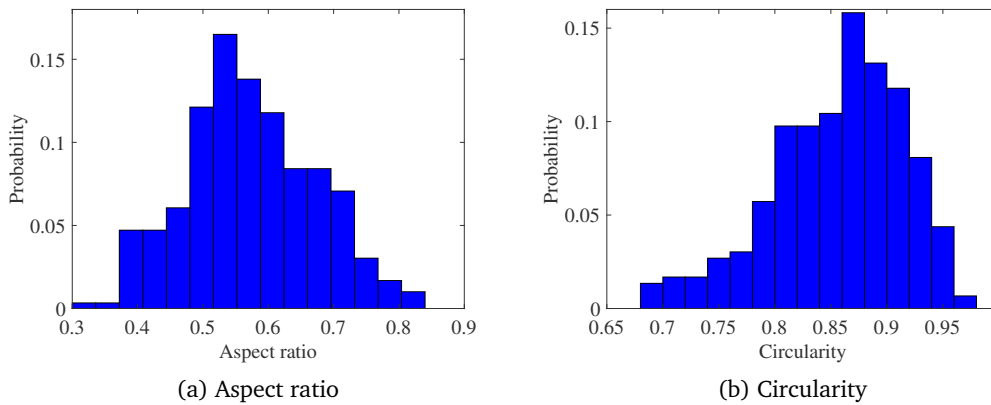
Figure 4.8: Particle shape descriptors of the extracted particle shapes.

The particle shape descriptors can be used to generate numerical particle assembly that possesses similar shape properties of a corresponding physical particle assembly or to quantify the relationship between macroscopic material properties (e.g., shear strength) and

particle shapes Härtl and Ooi (2011). A more direct approach, as adopted in this work, is to generate particles with realistic irregular shapes using extracted particle shape data from CT images. In the next section, a subset of realistic particle shapes extracted from CT image will be used to illustrate the development of a grading and shape-dependent discrete element model.

4.5   Discrete element model

In this section, two-dimensional (2D) discrete element model will be developed to simulate the behavior of the JSC-1A MRS. The model explicitly accounts for particle size distribution and realistic irregular particle shapes extracted from CT images. Despite the limitations of a 2D numerical model, the procedure presented for model development is general. The developed model can capture microscopic behavior between regolith particles and the responses of the system with reasonable computational time.

4.5.1   Contact models

In a discrete element model, the microscopic interactions between particles are simplified into contact behavior of two elements. The contact force $\boldsymbol{F}_c$ consists of two parts: the normal force $\boldsymbol{F}_n$ and the shear force $\boldsymbol{F}_s$

$$\boldsymbol{F}_c = \boldsymbol{F}_n + \boldsymbol{F}_s = F_n \boldsymbol{n}_n + F_s \boldsymbol{n}_s \tag{4.9}$$

where $\boldsymbol{n}_n$ and $\boldsymbol{n}_s$ are the unit vectors denoting the direction of the normal and the shear force, respectively; F_n and F_s are the magnitudes of corresponding contact forces. Assuming the relative displacement increment at the contact during a timestep Δt is given by its components $\Delta \delta_n$ and $\Delta \delta_s$, the contact law for a simple linear model updates the contact

forces through

$$F_n = F_n^0 + k_n \Delta\delta_n \tag{4.10}$$

$$F_s = \min(F_s^0 + k_s \Delta\delta_s, \mu_c F_n) \tag{4.11}$$

$$M = 0 \tag{4.12}$$

where F_n^0 and F_s^0 are the normal and the shear force at the beginning of the current timestep, respectively; k_n and k_s are the normal and the shear stiffness, respectively; μ_c is the microscopic friction coefficient, and M is the contact moment.

In Equation 4.11, an incremental displacement formulation is used to calculate the tangential force to avoid the "ghost force" issue when the accumulative shear displacement is too large and needs a long time for relaxation during the simulation. Alternatively, a modification of the original Cundall and Strack Cundall and Strack (1979) force was proposed by Brendel and Dippel (1998) and adopted in Alonso-Marroquín and Herrmann (2002), which "freezes" the shear displacement when the shear force reaches a given threshold.

A more complex contact law may include rolling resistance such as the one proposed in Iwashita and Oda (1998); Jiang et al. (2005), where a term of rolling resistance moment is added to the contact moment as

$$M = \min(M^0 + k_r \Delta\theta_b, \mu_r \bar{R} F_n) \tag{4.13}$$

where M^0 is the contact moment at the beginning of the current timestep; $\Delta\theta_b$ is the relative bend-rotation increment; μ_r is the rolling resistance coefficient; k_r is the rolling resistance stiffness defined as:

$$k_r = k_s \bar{R}^2 \tag{4.14}$$

where $\bar{R}$ is the contact effective radius defined as $\bar{R} = 1/(\frac{1}{R_1} + \frac{1}{R_2})$, in which R_1 and R_2 are the radii of the contact particles. If one side of the contact is a wall, the corresponding radius $R_2 \to \infty$.

It should be noted that the adopted rolling resistance model of Equation 4.13 uses a simplified formulation for the rolling kinematics, and the particle size effects on the rolling resistance are implicitly incorporated in the rolling stiffness term. The interested reader is referred to Luding (2008); Wang et al. (2015) for examples of improved and more advanced rolling resistance models.

The rolling resistance model can be used to indirectly account for effects of irregular particle shapes and to improve predictions of a discrete element model with only circular particles. As a comparison, discrete element models with circular particles and rolling resistance will also be implemented and compared with the shape-dependent model.

4.5.2 Particle size distribution

In a discrete element simulation, the computational cost is positively correlated to the number of particles in the model. Though the MRS contains only a small amount of fine particles (less than 10% by weight), the number of fine particles can be prohibitively large. When setting up a discrete element model, within the limits of the current computational resources, it may become necessary to introduce some reasonable approaches to modify the particle size distribution, so that the total number of particles can be reduced. Two approaches can be used to reduce the number of particles: up-scaling of particle sizes Kim et al. (2012); Wang et al. (2014a); Feng et al. (2017a), and modifying the gradation by trimming fine particles.

For soil samples with a broad range of particle sizes like the MRS, up-scaling of particle sizes may not be appropriate: a small scaling factor could be insufficient to significantly reduce the number of particles, and a large scaling factor might result in unrealistically large particles. With the trimming approach, fine contents are considered to have negligible contributions to the mechanical strength of the sample, and therefore, they can be "trimmed" or removed.

Considering the wide range of particle sizes and the powder-like tiny particles in the MRS, the particle trimming method is adopted to reduce the particle number in this

work. For the particles that are smaller than 0.425 mm, they are substituted with alternative particles whose size are equal to 0.425 mm. However, the number of alternative particles will be recalculated so that the resulting particle packing has the same volume fraction as the original specimen.

4.5.3   Particle shape representation

Many methods have been proposed and developed to simulate irregularly-shaped particles, e.g., the disc clump method Das (2007); Shi et al. (2015), the spheropolygon (2D) and spheropolyhedron (3D) method Dobrohotoff et al. (2012); Alonso-Marroquín and Wang (2009), the polyhedrons method Mack et al. (2011); Govender et al. (2014), the non-uniform rational basis splines method Andrade et al. (2012b), the level set method Kawamoto et al. (2016) and so on. In this work, an irregularly-shaped particle is modeled using a group of discs called a clump. The most notable advantages of this method are its computational efficiency and straightforward implementation of contact detection algorithms. There are three options to represent a clump (Shi et al., 2015): the domain overlapping filling method, the domain non-overlapping filling method, and the boundary filling method, as shown in Figure 4.9. The clump generated by domain overlapping filling requires the least number of particles and is, therefore, the most computationally efficient. The clump created by the domain non-overlapping filling can also be promoted to a cluster that can capture the breakage behavior. The boundary filling method, depending on the size of filling elements, could provide a better representation of surface roughness.

The domain overlapping filling method is adopted in this work. This approach is also called the Overlapping Discrete Element Cluster (ODEC) method, and the filling process consists of three main steps (Das, 2007): image matrix parameterization, topological skeletonization, and optimum overlapping, as illustrated in Figure 4.10. It should be noted that the irregularly-shaped particles generated by the ODEC method are actually clumps (those that do not break), but the phrase ODEC is kept in this work as it was originally used in (Das, 2007).

(a) Domain overlapping filling   (b) Boundary filling   (c) Domain non-overlapping filling
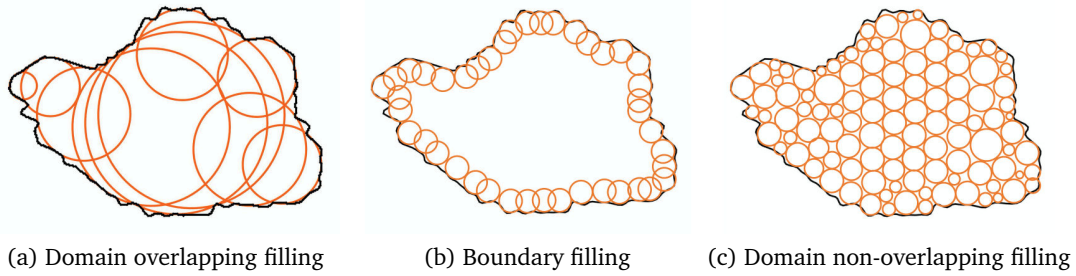
Figure 4.9: Schematic illustration of the three options for representing an irregularly-shaped MRS particle with disc clump method (modified after Shi et al. (2015)).

In the image matrix parameterization, the particle shape is converted to binary image matrix, with status labels indicating particle pixels and background pixels. The binary images are collections of binary pixels that signal whether a square area (or a cubic volume in 3D) is occupied by solid (b = 1) or by void (b = 0). Topological skeletonization, or Medial Axis Transformation, is used to identifying skeleton of a particle, which is defined as the locus of centers of all maximally inscribed discs. In optimum overlapping, discs are iteratively added to the clump. For each iteration, the center of the new discs to be added is searched on the topological skeleton, and it is assured that the newly added disc can cover the maximum uncovered area.

(a) Binary image matrix   (b) Topological skeleton   (c) Optimum overlapping   (d) Resultant clump
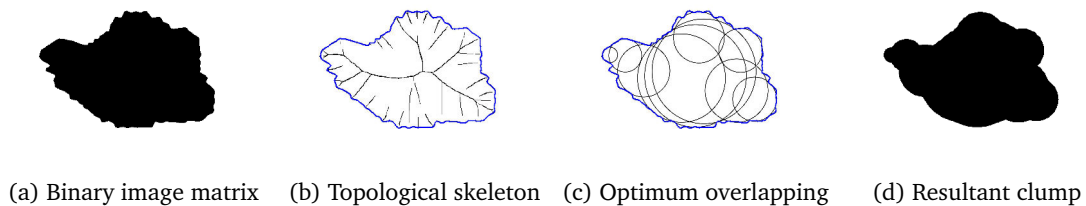
Figure 4.10: Schematic illustration of particle shape representation with domain overlapping filling method.

When applying the ODEC algorithm to irregularly-shaped particles (i.e. non-circular or non-spherical particles), as the number of discs used per clump increases, the percentage of covered area also increases. Figure 4.11 shows the relation of the percentage coverage and the number of discs per clump based on CT image data of the MRS. A clump with a

larger number of discs would have a better representation of the particle shape but with higher computational cost. In this work, each clump is filled by five discs, corresponding to an 80% area coverage. Each clump represents an irregularly-shaped particle.

In the following analysis, seven irregular particle shapes are selected and, therefore, there are seven clump templates used in developing the discrete element model. These seven shape templates are shown in Figure 4.12. The seven types of particle shapes are imported into the discrete element model as clump templates. Each generated particle in DEM model is based on a randomly selected clump template with its size following the particle size distribution described in the previous subsection.
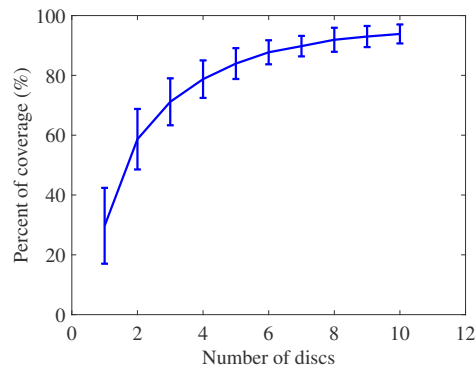
Figure 4.11: The percentage coverage as a function of discs number in the domain overlapping filling method. The error bars indicate the variation of the percentage coverage among different particle shapes when the same number of discs are used.

Figure 4.12: Seven basic particle shapes used in the DEM model.

4.6 DEM simulation of direct shear tests

4.6.1 Model details and material parameters

The grading and shape-dependent DEM model is used to simulate direct shear tests on JSC-1A MRS. PFC2D Itasca Consulting Group, Inc (2014) is used to implement the model and to perform simulations. The dimension of the soil specimen is 63.5 mm in width and 25.4 mm in height. The porosity of the packing in the DEM model is 0.22, which corresponds approximately to a porosity of 0.49 in a three-dimension sample following the parabolic equation recommended by Wang et al. (2014b).

To generate a numerical specimen following the prescribed particle size distribution with irregularly-shaped particles, the following steps are taken:

1. The particle size distribution (PSD) curve is first divided into a number of bins. In this work, the number of bins and bin sizes are set based on the number of sieves and sieve openings used in the laboratory sieve analysis.

2. The area of particles in each bin is calculated based on the total volume of the specimen and the target porosity.

3. Within each PSD bin, a particle size is randomly generated and the corresponding particle shape is randomly selected from the list of irregularly-shaped particles, e.g., Figure 4.12.

4. The previously generated particle is scaled such that its area equals to the area of an equivalent disc with the same particle size.

5. The scaled irregularly-shaped particle is then inserted to the specimen at a randomly selected position.

6. Steps 3 - 5 are repeated for each PSD bin until the total area of the generated particles matches the target area computed in step 2.

7. The generated specimen is allowed to settle under gravity.

It is worth noting that, within the limits of the resolution of the X-ray CT system, the particle shapes at different particle sizes are not directly obtained. Herein, the particle shape or shape descriptors are assumed to resemble each other at different sizes, known as the fractal phenomenon of granular material Arasan et al. (2011). Therefore, the same shape templates are used at different scales in generating the numerical specimen.
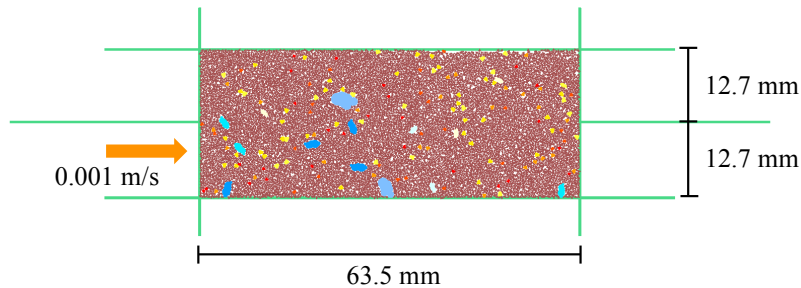
Figure 4.13: Discrete element model of a direct shear test specimen. Light green lines represent the shearing cell and different colors are used to indicate particles with different sizes.

The generated numerical specimen is shown in Figure 4.13. During the preparation of soil specimen in the laboratory test, the specimen is vibrated and slightly compacted to remove potential cavity and improve sample homogeneity. In the numerical simulation, for the same purpose and during the specimen preparation stage, the shearing cell is set to be frictionless, and the friction coefficient of soil particles is set to be 0.1. The input parameters for the DEM model are calibrated using one set of laboratory test data corresponding to a confining stress of 95.8 kPa , following a calibration procedure similar to Belheine et al. (2009); Plassiard et al. (2009); Behraftar et al. (2017). The calibrated values are summarized in Table 4.3. Then, the other sets of test data are used to validate simulation results of the DEM model.

The direct shear test consists of two stages: consolidation and shearing. In the numerical simulation, the movement of the shearing cell is governed by servo-control mechanism Itasca Consulting Group, Inc (2014) to achieve and maintain a specified consolidation pressure. Three different confining stresses, i.e., 95.8, 191.5 and 383 kPa, are considered. The time step is set at 2×10^{-6} s. In the shearing stage, the lower part of the shearing cell

Table 4.3: Input parameters for the DEM model.

Parameter	Value
Width of shear cell w	63.5 (mm)
Height of shear cell h	25.4 (mm)
Packing porosity ϕ	0.22
Density of particles ρ	1940 (kg/m^3)
Contact normal stiffness k_n $\star$	1.5×10^7 (N/m)
Contact shear stiffness k_s $\star$	1.5×10^7 (N/m)
Friction coefficient of particles μ_c^b $\star$	2.5
Friction coefficient of boundary μ_c^w $\star$	2.0
Rolling resistance coefficient μ_r $\star\star$	0.7

$\star$ denotes the parameters that need to be calibrated.
$\star\star$ is the rolling resistance coefficient required if using simplified disc only particles with the rolling resistance contact model to account for particle shape irregularity.

is moved at a speed of 0.001 m/s. The simulation is stopped when the normalized shear displacement reaches 12% or the shear stress reaches its peak and significantly decreases.

4.6.2 Results and discussion

Figure 4.14a shows the shear stress and shear displacement behavior of the MRS in the direct shear test. The results from the developed discrete element model match reasonably well with the experimental data, and the peak shear stress can be perfectly captured. The shear stress from DEM model exhibits a more significant decrease in the post-peak stage compared to the laboratory experiment. The post-peak difference between the DEM and experiment results, as being previously observed in Wang et al. (2014a); Feng et al. (2017a), may come from the particle breakage effect that is not included in the DEM model. In addition, the simplification of a 3D problem into a 2D DEM model also contributes to the differences. Nevertheless, the DEM simulation predicts a maximum macroscopic friction angle of 40°, which matches very well with the value obtained from lab test (41.4°±2.2°).

As a comparison, two additional cases of DEM simulations are performed. The first case uses the same input parameters for the linear contact law and the same gradation but

(a) Stress displacement behavior

(b) Normal and shear stress at failure
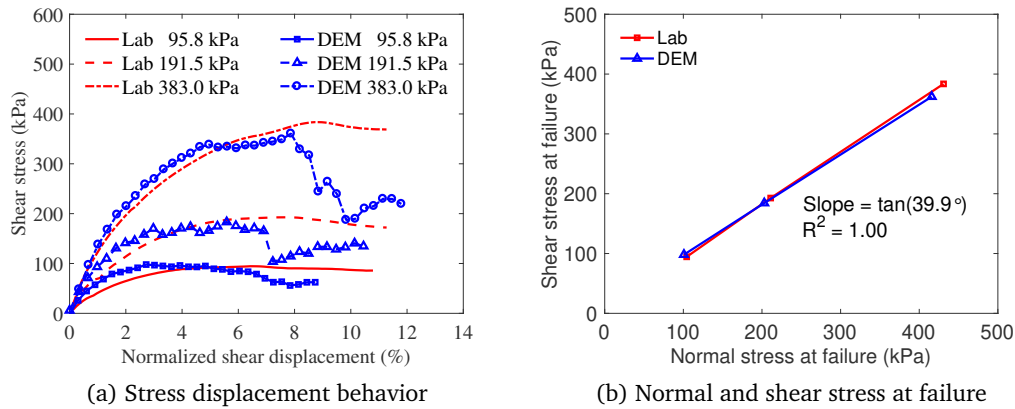
Figure 4.14: Grading and shape-dependent DEM simulations of direct shear test: stress response and comparison with laboratory test.

with simple disc-shaped particles, i.e., no consideration of particle shapes. The second case also uses disc-shaped particles but incorporates the rolling resistance model of Equation 4.13.

Figure 4.15 shows stress responses of DEM simulation with disc-shaped particles. For such a case, the maximum macroscopic friction angle is 27.2°, and the corresponding friction coefficient is about 40% less than the value obtained with shape-dependent DEM simulations. This comparison shows that the particle shape irregularity makes a significant contribution to the shear strength of this material.

Figure 4.16 plots the stress responses of disc-shaped particles with the rolling resistance model of Equation 4.13. In this case, a rolling resistance coefficient μ_r of 0.7 is required to achieve the same shear strength predicted using the shape-dependent DEM model.

Figure 4.17 shows the formation and evolution of shear band (characterized by particle rotations) for all three cases of DEM simulations. Two main distinct effects of particle shape irregularity on the shear band can be observed: (1) the particle shape irregularity tends to resist or inhibit the shear band formation; and (2) the particle shape irregularity could induce additional shear band in a direction other than the common horizontal direction.

Previous study Härtl and Ooi (2011) has found that particle shape irregularity could increase the coordination number and increase the mobilized particle contact friction, leading to a larger macroscopic friction angle. A similar phenomenon is captured by the grading and
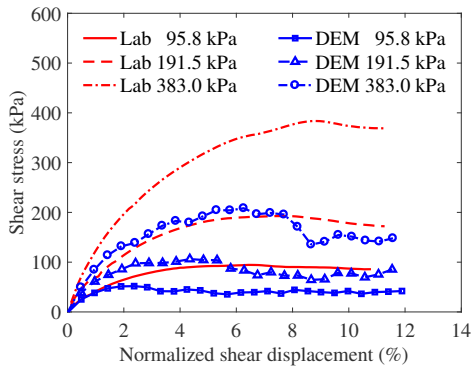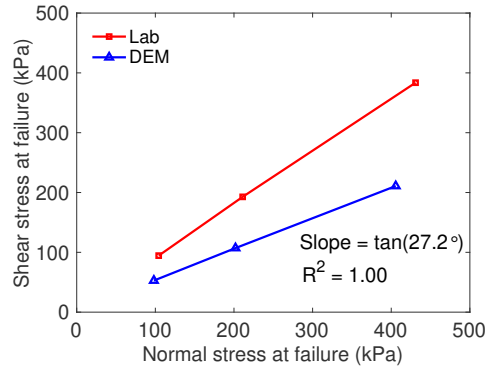
(a) Stress displacement behavior (b) Normal and shear stress at failure

Figure 4.15: DEM simulations of direct shear test with disc-shaped particles and a linear contact model: stress response and comparison with laboratory test.
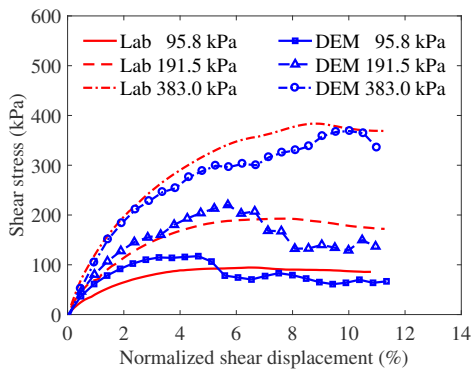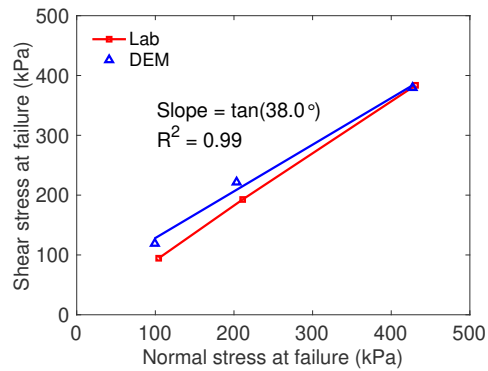
(a) Stress displacement behavior (b) Normal and shear stress at failure

Figure 4.16: DEM simulations of direct shear test with disc-shaped particles and a rolling resistance contact model: stress response and comparison with laboratory test.
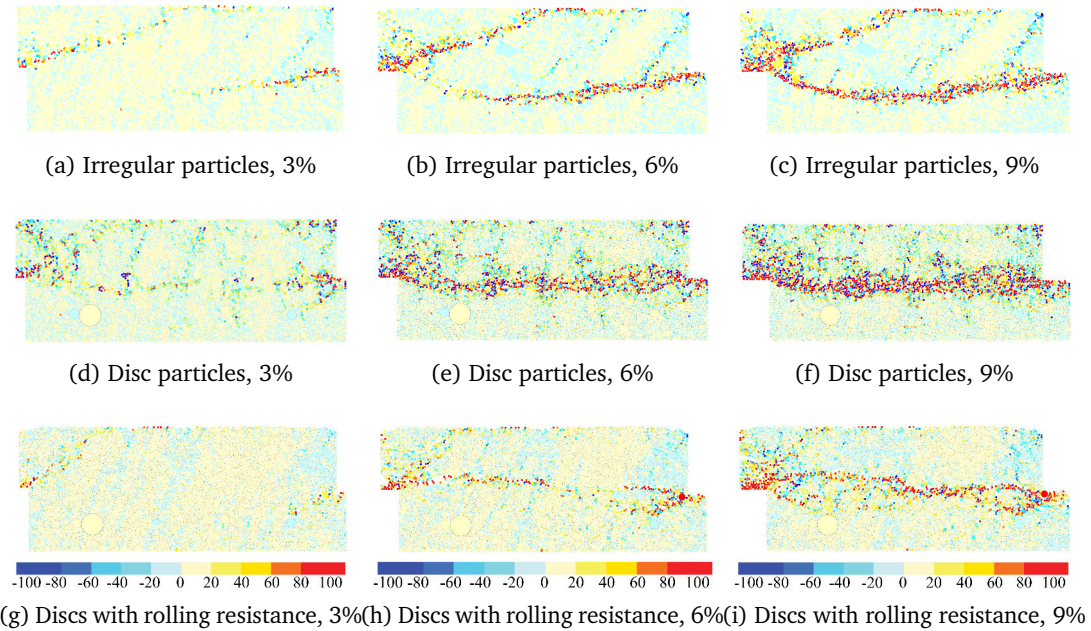
Figure 4.17: Shear band in numerical DST at 3%, 6% and 9% shearing displacement with normal stress 95.8 kPa. The color indicates the rotation of the particle. The unit of the color bar is in degree with a counterclockwise rotation being positive.

shape-dependent DEM model developed in this work. Here, the coordination number can be directly related to the total contact number in the model, since the particle number in DEM specimens are the same. Figure 4.18 shows the polar histogram of the contact force directions in the specimens at peak shear stress state with a normal stress of 95.8 kPa. It can be observed that the specimen with irregularly-shaped particles possesses the largest number of contacts. It is also interesting to note the anisotropic nature of the contact network for three different cases, which could affect the macroscopic material response. For instance, the dependence of elastic constants on the contact network has been reported and quantified in Alonso-Marroquin et al. (2005). The contact forces directed close to horizontal give a higher shearing resistance in the direct shear test. The contact force directions cluster around 30° for the specimen with irregularly-shaped particles and the specimen with discs and rolling resistance. The contact force directions cluster around 45° for the specimen with disc-shaped particles and no rolling resistance. Results of the mobilized contact friction in each specimen

82

are shown in Figure 4.19. Consistent with the previous study (Härtl and Ooi, 2011), the specimen with irregularly-shaped particles possesses the largest percentage of mobilized particle contact friction that is greater than the macroscopic friction ($\tan 40°$).

(a) Irregular particles   (b) Disc particles   (c) Discs with rolling resistance
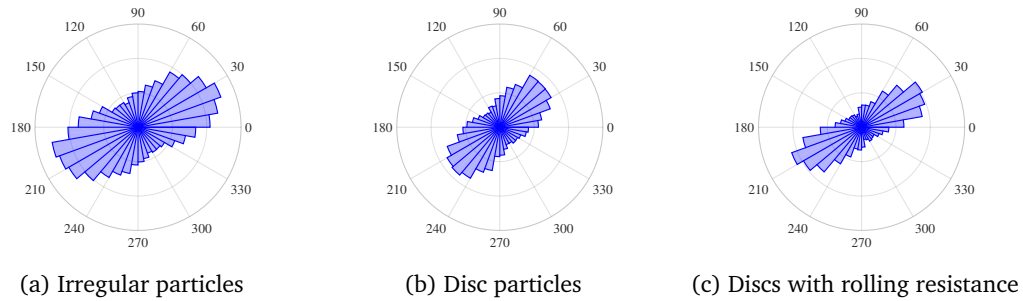
Figure 4.18: Polar histogram of the contact direction at peak shear stress with a normal stress of 95.8 kPa.

(a) Irregular particle   (b) Disc particles   (c) Discs with rolling resistance
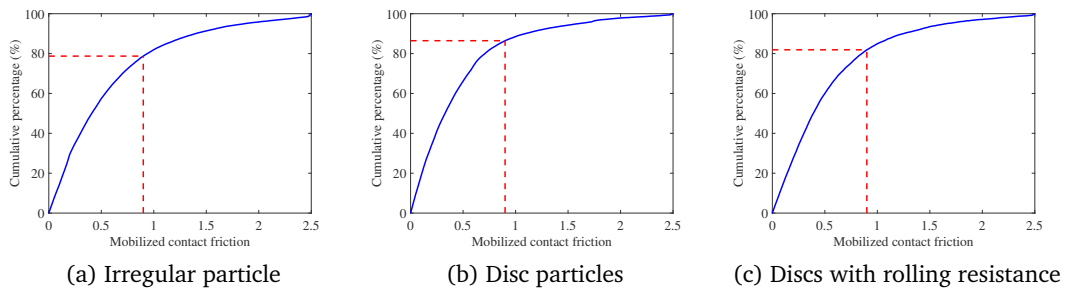
Figure 4.19: Cumulative frequency of mobilized contact friction coefficient for all contacts at peak shear stress with a normal stress of 95.8 kPa. The red dashed line indicates the mobilized contact friction corresponding to $\tan 40°$, where 40° is the maximum macroscopic friction angle obtained from DEM simulations with irregular particles.

4.7 Conclusions

In this work, the physical and mechanical properties of JSC-1A MRS are characterized by a series of laboratory tests. The properties characterized include specific gravity, particle size, particle size distribution, particle shapes and shear strength. X-ray computed tomography is used to obtain particle images, upon which particle shape data are characterized by a series of imaging processing techniques and are further used to generated irregularly-shaped

numerical particles through the domain overlapping filling method. A grading and shape-dependent DEM model is then developed, calibrated and validated against direct shear tests on JSC-1A MRS. In summary, it is found that

1. The JSC-1A MRS used in this study can be characterized as well-graded sand (SW) following the Unified Soil Classification System with a specific gravity of 1.94 ± 0.02.

2. The calibrated grading and shape-dependent DEM model can capture the behavior of the regolith simulant in a direct shear test, in particular, the peak shear strength and the maximum friction angle.

3. The particle shape effect accounts for approximately 40% of the shear resistance of the JSC-1A MRS. The irregular particles would increase the mobilized contact friction and the number of particle contacts within the assembly when compared with an assembly with the same number of disc-shaped particles.

4. The additional shear resistance resulting from irregular particle shape effect cannot be fully replicated by solely increasing the micro friction between particles but can be captured through a calibration of rolling resistance contact model.

The laboratory characterization and numerical model developed in this work provide insights into the mechanical behavior of JSC-1A MRS from a fundamental level. The calibrated grading and shape-dependent model can be a useful tool for simulating and predicting regolith behavior in a complex environment such as microgravity and low pressure, which will be explored in future studies.

Chapter 5

Discrete element modeling of deformable pinewood chips in cyclic loading test

The design of efficient lignocellulosic biomass feedstock systems is challenging, as current laboratory characterization and design methods were developed primarily for fine powders with relatively low compressibility. The discrete element method (DEM) is gaining prominence as an alternative method for modeling the bulk flow and transport of particulate materials in hoppers and feeders. However, prior DEM simulations investigating the flow of wood chips modeled the particles as simple rigid geometries such as spheres, rods or blocks, and neglected the effects of particle deformability and irregular shapes. As a consequence, those simplified DEM models may not provide enough key diagnosis to help improve the design of biomass feeding and handling equipment. This work presents a bonded-sphere DEM approach for characterizing the mechanical behavior of bulk flexible, deformable pinewood chips in a cyclic stress loading test. Clustered spheres that can bend and twist via

A similar form of this chapter has been submitted at the time of writing: Y. Xia, Z. Lai, T. Westover, J. Klinger, H. Huang, and Q. Chen. Discrete element modeling of deformable pinewood chips in cyclic loading test.

elastic bonds are used to model irregular-shape particles in real pinewood chip samples. An axial compression tester, which contains 0.06 million bonded-sphere particles (1.35 million spheres) in a quarter cylinder, is simulated with a domain size similar to the experiments. With careful calibration, the simulations have delivered the bulk densities and the bulk moduli of elasticity that are in good agreement with those measured in the corresponding experiments. However, it is also been found challenging for the present DEM model to accurately predict the overall stress-strain behavior of bulk pinewood chips, especially the large sustained plastic deformation during unloading. Additional numerical tests have shown that the adjustment in certain contact parameters (e.g. bond stiffness) can lead to profound solution improvement, but meanwhile will induce extra challenges such as increased computing time. Future work will include an elasto-plastic particle bond model to enhance the simulation fidelity.

5.1 Introduction

Loblolly pine forest residues are a low-cost source of biomass for conversion into biofuel or biochemical (Office, 2016). Research efforts on instrumented laboratory characterization of bulk mechanical and rheological properties of wood chips have been on the rise recently (Stasiak et al., 2015; Hernandez et al., 2017), in part because of a growing need for the design of more efficient and durable feedstock systems in biorefinery (e.g. grinder, hopper and feeder). However, a number of limitations have been observed in the current experimental approaches for measuring the required material properties and designing equipment to robustly handle biomass, including residues (Westover and Hartley, 2018). In general, the current quantitative methods to design equipment to handle particulate materials were originally devised for powder materials that are relatively incompressible, and that are handled at consolidation pressures larger than about 2 kPa. In many cases, the processes that handle lignocellulosic biomass for biofuels applications do not meet these criteria, and hence often result in various handling problems (Barletta and Poletto, 2013;

Hernandez et al., 2017). For a limited range of applications, the purely empirical methods may be used to successfully design equipment by performing laboratory tests using conditions that are similar to those expected in industrial operations. However, a direct extension of those empirical methods to a wider range of conditions is unlikely practical due to the large number of variables, especially when many of the variables are nonlinearly related. The limitations found in the current experimental and empirical methods indicate that these methods alone do not suffice to satisfy the requirements in biomass characterization. Biomass particles such as processed pinewood chips usually exhibit 1) a wide range of sizes and 2) high complexity of shapes, and are often subject to large deformation and breakage in biomass feedstock refinery and transport processes. Figure 5.1 displays representative loblolly pine forest residues that have been hammer-milled with a 25 mm screen. The shapes of individual particles are mostly irregular, with a wide range of sizes from a few millimeters to approximately a centimeter. It is well established that particle shape and size distributions are salient factors that can significantly affect the bulk behavior of particulate materials (Höhner et al., 2012). Another factor is that pine chips are relatively soft and can deform considerably even at low stress loading. Predicting the behavior of pinewood chips in feeding and handling processes requires consideration of the above factors to ensure model fidelity.

Figure 5.1: Loblolly pine forest residues after being hammermilled with a 25 mm screen.

Originally introduced by Cundall and Strack (1979), the discrete element method (DEM) refers to a class of computational models that are widely used for the predictive modeling of the bulk behavior of particulate materials. DEM is similar to molecular dynamics in that it explicitly tracks the motion and often deformation of each particle in the flow field. A review on the major DEM models and applications is reported by Zhu et al. (2008). Moreover,

the recent progress in the DEM comminution modeling of mineral ores is summarized in Weerasekara et al. (2013), while Horabik and Molenda (2016) have reviewed DEM research for agricultural granular materials. Most DEM simulations assume spherical, monodisperse particles because the contact detection and force calculations are simplest and achieve the best scaling in parallel computing. Rackl et al. (2017) modeled wood chips as mono-sized spheres in DEM in order to decrease model complexity and reduce simulation time. To compensate the loss of accuracy for using simple spheres, other work adapted the rolling friction parameters of the DEM contact law in spheres to partially mimic the particle shape effects (Wensrich and Katterfeld, 2012). However, the impact of particle shapes and sizes on the bulk flowability was not further explored. Wood chips have also been modeled with simple non-spherical shapes, such as polyhedron (either ideal or round-edged) and superellipsoids (Cleary and Sawley, 2002; Coetzee, 2017; Ma et al., 2017). For example, Scherer et al. (2016) modeled wood chips as single-body polyhedral particles in a rotary drum. However, their studies did very limited investigation of the impact of particle shape and size on simulation results. To approximate particles with more complex and irregular shapes, two DEM models: the multi-sphere model (Abbaspour-Fard, 2004; Kruggel-Emden et al., 2008) and bonded-sphere model (Zhong et al., 2016) are most often used, as shown in Figure 5.2. In the multi-sphere model, many spheres are "glued together" to approximate a rigid, unbreakable particle. Although the model was also applied for modeling certain kind of wood chips (Maione et al., 2015), it is apparently not suitable in our case, since it does not consider particle deformability – a factor that significantly affects the bulk flow behavior of pinewood chips (e.g. see Figure 5.3). An alternative model, namely the bonded-sphere model, which was initially devised for modeling fracture initiation and evolution across mineral grains in rock (Cho et al., 2007), can also be used to approximate individual complex-shape particles. In the bonded-sphere model, a particle shape is approximated with a cluster of spheres where each sphere is connected to neighboring spheres with beam like bonds that can be elastically deformed and broken. By adjusting the size and masses of the sphere clusters, the size, shape and mass distributions of pinewood particles can be

modeled. The bonded-sphere model is so far the most robust and scalable model in DEM for simulating particulate systems consisting of arbitrarily shaped and deformable particles, despite some known weaknesses when compared with certain specialized models such as the sphero-cylindrical flexible fibre model (Guo et al., 2013, 2015, 2018) for bendable crop stems (Lenaerts et al., 2014; Langston et al., 2015; Leblicq et al., 2016b,a).
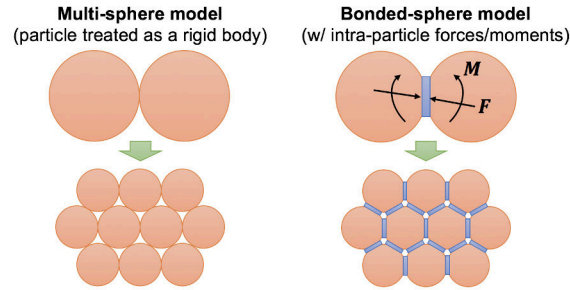
Figure 5.2: Illustration of the multi-sphere model (left) and the bonded-sphere model (right).
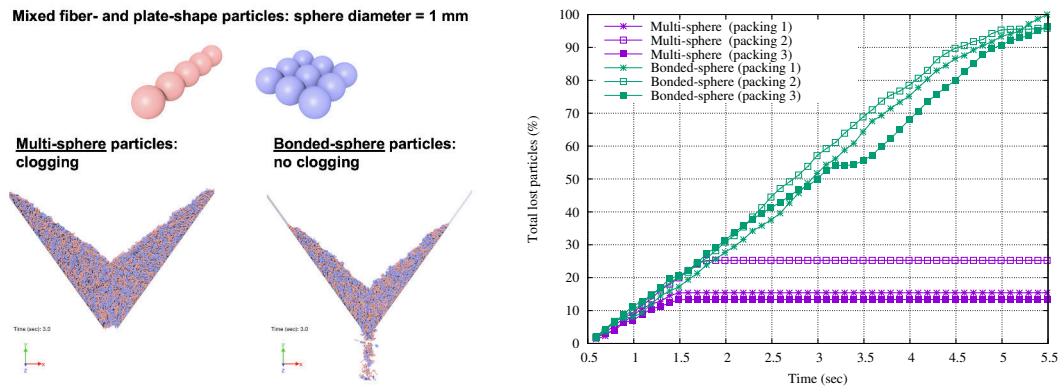
Figure 5.3: DEM hopper simulation examples that used multi-sphere particles and bonded-sphere particles, respectively.

Our literature survey, however, has also unveiled a wide scientific gap in the DEM modeling of biomass particulate systems. Most earlier works have focused on the bulk rheological behavior of those particulate materials (Oevermann et al., 2009; Höhner et al., 2012; Kruggel-Emden et al., 2012; Höhner et al., 2015; Maione et al., 2015; Schott et al., 2016; Scherer et al., 2016; Maione et al., 2017), but disregarded the impact of external loading on their bulk mechanical properties (e.g. bulk elasticity) and consequently on their

bulk flowability. As of yet, it is unclear what improvements can be made in modeling the mechanical behavior of biomass materials such as wood chips, during hopper flow, auger feeder and grinding operations if particle deformability is considered. Indeed, a quantitative characterization of the bulk mechanical properties of wood particulate materials under external stress loading conditions is a relatively untouched area in DEM modeling. The primary goal of this work is to narrow the aforementioned scientific gap through DEM simulations of bulk wood chips in cyclic compression tests. The particular type of wood chips considered in this work is loblolly pinewood forest residues, as those featured in Figure 5.1. Six DEM clustered-sphere particle shape templates were created to approximately match the particle size and shape distributions of laboratory samples. To account for particle deformability, the bonded-sphere model is employed to model the individual pinewood particles – a major contribution of this work. Numerical compression tests are performed to assess the bulk mechanical properties of pinewood particles under compression. An equivalent laboratory experiment is conducted in this work as a reference for calibrating the DEM model and validating the simulation results. Since there are very few similar simulations in existing literature, this work presents a new insight into the discussed aspects. The developed workflow and methodology can be easily extended to other woody samples as well as other materials with similar physical features such as miscanthus. Follow-on numerical experiments of hopper flow with the calibrated DEM models are planned in the future.

The rest of the paper is organized as follows. Section 5.2 briefly describes the formulation of the bonded-sphere DEM model. Section 5.3 discusses the particle shape conceptualization with the bonded-sphere model. Section 5.4 presents the detailed setup of the compression test in DEM simulations. Section 5.5 reports the simulation results, analysis and suggestion for further improvement. Lastly, a summary of this work is provided in Section 5.6.

5.2 Bonded-sphere DEM model

The concept of DEM is relatively mature and a general formulation of DEM can be found in Cundall and Strack (1979) as well as Chung (2006). In this section, we will present a brief description on the DEM model used in this work. It is not intended to elaborate all aspects of DEM, but rather to provide sufficient background information to present the novel features of the current bonded-sphere DEM model.

5.2.1 Basic formulation

Within the bonded-sphere DEM model, the motion and deformations of all particles are tracked by calculating the force and moment. The bulk behavior of the material is presented as an assembly of the actions (i.e., the interactions and motion) of all constituent particles. Each particle has two types of motion: translational and rotational, which can be described by the Newton-Euler equations. As to the base spheres used in this work, the Newton-Euler equations are written as

$$m\frac{\mathrm{d}^2 \boldsymbol{x}}{\mathrm{d}t^2} = \boldsymbol{F} \tag{5.1}$$

$$I\frac{\mathrm{d}^2 \boldsymbol{\theta}}{\mathrm{d}t^2} = \boldsymbol{M} \tag{5.2}$$

where m and I are the sphere mass and moment of inertia, respectively; $\boldsymbol{x}$ and $\boldsymbol{\theta}$ are the sphere translational and rotational position; $\boldsymbol{F}$ and $\boldsymbol{M}$ are the overall external forces and moments experienced by the spheres; and bold symbols indicate vectors. In order to resolve the motion of each sphere, all the forces/moments experienced by each sphere are first evaluated and summed. A sphere can be subjected to the following typical types of forces/moments: gravity, damping, contact forces, and prescribed external forces. Herein, the damping is particularly referred to the global damping, which is sometimes (artificially) introduced in a DEM model to facilitate energy dissipation and enhance a quasi-static simulation (Chung, 2006; Itasca Consulting Group, Inc, 2014). There is another type

of damping called local damping, which is usually incorporated into the contact forces accounting for the realistic energy dissipation due to collisions. In this work, only the local damping is considered. For the contact forces, typical contact models would be selected aimed at the particular material of interest. The contact models used in this work for modeling deformable pinewood chips will be presented in a subsequent section. Once the sphere forces/moments are obtained, the sphere motion (i.e., Equation 5.2) is then numerically integrated with a fixed timestep size. For the time integration, a commonly adopted approach is the second order Velocity Verlet algorithm (Verlet, 1967). Consequently, the translational and rotational positions as well as the corresponding velocities of each sphere are updated. The evaluation of sphere forces/moments (especially for the contact forces) and the time integration of sphere motion are resolved cyclically at each timestep through the duration of the DEM simulation.

5.2.2   Particle representation and contact models

As aforementioned, the irregular-shape pinewood chips are represented by clusters of spheres using the bonded-sphere model (see Figure 5.2). The bonded-sphere model was initially devised by Potyondy and Cundall (2004) for modeling fracture initiation and evolution across mineral grains in rock. Note that the "bonded-sphere model" was originally referred as "bonded-particle model" in (Potyondy and Cundall, 2004). Here in this work, we will stick to "bonded-sphere model" since spheres are used as the base elements to form an irregular-shape particle, as well to distinguish the particle within "bonded-particle model" from actual pinewood particles. In bonded-sphere model, the spheres in a same cluster (i.e., particle) are connected with "bonds", which can be regarded as special contacts that can carry forces and moments. The bonds connect the spheres as a whole, but also allow them to have relative displacements when subjected to external forces/moments. The particle deformation (e.g., bending or deflection) is then replicated from the overall effects of relative displacements of all the spheres within the cluster (i.e., the particle). In this work, the contact forces are calculated from two types of contact models: linear parallel bond model

([Potyondy and Cundall, 2004](#)) for intra-particle contacts (i.e., the bonds) aiming at capturing the deformation of particles, and Hertz-Mindlin model ([Hertz, 1882](#); [Mindlin, 1953](#); [Di Renzo and Di Maio, 2005](#)) for inter-particle contacts aiming at capturing the collisions between particles. The linear parallel bond model is first proposed by [Potyondy and Cundall](#) ([2004](#)) to analyze rock mechanics. It is simple, but provides constraints to both relative translational and rotational displacements between bonded sphere neighbors. The Hertz-Mindlin contact model is a complete frictional contact model based upon the Hertz theory ([Hertz, 1882](#)) for contact normal forces and the Mindlin theory ([Mindlin, 1953](#)) for contact tangential forces. It takes account of the stiffness variation due to the change of contact areas during the collision of two elastic spheres. The detail formulations of linear parallel bond model and Hertz-Mindlin contact model have been discussed in [Chapter 2](#).

5.3   Characterization of pinewood particles

This section presents a numerical conceptualization of real pinewood particles for DEM simulations. In addition, we will also characterize the mechanical behavior of the resulting individual DEM particles to gain insights into the mechanical properties of those particles.

5.3.1   Particle shape conceptualization

In order to achieve the required fidelity of DEM simulations for predicting the mechanical properties of pinewood particles, the DEM particles need to adequately approximate the shapes and mass distributions of targeted physical materials. Chipped loblolly pinewoods from whole tree debarked chips (pinus taeda) were obtained from TFTX Consulting. The chips were harvested in the fall of 2017 near Brighton, South Carolina, USA, and were then ground using a Schutte-Buffalo hammer mill (Circ-U-Flow model 18-7-300) equipped with a 25 mm screen. After milling, the sample was sieved using a SWECO Vibro Energy Round Separator (Florence, KY, USA; Model ZS24) equipped with 1 mm and 6 mm sieves

to remove large and small particles (i.e. only particles that passed through a 6 mm sieve but did not pass through a 1 mm sieve were used in this study). The sieved samples were divided using rotary or riffle splitters to ensure uniform sample splitting for subsequent tests. Two-dimensional size and shape distributions of the material were obtained using an automated Clemex digital imaging system as described in Hernandez et al. (2017). Though every pinewood particle has a unique shape, most of them can be approximated by some representative shapes such as short stick or thin flake, with maximum length ranging roughly from 5 to 10 mm and maximum width ranging roughly from 1 to 5 mm. This approximation method served as the basis for our particle conceptualization process as follows. In this work, a conceptualization of the sieved pinewood particles resulted in a set of 6 types of irregular-shape DEM particles denoted by A5, A7, B10, B31, C72 and D229, respectively, as listed in Table 5.1. Each particle type consists of a cluster of base spheres, with all the base spheres having the same diameter of 1 mm. In the particle type notations, the letters are used to categorize the particle cross-section shapes, while the numbers are used to indicate the number of base spheres. Particles in categories A, B, C and D have 1, 3, 5 and 7 rows of base spheres, respectively, as described in Table 5.1. For example, a B31 particle comprises of 31 base spheres arranged in three rows, and roughly resembles a flake-shape pinewood particle that is 2.7 mm in width, 3.5 mm in length, and 1.0 mm in thickness. The simulated particle size distributions were selected to be approximately the paricle width and length distributions of the physical pinewood particles, as shown in Figure 5.4. Though we could enhance the particle resolution by using even smaller base spheres (e.g., 0.5 mm in diameter), yet the allowable minimum timestep size for a numerically stable DEM simulation would be reduced by at least 40%, and the total number of spheres would be increased by 5 - 6 times depending on the packing patterns, resulting in a tremendous increase of computing time by 8 - 10 times for a same DEM simulation problem. Notice that even with the current particle resolution, over a million base spheres are required to set up a simulation with domain sizes comparable to that in our laboratory test. This implies a huge computational costs in our DEM simulations anyhow.

Table 5.1: Specification of the six DEM particle types in simulations (W/L is short for width/length).

	Type	Layer (spheres)	Row (spheres)	Effective W/L	Mass ratio
	A5	1 (5)	1 (5)	1.0 / 5.0 [mm]	7.2%
	A7	1 (7)	1 (7)	1.0 / 7.0 [mm]	12.0%
	B10	1 (10)	1 (3), 2 (4), 3 (3)	2.7 / 3.5 [mm]	6.5%
	B31	1 (8) 2 (15) 3 (8)	1 (4), 2 (4) 1 (4), 2 (7), 3 (4) 1 (4), 2 (4)	2.7 / 5.5 [mm]	15.6%
	C72	1 (17) 2 (38) 3 (17)	1 (5), 2 (7), 3 (5) 1 (6), 2 (8), 3 (10), 4(8), 5 (6) 1 (5), 2 (7), 3 (5)	3.5 / 8.0 [mm]	25.8%
	D229	1 (32) 2 (48) 3 (69) 4 (48) 5 (32)	1 (4), 2 (7), 3(10), 4 (7), 5 (4) 1 (5), 2 (8), 3 (11), 4 (11), 5 (8), 6 (5) 1 (6), 2(9), 3 (12), 4 (15), 5 (12), 6 (9), 7 (6) 1 (5), 2 (8), 3 (11), 4 (11), 5 (8), 6 (5) 1 (4), 2 (7), 3(10), 4 (7), 5 (4)	5.2 / 13 [mm]	32.9%
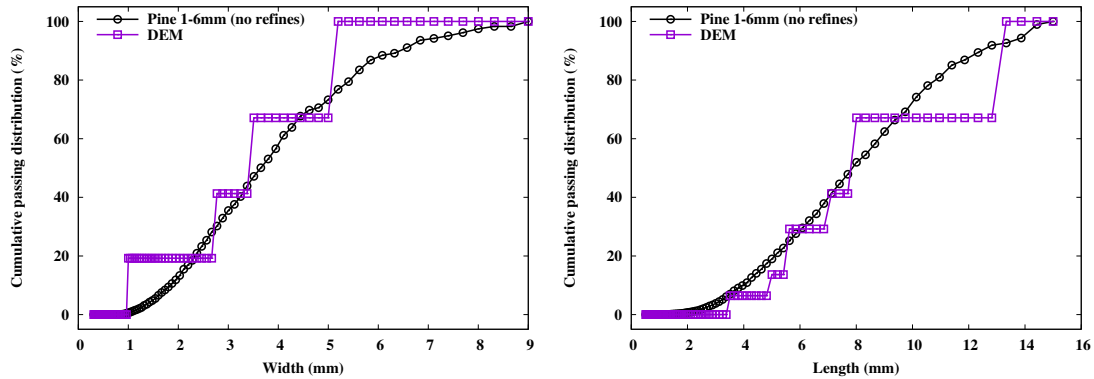
Figure 5.4: Width (left panel) and length (right panel) distributions of physical pinewood particles and DEM particles.

In addition, we conducted a quick validation of the bonded-sphere model by using one A5 particle in a cantilever beam benchmark problem, for which an analytical solution is available for comparison. In this problem, an A5 particle is created with one end sphere fixed, and the other end sphere subject to a constant force perpendicular to the particle length direction. In bond parameter setup, k_n^b is equal to 1×10^{12} N/m^3, while k_s^b is set large enough (i.e., 1×10^{12} N/m^3) to minimize shear displacement between the spheres. The eventual deflection of the particle at equilibrium is recorded and compared to that calculated from the analytical solution. In Figure 5.5, the deflection d of the free-end sphere along the direction of the force, agrees well with the analytical solution, which reads $d = FL^3/3EI$, where the circular cross-section area moment of inertia $I = \pi/4(D/2)^4$ with $D = 0.001$ m, and for the present problem $L = 0.004$ m and $E = 1 \times 10^9$ Pa.
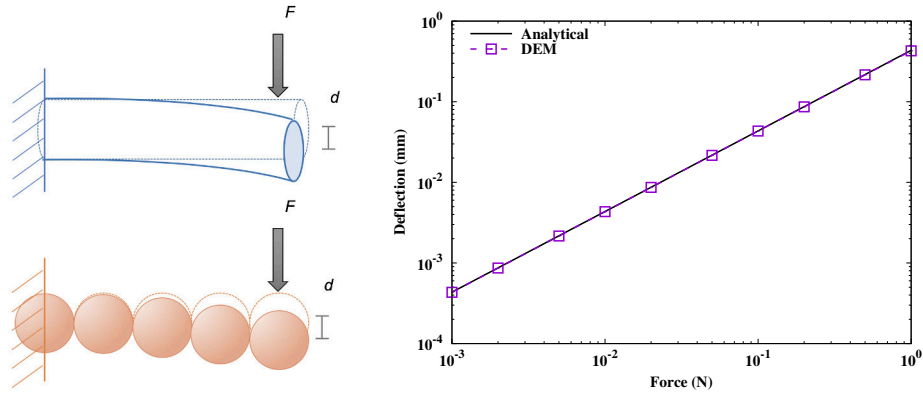
Figure 5.5: Validation of the bonded-sphere DEM model with a cantilever beam bending problem.

5.3.2 Correlation between base spheres and clustered particles

A bulk sample of pinewood particles is inherently a multiscale system. To simulate mechanical behavior of such a system, the bonded-sphere DEM model allows us to characterize the system at three length scales successively from bottom to top: 1) the base sphere scale, 2) the clustered particle scale, and 3) the bulk scale. Because the model's mechanical properties of contact (i.e., the Young's modulus, Poisson's ratio, friction coefficient and bond

stiffness) are defined based on the sphere-to-sphere interaction, no analytical correlation or formula is readily available to link from one scale to another for a system of complex-shape particles, e.g. from the sphere scale to particle scale, or from the sphere scale to bulk scale. While the correlation between the sphere scale and bulk scale is to be explored later in Section 5.5, this section attempts to unveil part of the correlation between the sphere scale and particle scale by using the C72 and D229 particles as examples, as they possess the most complex particle shapes out of the six designed particle types. A bulk of simulated pinewood particles considered in this work contains a large portion of complex-shape particles like C72 and D229. When subject to axial compression, most of the particles in the bulk are unlikely to stay bent like the A5 particle in the cantilever beam bending problem as shown in Figure 5.5. Instead, the majority of the complex-shape particles tend to orient with their longitudinal direction of shapes being normal to the direction of the bulk compressive force (or with a tilt of angle larger than 45°). For example, Figure 5.6 illustrates our observation in part, where the orientations of the C72 and D229 particles are displayed exclusively out of a mix of the six types of particles under a 2 kPa compressive stress loading. Thus we suggest that a more relevant scenario to investigate is when a complex-shape particle is subject to compressive stress normal to its longitudinal direction of shape.

(a) Type C72   (b) Type D229
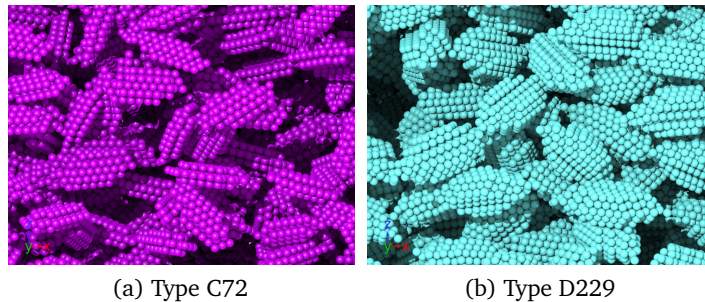
Figure 5.6: Orientations of (a) C72 and (b) D229 particles out of the mixed six types of particles under a bulk compression of 2 kPa.

Now we present a compression test for a C72 particle and a D229 particle, respectively. As displayed in Figure 5.7, the two particles contain three and five layers of base spheres, respectively, along the direction of the external force. The spheres in the top layer were

applied with compressive forces, while the spheres at the bottom layer were fixed. The compressive force was increased consecutively to provide an equivalent stress (i.e., the compressive force divided by the particle effective cross-section area) from 0.5 to 1, 2 ... and eventually 10 kPa, to mimic the range of bulk stress in Section 5.5. For each the compressive stress, the displacements of the spheres in the top layer were recorded and converted to equivalent strains (i.e., the displacements divided by the distance between the loading end and fixed end). Given a range of k_n^b values from 10 to 100 GN/m^3 (while the other contact parameters remained constant), the corresponding stress-strain curves were obtained, as shown in Figure 5.7. From those curves, it is not hard to conclude with a linear correlation between k_n^b and particle's Young's modulus, E_p, for the C72 and D229 particles. For each of the k_n^b tested, the compressive strain of the single particles increased linearly with the external force, indicating that the E_p is constant. For example, when k_n^b is set to 10 GN/m^3, E_p corresponds to 3.74 MPa for the C72 particle and 5.04 MPa for the D229 particle. These E_p values are much smaller than the E_s calculated using an analytical relation for sphere-to-sphere interaction, (i.e. $E_s = k_n^b \cdot d = 10$ MPa, and $d = 0.001$ m), and also appear a few orders of magnitude smaller than the Young's modulus for tight pinewood blocks in literature. In general, for a real pinewood chip particle, the E_p is not geometrically constant, e.g. from surface to interior. Usually, the surface texture of a pinewood chip particle consists of more loose wood fibers and is thus less dense than the inner part of the particle. Hence given the same test for a real pinewood chip particle, the E_p to be measured could be low at the beginning, and become larger with the increase of the external loading. This perspective suggests possible legitimacy for our DEM model to adopt E_p values that can be much lower than the Young's modulus for an actual tight pinewood block. Therefore, considering all these uncertainties, we recommend that a suitable choice of parameters to be eventually used in the DEM-based numerical bulk compression test should still rely on bulk scale calibrations.
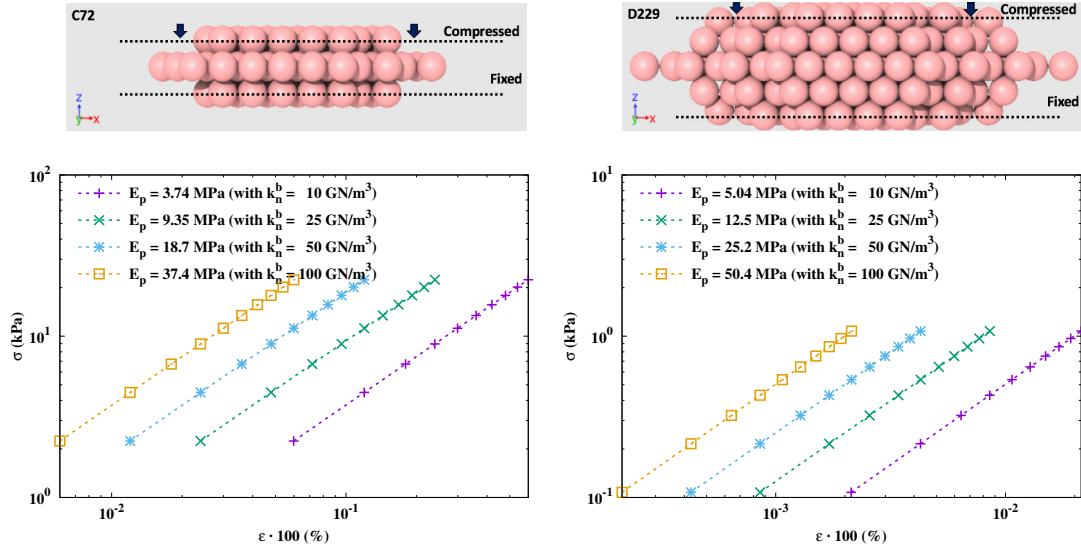
Figure 5.7: Compressive stress-strain curves for an individual particle: type C72 (left graph) and D229 (right graph), respectively, with different bond normal stiffness values, k_n^b.

5.4 Simulation setup

This section describes the two main steps, 1) initial particle packing, and 2) cyclic stress loading and unloading for setting up DEM simulations of a cyclic axial compression test using a mix of the complex-shape flexible particles devised in the previous section. The simulations are designed based on the corresponding laboratory experiment, which is also conducted as reference for the calibration and validation of the current bonded-sphere DEM model.

5.4.1 Initial packing

The reference experiment was conducted in a cylindrical container with a radius of 177.8 mm (7 inches). To minimize the computational cost of simulations, we chose to model only a quarter of the container, with the bottom wall in the $z = 0$ plane, a 150 mm-radius cylindrical wall along the z axis, and two virtual symmetry boundaries in the $x = 0$ plane and $y = 0$ plane, respectively. The bottom and cylindrical walls were treated as frictional walls, while the symmetry boundaries were considered as frictionless walls. Notice that the radius

of the modeled container is nearly identical to that of the physical tests and is approximately 20 times the mean particle length of 8 mm to minimize the domain size effect in simulations. Table 5.2 lists the model's contact parameters used in the present simulations, which are a result of limited parameter calibration on certain parameters, e.g. the E and k_n^b. We applied the same set of model parameters to all the base spheres, in order to alleviate the challenge in DEM model parameter calibration.

Table 5.2: Contact parameters of the DEM base spheres used in simulations.

Parameter	Value	Unit
Young's modulus, E	1×10^7	Pa
Poisson's ratio, v	0.3	-
Coefficient of restitution, e	0.1	-
Particle friction coefficient, μ	0.5	-
Wall friction coefficient, μ_w	0.1	-
Bond normal stiffness, k_n^b	1×10^{10}	N/m^3
Bond shear (tangential) stiffness, k_s^b	6×10^8	N/m^3
Coefficient of bond radius, c_r	1.0	-

In our DEM simulations, the initial particle packing is generated with a "rainfall" method, as shown in Figure 5.8 (visualized with OVITO Stukowski (2009)). First, packs of particles were inserted periodically from a region above the container and allowed to deposit in the container due to gravity. The insertion region is also a cylindrical volume with a radius of 150 mm and vertical extension from $z = 100$ to 150 mm. The particle insertion was stopped when the height of the bulk sample reached well above 100 mm. Then the system was allowed to relax until the mean velocity of the particles became sufficiently small. It is important to note that a large friction coefficient of $\mu = 1.0$ was used until this point, in order to enhance the packing porosity. The simulation was then restarted with $\mu = 0.5$ and allowed to re-equilibrate with time reset from $t = 0$. Due to the sudden reduction of friction, the bulk height of the sample decreased noticeably. Such change also caused a sudden increase of the system kinetic energy, as shown near $t = 0.02$ s in Figure 5.9a. Finally, the particles with positions above $z = 100$ mm were removed, which caused another slight increase in the system kinetic energy as seen near $t = 0.32$ s in Figure 5.9a. The system was

again allowed to relax until the mean velocity of the particles had sufficiently decreased, as displayed in Figure 5.9b. The sample obtained in the initial packing contained about 61,900 particles (i.e. 1,348,513 based spheres), corresponding to a porosity of about 60%. Note that when $\mu = 0.5$ was used throughout the whole initial packing process, a lower porosity of 56.4% was obtained. Such comparison suggests that a large μ can be used as a porosity enhancer during particle insertion for creating a loose initial packing. In fact, the bulk porosity measured in physical samples is usually very high, and how to create a high initial packing porosity in DEM simulations is not trivial.
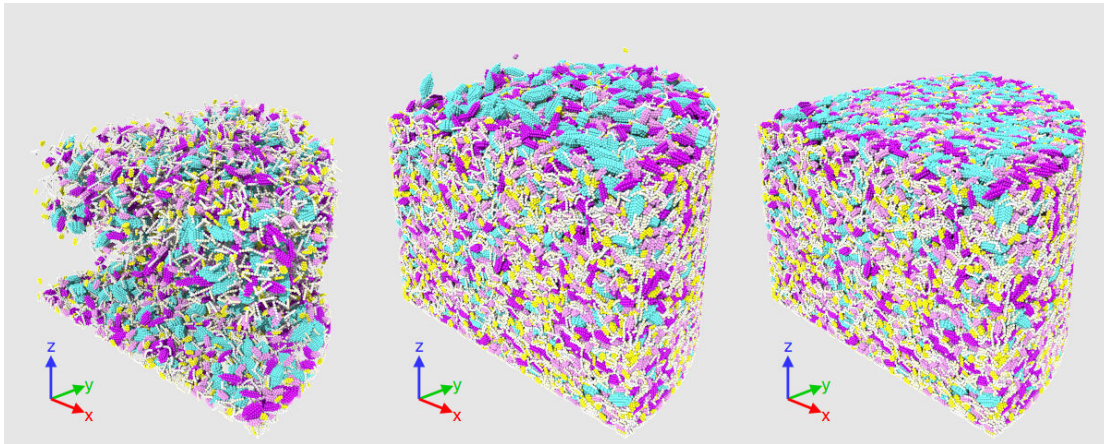
Figure 5.8: Initial particle packing with a "rainfall" method. from left to right: insertion by "rainfall", insertion completed; extra particles removed.

In order to enable quick calibration of the material and contact property parameters, we created a separate simulation setup, denoted as half-size simulation, with the radius and height of bulk sample reduced by half (see Figure 5.10), while using the same six types of DEM particles with the same size and mass ratios. The half-size simulation contained about 8,080 particles after initial packing, with the number of the base spheres (164,149) being roughly one-eighth of that in the full-size simulationn. A comparison of simulation problem sizes between the full-size and half-size simulations is provided in Table 5.3. The half-size simulation allows us to identify a suitable set of parameters with a great reduction of computing time. The parameters identified in half-size simulation were then used in
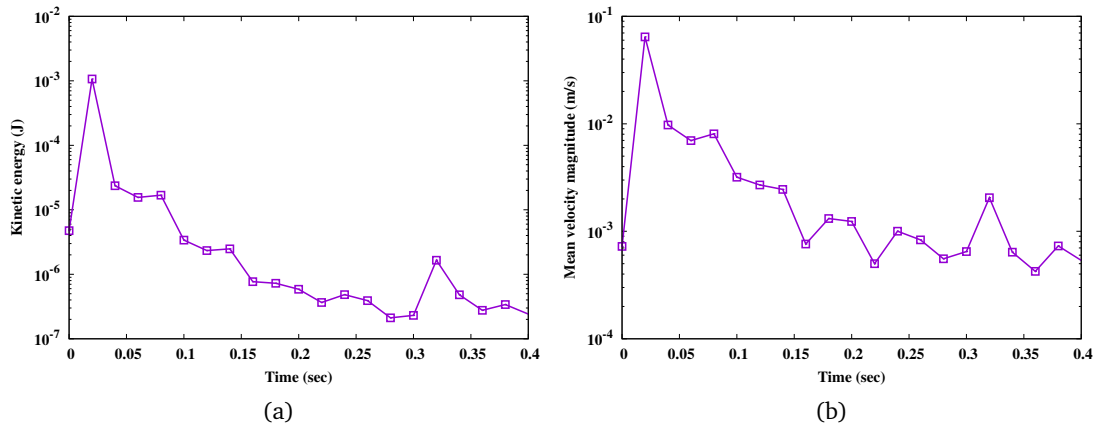
Figure 5.9: Time history of (a) the system kinetic energy and (b) the mean velocity magnitude of base spheres since the reduction of friction coefficient from $\mu = 1.0$ to 0.5, until final equilibrium.

the full-size simulation. By doing so, the domain size effects can be checked as well. The simulation setup described above was selected to mimic the physical experiments in which the pinewood particles were slowly poured into a cylindrical vessel with a diameter of 177.8 mm. The particles were poured to a depth of 100 - 120 mm, and were then evenly distributed using a flat scraper held at approximately 75° and moved forward to avoid causing compressive stress during the top surface smoothing process.
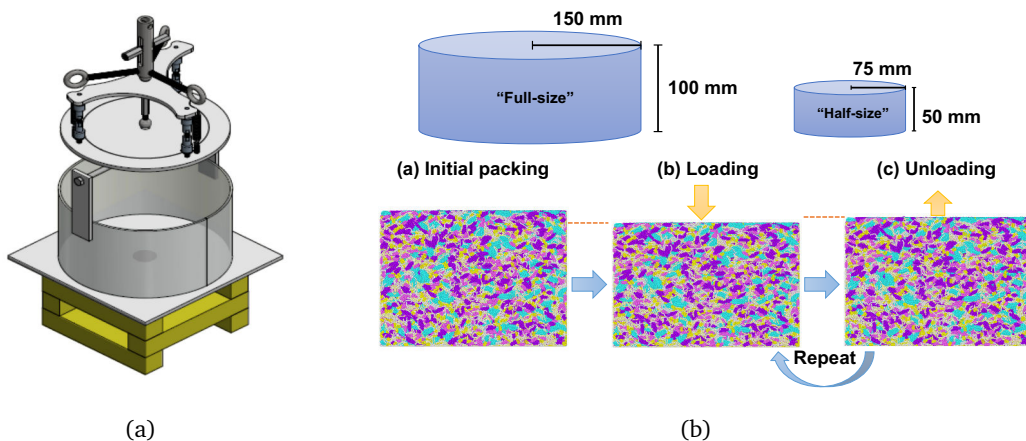
Figure 5.10: Illustration of the cyclic compression test setup for DEM simulations: (a) laboratory compression tester, and (b) numerical DEM setup.

Table 5.3: Simulation problem sizes.

Metrics	Full-size simulation	Half-size simulation
Diameter of base spheres	1 mm	1 mm
Radius of container	150 mm	75 mm
Bulk height of sample	100 mm	50 mm
Number of particles	about $61,900$	about $8,080$
Number of base spheres	$1,348,513$	$164,149$
Initial packing porosity	60%	61%

5.4.2 Cyclic stress loading and unloading

The initial packing is followed by an axial compression test, as illustrated in Figure 5.10. The simulations resembled the main procedures of the laboratory experiment. In the test, six loading & unloading cycles were sequentially operated on the same sample, with peak compressive stresses of 0.5, 1, 2, 3, 4 and 10 kPa, respectively. For example, the 0.5 kPa stress loading was conducted on the sample from the initial packing, and the 1 kPa stress loading was conducted on the same sample after the 0.5 kPa stress was unloaded. At the beginning of the simulation test, a quarter circular surface mesh made of triangular elements was added inside the container with a position slightly above the sample. This mesh represents a lid to be pushed downward against the sample to provide the compressive stress. A servo-control mechanism was applied to the lid mesh with a user-specified target stress (e.g. 0.5, 1.0 ... 10 kPa) and user-specified maximum velocity (e.g. 0.1 m/s). The compressive stress being monitored was calculated as an integration of sphere-to-mesh contact forces divided by the area of the quarter lid. During loading & unloading, an automation algorithm was used in the servo-control such that 1) when no particles were detected near the mesh, it moved at the specified maximum velocity; and 2) when particles were detected near the mesh, the lid velocity was reduced to prevent the lid from moving too much within one time step and passing over the neighboring particles. When the calculated stress approached close to the target value, the velocity of the lid was further reduced to allow the stress to reach the target value smoothly. The transient external force and bulk height data were recorded and converted to stress-strain relation for calculating bulk moduli of elasticity.

5.5 Simulation results

In this section, we report DEM simulation results for the axial compression test with pinewood particles. The simulations were performed with LIGGGHTS Kloss et al. (2012) (version 4.0.0) on a computing node (36 Intel Xeon E5-2695 v4 CPU cores, 128 GB of RAM, SUSE Linux).

The reference physical experiments were performed using an Instron automated load frame (Norwood, MA, USA; model 5967), as shown in Figure 5.10. The maximum speed of the lid varied during the tests but was always regulated to ensure that the instantaneous stress approached the target value smoothly. The target stress values were maintained for 1 minute before being relaxed. Four tests were conducted in order to account for possible discrepancies in sample splitting and preparation, although results from only two representative tests are shown here. In DEM simulations of the test, a servo-control mechanism with a higher loading speed (see Section 5.4.2) is adopted to achieve a balance between computational expenses and quasi-static state of simulation. It took 360 hours to simulate a physical time span of 20 seconds (10 million time steps), with a timestep size of $\Delta t = 2$ microsecond (ms) being used. Despite the huge computational cost, simulations are found very helpful for experimentation, as they can unveil more inner details of the test system that the laboratory experiment is not able to measure. For example, Figure 5.11 shows the simulated porosity contours of initial packing as well as two typical stress loading states on the lateral cross-section plane at $z = 50$ mm and radial cross-section plane at the 45° angle for $z = 0$ - 80 mm. The porosity distribution in the bulk exhibits strong heterogeneity due to the irregular-shape particles and distributions, but the mean porosity are still around 60% in these planes of initial packing. The simulation results are compared with the experimental data obtained from the physical tests for validation and calibration. The primary metrics that will be discussed as follows include 1) the bulk stress-strain relations and 2) the bulk density.
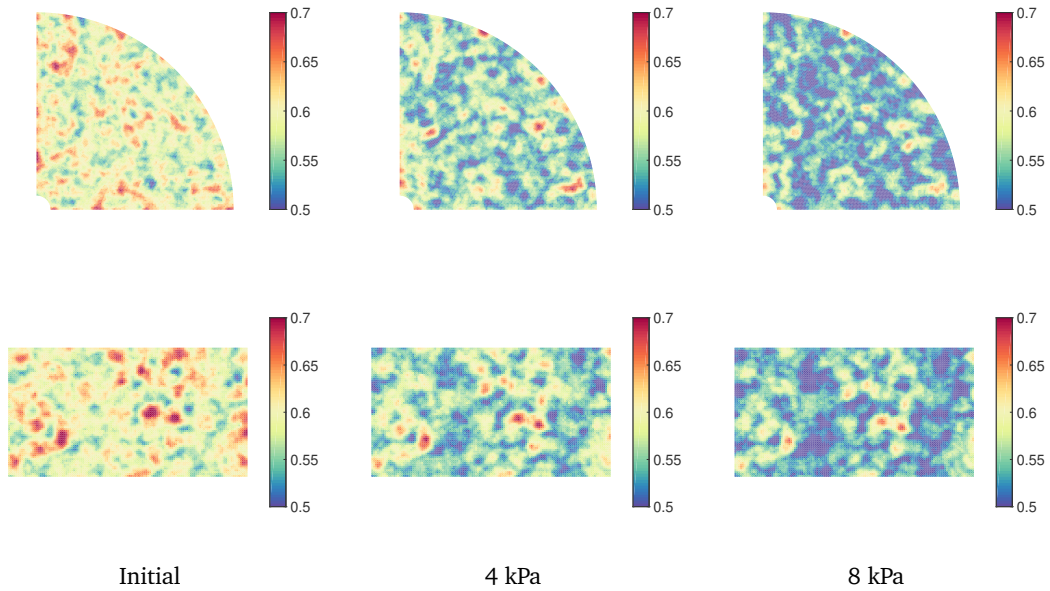
Figure 5.11: Porosity contours on horizontal cross-section plane at $z = 50$ mm (top) and vertical cross-section plane at 45° angle (bottom).

5.5.1 Bulk stress-strain relations

When bulk pinewood chip particles are subject to a sequence of loading & unloading cycles with sequentially increased peak loading stresses, the evolution of the bulk mechanical behavior can be characterized in two phases: Phase 1, bulk plasticity dominant phase in the beginning lower loading & unloading cycles; and Phase 2, bulk elasticity dominant phase in the subsequent higher loading & unloading cycles. During Phase 1 when peak loading stresses are relatively low, the internal structural evolution of the bulk is likely dominated by the irreversible reduction of porosity due to pore collapse and particle reassembling, and as a consequence, the bulk is not expected to fully restore its volume (or height in the present setup) after each unloading. Phase 2 arrives when the peak loading stresses become sufficiently large in the ensuing cycles (but not yet near the threshold to cause particle breakage): the mechanical behavior of the bulk is expected to be more elastic, as the room for the residual porosity to further diminish is much smaller. In the experiments, no breakage

of pinewood chips is detected in the samples, which warrants the use of loading stress up to 10 kPa.

Figure 5.12 presents a comparison between the simulations and experiments on the full stress-strain histories of the six loading & unloading cycles. The compressive bulk strain ε is calculated by $\varepsilon = (L_0 - L_*)/L_0$, where L_0 is the height of the initial pack (i.e. $L_0 = 100$ mm in the full-size simulation and 50 mm in the half-size simulation), and L_* the transient height of the pack. For clarity, we also plotted each of the cycles individually in Figure 5.13, which shows that both the simulations and experiments captured bulk plastic deformation to certain extent in those cycles (e.g. $\Delta\varepsilon = 1\%$ to 3%). A number of main observations are discussed as follows. First, the two experimental curves exhibit a clear difference from the second cycle to the last, in part due to the inherent difference between the two samples. As shown in Figure 5.13, the first sample exhibited more plastic deformation than the second one by up to 1.1% throughout the test. Nevertheless, the shapes of the two experimental data curves look similar near all the peak stresses, which indicate consistent bulk mechanical properties between the two samples under compressive stress. Another interesting phenomenon is when the peak stresses were reached and then maintained, the bulk strain continued to increase slightly. For example, as can be seen in Figure 5.13f, the two samples underwent a continued bulk deformation by $\Delta\varepsilon = 0.5\%$ when the peak loading stress stayed at 10 kPa. Such creeping phenomenon was not observed in the simulations with the present DEM model, which does not incorporate any rate-dependent contact models.

Regarding the DEM simulation results, the domain size effect is observed between the two simulation curves obtained with the full-size simulation and half-size simulation, as shown in Figure 5.12a. A closer comparison in Figure 5.13a and Figure 5.13b suggests that, though the two simulations have similar initial packing porosity, i.e. 60% versus 61%, more porosity (in terms of percentage) had diminished in the half-size simulation over the first two cycles, which led to about 1% more bulk plastic deformation. Nevertheless, as seen in Figure 5.13c, the two simulations of different sizes behaved quite similarly since the third cycle, despite a pre-existing difference in bulk plastic deformation by 1%. The
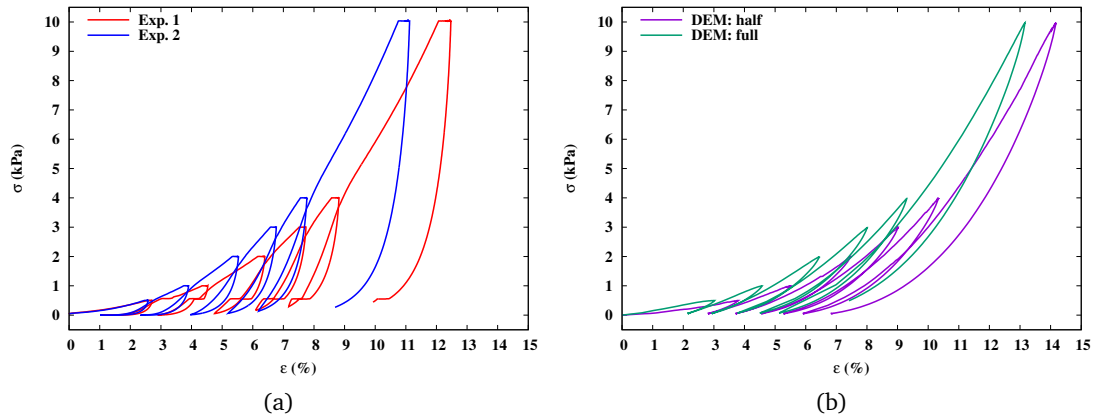
Figure 5.12: Comparison of stress-strain curves for the compression test between (a) experiments and (b) simulations.

stress-strain curves obtained with the full-size simulation have a reasonable agreement with their experimental counterparts over the first three cycles, where the simulated curves are bounded by the two experimental data curves (see Figure 5.13a - Figure 5.13c). In addition, we sampled the stress and strain data in the 89 - 99% range of each peak stress (e.g. 3.56 - 3.96 kPa during the 4 kPa loading) for calculating the transient bulk moduli of elasticity, and compared the results between the simulations and experiments in Figure 5.14. The values associated to the full-size simulation are consistently lower than their experimental counterparts near each peak stress, but yet bounded in a 20% deviation of the experimental data. The bulk moduli of elasticity in the simulations can be increased with a higher k_n^b value to better match the experimental data. However, a major discrepancy between the simulations and experiments lies in the unloading regions, where the experimental unloading curves are significantly steeper than their simulation counterparts. As a result, the physical samples displayed 1% more bulk plastic deformation than the simulated samples at the end of the test, as shown in Figure 5.13f. This contrast suggests that even after the six loadings already conducted, it is highly possible the experimental samples may still contain an abundance of pore spaces that could shrink during subsequent loadings. However, the simulated pinewood particles, which were dominated by bulk elasticity other than plasticity over the last three cycles, exhibited much less plasticity during the unloading processes

107

(a) 0.5 kPa

(b) 1 kPa

(c) 2 kPa

(d) 3 kPa

(e) 4 kPa

(f) 10 kPa
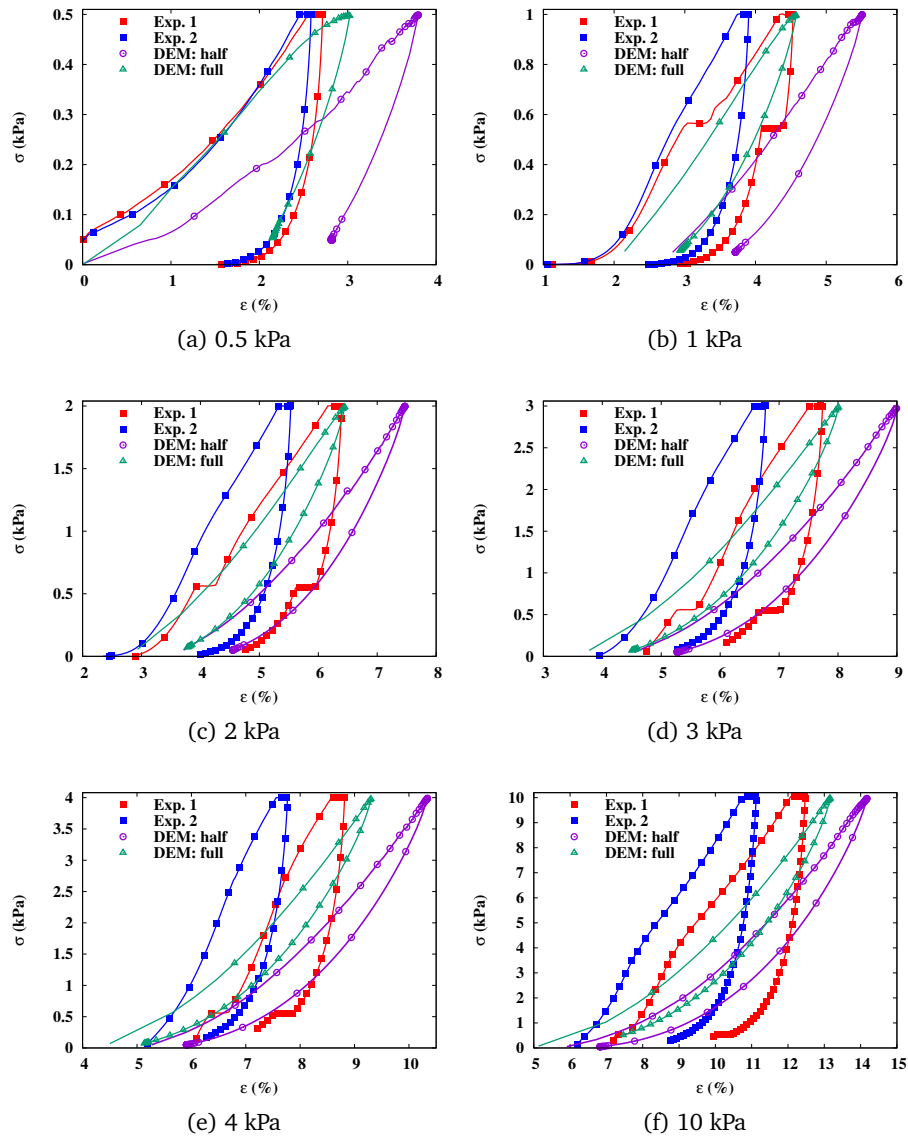
Figure 5.13: Comparison of experiment and simulations on the stress-strain histories in individual cycles.

as well as smaller bulk plastic deformation (i.e. $\Delta\varepsilon \leq 1\%$ as shown in Figure 5.13d - Figure 5.13f). The small strain recovery during relaxation after the applied stress is removed, even at high stress levels, suggests that plasticity is consistently dominant over elasticity across the entire range of applied stress. The observed changes in the effective Young's modulus and Poisson's ratio (i.e. the slope of the stress-strain curves during relaxation) is likely due to changes in effective particle-particle friction coefficients. This observation indicates that the friction coefficients and other parameters should be considered functions of the strain or void ratio. This behavior is not unexpected because the impact of surface and internal moisture are expected to be strong functions of contact pressure and area, which are dependent upon strain and void ratio. Above all, these findings call for further investigation for enhanced DEM models to account for the large bulk plastic strain in pinewood particles after unloading.
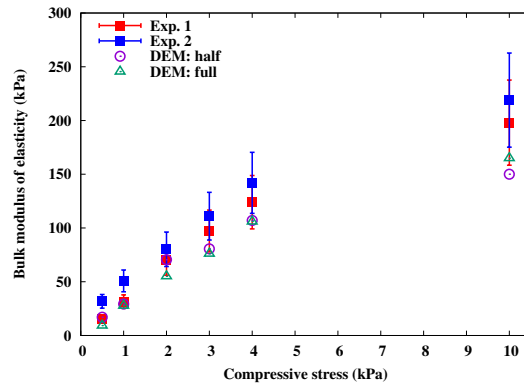
Figure 5.14: Comparison between experiment and simulations on the bulk moduli of elasticity near the peak loading stresses. The error bars represent a 20% deviation from the corresponding data.

5.5.2 Bulk density

Measured at initial packing, the bulk densities of the two physical pinewood chip samples read 169 and 159 kg/m^3. The porosities of the physical samples were also measured and used as references for porosity in the DEM simulations. To keep generality in our discussion, we first express the bulk density of particulate materials in the following general

form,

$$\rho_{\text{bulk}} = \rho_{\text{grain}}\phi_{\text{grain}} = \rho_{\text{grain}}(1 - \phi_{\text{void}}),$$

where ρ_{grain} denotes the grain density, ϕ_{grain} the grain volume fraction, and ϕ_{void} the bulk porosity, respectively. In bonded-sphere DEM simulations, the ϕ_{void} accounts for the void space between the base spheres only, and can be calculated as

$$\phi_{\text{void}} = 1 - \frac{N_{\text{spheres}}\frac{4}{3}\pi r_{\text{sphere}}^3}{\frac{1}{4}\pi r_{\text{cylinder}}^2 h_{\text{bulk}}}$$

in a quarter cylindrical container, where N_{spheres} is the number of base spheres, r_{cylinder} the container radius, h_{bulk} the bulk height, and r_{sphere} the sphere radius. In the simulations, ϕ_{void} depends on a number of physical constraints such as the particle shapes, particle size distributions and inter-particle friction coefficient. The bound of ϕ_{void} can be roughly estimated if those constraints are specified. For example, with random packing, mono-sized rigid spheres have a statistical lower limit of ϕ_{void} as 36.6%. Recall that our simulated bulk samples have a ϕ_{void} of 60% from initial packing. In contrast, the ϕ_{void} in the physical pinewood particle samples could be higher than the simulations, as the porosity may include not only the macro void between the pinewood particles, but also the micro pore space on the particle surface and inside the particle internal structures.

In order to obtain the ϕ_{void} in the physical samples, we first measured ρ_{grain} with a gas pycnometer, as ϕ_{void} can be calculated from $\phi_{\text{void}} = 1 - \rho_{\text{bulk}}/\rho_{\text{grain}}$. The ρ_{grain} measured is equal to 1398 ± 23 kg/m^3, an average of 5 representative splits of the material, with each split measured three times. This value appears much higher than the density of natural pinewood blocks, which range from 400 to 460 kg/m^3. Nevertheless, ρ_{grain} values between 1400 and 1600 kg/m^3 are often reported for processed wood chips with this technique Redding et al. (2005); Hehar et al. (2014); Olatunde et al. (2016). Based on the measured ρ_{grain}, the calculated ϕ_{void} is equal to 88% and 89% for the physical samples at initial packing, being much higher than their DEM counterpart. Two possible factors are considered to have

contributed to the high ϕ_{void} values (or equivalently ρ_{grain}) in experiments. For the first, the irregular surface structures of realistic pinewood particles at both the macro and micro scales are likely to have created more inter-particle voids than it could be numerically possible in DEM simulations, as the surface of base spheres in our DEM models is assumed smooth. For the second, as mentioned earlier, it is likely that the pore space in our laboratory samples also included internal macro and micro pore structures of the pinewood particles as a result of pressurized open-up and infiltration by the probe gas (e.g. helium). Taking these factors into account, it is legitimate to interpret the relatively low ϕ_{void} in the DEM simulations as the void space external to the particles, and reasonable to use a ρ_{grain} value closer to the density of natural pinewood block for calculating ρ_{bulk} in the DEM simulations.
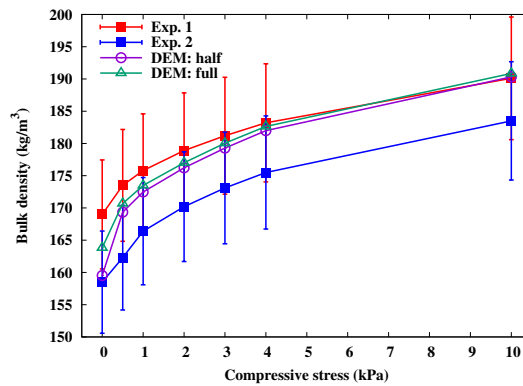
Figure 5.15: Comparison between experiment and simulations on the bulk density under the six peak loading stresses. The error bars represent a 10% deviation from the corresponding data.

Figure 5.15 displays a comparison of the simulation and experimental results on the bulk density under the six peak compressive stresses in the test. A number of important observations are as follows. First, the two experimental data sets exhibit clear difference in the magnitude of the measured densities (which is common for particulate wood materials in part due to the unavoidable variance between different samples), but much similarity in their increment when the compressive stresses reached higher. For the DEM simulations, the calibrated ρ_{grain} for fitting the experimental data is equal to 410 kg/m^3, which is within the density range for natural pinewood block in our case (400 - 460 kg/m^3). We have also

found that within this range ϕ_{void} is relatively insensitive to the choice of ρ_{grain}. With the ρ_{grain} value chosen for our model, the curves obtained in both the full-size and half-size simulations are found bounded by the experimental data in a narrow error range of $\pm 10\%$, as shown in Figure 5.15, well satisfying our expectation of 80% fidelity for DEM simulations. Moreover, the two simulation curves appear to well agree with each other under all the six peak loading stresses. This indicates that ρ_{bulk} is relatively insensitive to the bulk size in our DEM simulations, as long as the bulk is sufficiently large. Lastly, it is worth noting that the ϕ_{void} is 1% higher in the half-size simulation than that in the full-size simulation at initial packing, which is implied by a smaller initial ρ_{bulk} in Figure 5.15. We anticipate this effect is due to the greater impact of wall boundaries in the half-size simulation. When the 0.5 kPa loading was applied, the additional porosity in the half-size simulation diminished quickly and reached the values close to the full-size simulation. This corresponds to the greater bulk plastic strain in the half-size simulation as observed in Figure 5.13a.

5.5.3 Further model calibration

Recall in Section 5.5.1, the bulk moduli of elasticity near the peak loadings obtained in the simulations are found overall lower than the experiments, as shown in Figure 5.14. As suggested earlier, a straightforward way to enlarge the bulk moduli of elasticity in the simulations is to make individual multi-sphere particles less deformable by increasing the bond normal stiffness k_n^b. In addition, we speculate that an increase in k_n^b may also have effect on the bulk mechanical behavior during the stress unloading periods, and subsequently improve our DEM model to better predict the mechanical behavior of bulk pinewood chips. In order to verify our assumption, we designed two additional simulation tests with the half-size simulation setup, and specified an k_n^b value equal to 10 GN/m^3 in the first test and 100 GN/m^3 in the second test. These two tests were started from the completed initial packing, but underwent only one stress loading & unloading cycle with a peak stress of 10 kPa, in order to avoid excessive computing time. We did not conduct the full six loading & unloading cycles here, since even a half-size simulation for completing the full six cycles with

112

$k_n^b = 10$ GN/m^3 and $\Delta t = 2$ ms requires about 50 hours on our 36-core compute node. To make the case even more demanding, the second test which uses $k_n^b = 100$ GN/m^3 requires a Δt as small as 1 ms to ensure numerical stability.
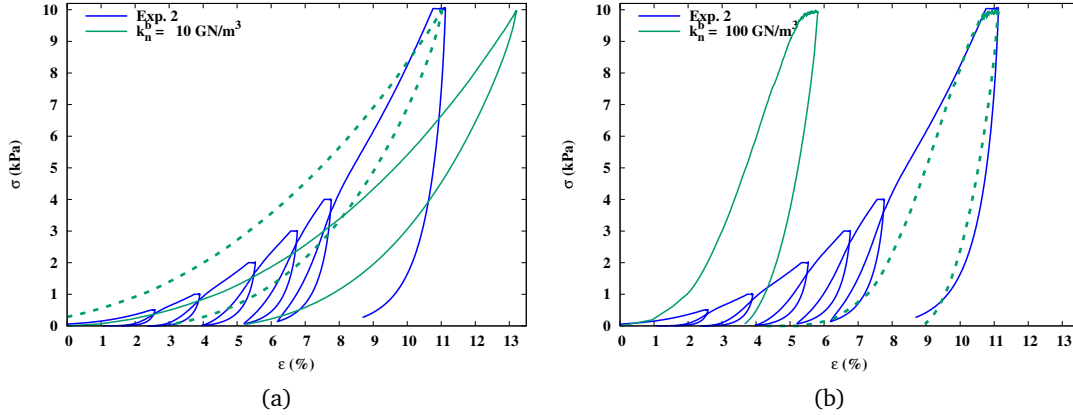
Figure 5.16: Stress-strain histories obtained by the two single loading & unloading simulations with (a) $k_n^b = 10$ GN/m^3 and (b) $k_n^b = 100$ GN/m^3. The green solid lines are the actual simulation curves; the green dashed lines are a result of horizontal shift to compare the slopes near the 10 kPa peak stress with the cyclic experimental test.

The stress-strain relations obtained by the simulation tests are shown in Figure 5.16 as green solid curves, and are compared with the experimental curves of the full six cycles. The green solid curve in Figure 5.16b appears much more stiff than that in Figure 5.16a, confirming a much stiffer bulk elasticity of the particles with a 10 times increase of k_n^b. Meanwhile, the bulk particles in the second test have experienced much less bulk plastic deformation than the first during stress loading, as they are harder and would not deform much to allow the porosity to diminish. During stress unloading, the bulk particles in the second test lost a compressive strain by only 1.5% – much less than the 7% loss of compressive strain in the first test. In order to better compare the two simulation curves with the last cycle in the experimental curve, we shifted them horizontally to allow their peak stress locations to match the experiments, and represented the shifted curves with the green dashed lines. The dashed curve in Figure 5.16b indicates a significantly improved simulation result that has a much better agreement with the experimental curve than in Figure 5.16a, especially for the

stress unloading period. However, as we mentioned earlier, the use of an enlarged k_n^b can not produce large plastic strains during the loading periods (especially at low loading pressures). An enlarged k_n^b also implies a smaller Δt required for numerical stability, which would then make the DEM simulations ever more expensive for these tests. Therefore, a quest for more realistic elasto-plastic contact models and more cost-effective model calibration methods is anticipated, and deserves more effort in the future.

5.6 Summary

A bonded-sphere DEM model based simulation approach has been presented for studying the mechanical behavior of bulk flexible, deformable pinewood chips. Clustered spheres that can bend and twist via elastic bonds have been used to model irregular particle shapes and constituent mass distribution sampled from real bulk pinewood chips. With a careful model calibration, a cyclic stress loading test simulation, which is designed with the size similar to a corresponding laboratory experiment, has been carried out to predict the bulk mechanical behavior of pinewood chips. The bulk densities and compressive moduli of elasticity obtained in the simulations have reached good agreement with the experimental results. However, it has been found challenging for the present DEM model to accurately predict the overall stress-strain behavior of bulk pinewood chips, especially the large sustained plastic deformation during the unloadings. Additional simulation tests have shown that adjustment in certain contact parameters (e.g. bond normal stiffness) could help improve the accuracy of the simulations in terms of some mechanical properties, but meantime would induce additional challenges, such as doubled or even tripled computing time. An elasto-plastic model based on the works of Luding (2005a,b) will be considered for further enhancing the fidelity of the DEM simulations in the future. Another potential opportunity is to allow values of model parameters, such as particle-particle friction, to depend upon strain or void ratio. Compared with prior DEM works that simulated bulk wood chip flow with simple rigid spheres, rods or blocks, the present work has demonstrated the

importance for a DEM model to account for the particle irregular shapes and deformability, in order to better predict the mechanical behavior of bulk wood chips. It is critical to understand that DEM models must reproduce the mechanical behavior of real particulate biomass materials (which are usually relatively soft), in order for the resulting simulations to be of value to provide key diagnosis for helping improve the design of biomass feeding and handling equipment. Above all, a better understanding of the mechanical behavior of the challenging biomass materials will likely require close coupling between instrumented laboratory and pilot scale tests and multi-scale modeling (Westover et al., 2018).

Chapter 6

Discrete element modeling the granular hopper flow of deformable-irregular particles

For granular materials that are comprised of irregular-shape flexible particles such as woodchips, corn stover or switchgrass, the particle deformability is exhibiting significant impact on their bulk flow behavior. To investigate the particle deformability effects, this work presents a bonded-sphere discrete element modeling (DEM) approach to numerically simulate the flow behavior of deformable-irregular particles. In this approach, a cluster of bonded spheres is employed to model an irregular particle and provide it with the ability to capture particle-wise deformation (e.g., compression, deflection or distortion). With an application of granular flow in a wedge-shaped hopper, the flow characteristics of deformable-irregular particles are studied. Same simulations while with spherical particles and rigid-irregular particles are also conducted as a comparison. As observed from the simulations, the rigid-irregular particles exhibit clogging issues while deformable-irregular

A similar form of this chapter has been submitted at the time of writing: Z. Lai, Y. Xia, H. Huang, T. Westover, and Q. Chen. Discrete element modeling the granular hopper flow of deformable-irregular particles.

particles do not as to the same orifice size, which indicates that particle deformation will reduce the critical bridging width. The quantitative analysis about particle stress, wall stress and discharge rate shows good agreements with the Walker's theory and extended Beverloo's formula, respectively. Further simulations with various bond stiffness and shape combinations are also devised and analyzed for the sake of gaining more insights into the effects of particle size, shape and deformability on granular hopper flow.

6.1   Introduction

Hopper is a type of equipment for material charging and discharging, and is commonly used in areas such as civil engineering, food and pharmacy industry, and biorefinery. Although most hoppers are simple in geometric configurations, the behavior of granular hopper flow can be complicated under the influence of various factors related to hopper geometries and flow media properties. The design of hopper flow is a non-trivial task, as inappropriate designs could result in poor operation performance and even equipment or functional failures (e.g., clogging and ratholing) (Horabik and Molenda, 2014). Therefore, great efforts have been and continuously will be made to better understand the granular hopper flow in regard to different hopper designs or flow mediums, and from both experimental and numerical perspectives.

Due to the discrete nature of granular materials, the particle-based discrete element method (DEM) (Cundall and Strack, 1979) has been emerged as the most prevalent numerical tool for modeling granular hopper flow and helping understand the bulk flow behavior from the micromechanics of granular materials. As a popular research topic for nearly two decades, the DEM-based studies on granular hopper flow can be generally categorized into three branches. The first branch focuses on the characterization of the intrinsic characteristics of granular hopper flow, such as the stresses of flow media or hopper wall (Masson and Martinez, 2000; Goda and Ebert, 2005), the flow pattern (e.g., mass flow vs. funnel flow) (Ketterhagen et al., 2009; Zhang et al., 2018b), the flow dynamics or fluctuations (Zhu

et al., 2006; Mollon and Zhao, 2013a; Kobyłka et al., 2017), and the segregation behavior (Ketterhagen et al., 2008; Yu and Saxén, 2014). The second branch puts emphasis on the effects of hopper aspect impact factors on the flow behavior, such as the hopper shape effects (Balevičius et al., 2011), or the orifice shape effects (Wan et al., 2018). The last branch dedicates to a more realistic modeling (e.g., more realistic sizes and shapes) of the particles, as well as the effects of particle-scale material properties on the flow behavior (Masson and Martinez, 2000; Cleary and Sawley, 2002; Balevičius et al., 2008; González-Montellano et al., 2011; Höhner et al., 2012; Liu et al., 2014a; Xu et al., 2015; Zhao et al., 2018b). For example, to gain insights into the sensitivity of granular hopper flow to the microscopic contact parameters, parametric studies on the contact stiffness (Masson and Martinez, 2000), particle-particle contact friction (Masson and Martinez, 2000; Balevičius et al., 2008), particle-wall contact friction (Yu and Saxén, 2011) were conducted. For incorporating more realistic particles in DEM, super-quadrics (Cleary and Sawley, 2002), clumps of overlapping spheres (González-Montellano et al., 2011; Höhner et al., 2012), or ellipsoids (Liu et al., 2014a) have been employed and the effects of particle shapes on flow behavior have been studied. It should be noted, however, that by using either spheres, super-quadrics, clumps or ellipsoids to model particles, these DEM simulations considered particles as rigid bodies without any particle-wise deformation (e.g., compression, deflection or distortion). Thus, although the granular hopper flow in different scenarios has been extensively studied via DEM, the observations and conclusions from these studies suit a type of "rigid" particles, and may not be applicable to flexible, deformable particles.

The granular hopper flow of flexible, deformable particles can be widely seen in biomass logistics and biorefinery process (Westover et al., 2015, 2018; Ilic et al., 2018), while the effects of particle deformability on their flow behavior have been a relatively unexplored area. As to the granular materials consisting of stiff particles, such as sands, grains or tablets, the constituent particles exhibit negligible particle-wise deformation in regular scenarios of applications. For this type of materials, the particle size and shape are well-known to be the two most salient factors affecting their flowability (Cleary and Sawley, 2002; Lai and

Chen, 2017). However, for flexible granular materials, such as woodchips, corn stover and switchgrass, their constituent particles may present great deformability (e.g., compression, deflection or distortion) even with a low external load (Mani et al., 2003; Wu et al., 2011; Stasiak et al., 2015). In addition to the particle size and shape, the particle deformability is another important factor that should not be ignored when studying the flowability of this type of materials. To approach a reliable modeling and prediction of the flow behavior of granular materials consisting of flexible particles, it is necessary to incorporate not only the particle size and shape, but also the particle deformability into the DEM model.

The primary goal of this work is to come up with a DEM approach to model granular hopper flow with the capability of embodying different particle sizes and irregular shapes, and more importantly, capturing particle deformability. For this purpose, the bonded-sphere model is employed to represent deformable-irregular particles in DEM. The loblolly pine woodchips are taken as a reference example for conceptualizing irregular shape templates and calibrating the contact parameters used in the DEM model. As a major contribution, the flow characteristics of deformable-irregular particles in a wedge-shaped hopper are studied with comparisons from spherical particles and rigid-particles. Particularly, the packing porosity, flow pattern, particle and wall stresses, and discharge profiles are analyzed. The particle and wall stresses are also compared with the Walker's theory and the discharge rate are benchmarked against the extended Beverloo's formula, both of which exhibit good agreements, respectively. To further explore the effects of particle shape and deformability, parametric studies on the particle bond stiffness and shape combinations are performed and analyzed as well. Although rather a simple hopper flow system (i.e., wedge-shaped and only two shape templates) is being considered, the present study achieves to model and capture the effects of particle deformability as a first step. The differences in the flow behaviors between deformable-irregular particles and rigid-irregular particles demonstrate the importance of taking into account the effects of particle deformability. The methodology and workflow presented in this study can be conveniently extended to model more complex-shaped hoppers with particles of wider variations in size, shape and deformability.

6.2 Bonded-sphere DEM model

In this section, we will present the formulation of bonded-sphere model for the representation of deformable-irregular particles in DEM. The DEM basics and the adopted inter-particle contact model will also be briefly described for the sake of completeness.

6.2.1 Bonded-sphere model for deformable particles

In recent years, DEM models accounting for deformable-irregular particles have been developed and applied to investigate the packing (Langston et al., 2015), compression (Leblicq et al., 2016b,a) and shear flows (Guo et al., 2015) of flexible fiber, or the separation of grain-straw mixture (Lenaerts et al., 2014). The prevalent approach of representing deformable-irregular particles in DEM is to employ the bonded-particle model, which is initially devised by Potyondy and Cundall (2004) to model fracture initiation and evolution across mineral grains in rock. In bonded-particle model, a deformable-irregular particle is represented by a cluster of base elements, which can be spheres (Guo et al., 2015), cylinders (Potyondy and Cundall, 2004; Lenaerts et al., 2014) or sphero-cylinders (Langston et al., 2015). The basic elements are connected by bonds (or joints), on which contact models are imposed to transit forces and moments. In this work, we will simply use spheres as the base elements to form deformable-irregular particles. To distinguish the usages of "particle" in different phrases, we will use "bonded-sphere model" when referring to "bonded-particle model" hereafter.

Figure 6.1 shows the sketch of bonded-sphere model and the rheological components of bond behavior. The spheres within a same particle are connected with bonds, which can be regarded as special contacts that can carry forces and moments. The bonds connect the spheres as a cluster, and also allow them to have relative displacements when the cluster is subject to external loads. Particle deformation is then reproduced from the overall effects of relative displacements of the spheres within the cluster (i.e., the particle). To describe the bond behavior (i.e, the interaction between two bonded spheres), the linear parallel bond

model (Potyondy and Cundall, 2004) is adopted. It is simple, but provides restrictions to both the relatively translational and rotational displacements of the bonded two spheres. There are also other more complicated bond models, such as rolling resistance model (Jiang et al., 2014, 2015a,b), elasto-plastic model (Guo et al., 2018) or visco-elasto-plastic constitutive model (Fleissner et al., 2007), to accommodate the modeling demands for specific materials. The simple linear bond model is adopted for simplicity as the focus of this study is on granular hopper flow, while the extension with more complicated bond models is straightforward.
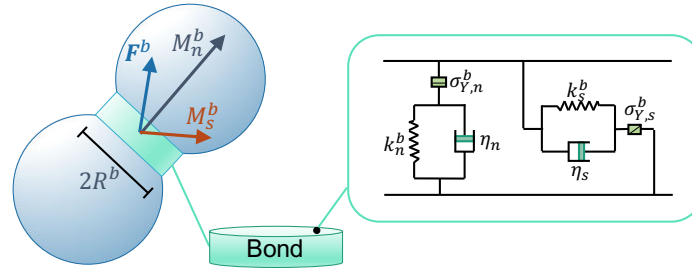
Figure 6.1: Sketch of bonded-sphere model and rheological components of bond behavior.

In linear parallel bond model, the bond between two spheres is assumed to be a cylinder of finite radius and thickness. Each point in the bond is imposed by two linear elastic springs providing normal and shear resistances, respectively. The overall bonding force and moment are the integral of the normal and shear stresses (compression as a positive) at a cross-section of the bond, which be can calculated as (Potyondy and Cundall, 2004)

$$\Delta F_n^b = k_n^b A \Delta \delta_n \tag{6.1}$$

$$\Delta F_s^b = k_s^b A \Delta \delta_s \tag{6.2}$$

$$\Delta M_n^b = k_s^b J \Delta \theta_n \tag{6.3}$$

$$\Delta M_s^b = k_n^b I \Delta \theta_s \tag{6.4}$$

where F_n^b, F_s^b, M_n^b and M_s^b are the bond normal force and shear force, twisting moment and swinging moment, respectively; δ_n, δ_s, θ_n and θ_s are the relative normal displacement, shear displacement, twisting rotation and swinging rotation between the two bonded spheres,

respectively; A, I, and J are the area, moment of inertia and polar moment of inertia of the bond (i.e., the bond cross-section with radius R^b), respectively; and Δ indicates the increment of each variable at each time step.

The bonded-sphere model is also capable of modeling particle breakage behavior. For a common type of bond breakage criterion, it is assumed that a bond would break if the normal or shear stress at any point exceeds the corresponding strength. For linear parallel bond model, both the normal force and swinging moment contribute to the normal stress, and both the shear force and twisting moment contribute to the shear stress. As a consequence, the bond breakage criterion can be given as

$$\sigma_{\max}^b = \frac{F_n^b}{A} + \frac{M_s^b R^b}{I} < \sigma_{Y,n}^b \tag{6.5}$$

$$\tau_{\max}^b = \frac{F_s^b}{A} + \frac{M_n^b R^b}{J} < \sigma_{Y,s}^b \tag{6.6}$$

where $\sigma_{Y,n}^b$ and $\sigma_{Y,s}^b$ are the normal and shear strength, respectively.

6.2.2   DEM basics and contact models

DEM directly tracks the motion (e.g., position, velocity and acceleration) of all particles. Each particle has two types of motion: translational and rotational, which can be described by the Newton-Euler equations of motion. A numerical simulation based on DEM requires cyclic calculations, in which the motion of particles and the interaction between particles are fully resolved. To begin with, the contacts between particles are identified and contact features are evaluated. The contact forces/moments are then calculated based on the selected contact models and corresponding contact features associated with each contact. After that, all the forces/moments subjected by each particle are summed and cast into the Newton-Euler equations to calculate the particle accelerations. Lastly, the velocity and position of each particle are time integrated, where the second-order Velocity Verlet algorithm (Verlet, 1967) is commonly adopted. The details of DEM formulation and cyclic

calculations will not be presented herein, but can be found in (Cundall and Strack, 1979; Chung, 2006; Itasca Consulting Group, Inc, 2014).

A key component of DEM cycles is to calculate the contact forces. This work adopts the bonded-sphere model to represent particles, which brings in two types of contacts: intra-particle contacts (i.e., contact between spheres within the same particle) and inter-particle contacts (i.e., contact between spheres from different particles). For intra-particle contacts, their contact forces are calculated based on the linear parallel bond model described in Section 6.2.1. For inter-particle contacts, this work adopts the Hertz-Mindlin contact model. Hertz-Mindlin contact model is a complete frictional contact model based upon the Hertz theory (Hertz, 1882) for contact normal forces and the Mindlin theory (Mindlin, 1953) for contact tangential forces. It takes account of the stiffness variation due to the change of contact areas during the collision of two elastic spheres. Normally, the Hertz-Mindlin contact model can be characterized by four parameters: Young's modulus E, Poisson's ratio ν, coefficient of restitution e, and the coefficient of friction μ. The detailed formulation of the Hertz-Mindlin contact model is referred to (Mindlin, 1953; Di Renzo and Di Maio, 2005).

6.3   Numerical setup of granular hopper flow

This section elaborates the numerical setup of the granular hopper flow tests from the following aspects. The material of interest (i.e., the loblolly pine woodchips) is first discussed with focuses on the particle shapes and contact parameters. Then, the hopper geometries and testing procedures are described, followed by a description of all the different simulation scenarios considered in this work. The customized version of LIGGGHTS 4.0.0 (Kloss et al., 2012) is adopted as the DEM code for setting up the hopper flow simulations. The method to obtain field properties such as packing porosity and particle stresses from LIGGGHTS outputs is presented to the last.

6.3.1 Material and contact parameters

The materials being referenced in this work are the loblolly pine woodchips, which are commonly used as biomass sources for conversion into biofuel or biochemical in biorefinery. Figure 6.2 shows a sample of loblolly woodchips. It is observed that the woodchip samples mainly consist of fiber-shaped and plate-shaped particles. In the present DEM model, the fiber-shaped and plate-shaped woodchips are generalized into two shape templates: fiber and plate (see Figure 6.2). The fiber template is built from five non-overlapping spheres in one row, and the plate template is built from ten non-overlapping spheres in three rows. The spheres have a radius of 1 mm and are bonded with their neighboring spheres. Though the woodchips samples are exhibiting more complex shapes in reality, this work conceptualize these complex-shape woodchip samples into just two shape templates for simplicity in order to reduce the computational expenses.

Woodchips
(mean size ~3 mm)

DEM: fiber & plate
(sphere size 1 mm)
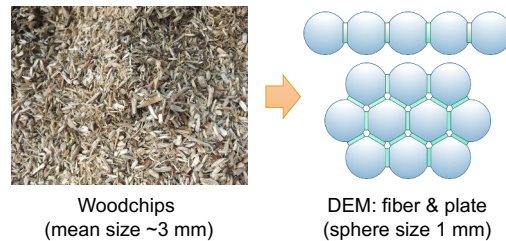
Figure 6.2: Two conceptualized shape templates of woodchips for DEM simulations.

As most of the contact parameters are difficult or impossible to be directly measured, a calibrate process is needed to obtain the contact parameters for the selected woodchip samples. For this purpose, both experimental and numerical compression tests on the woodchip samples are performed, and the stress-strain relation and bulk densities are used as the benchmark metrics for calibration. There are several excellent reviews in the literature discussing the procedures and challenges of calibrating contact parameters for a DEM model (Plassiard et al., 2009; Chehreghani et al., 2017; Coetzee, 2017). Usually, the calibration process is accomplished by performing parametric studies on each contact parameters. To make this work more focused on granular hopper flow, we will not present

the calibration details herein. The final material properties and calibrated contact parameters of the woodchip samples are listed in Table 6.1.

Table 6.1: Material properties and contact parameters of the woodchip samples and hopper wall.

Parameter	Symbol	Value	Unit
Density	ρ_s	430	kg/m^3
Sphere radius	R	0.5	mm
Young's modulus	E	10	MPa
Poisson's ratio	ν	0.3	-
Coefficient of restitution	e	0.1	-
Coefficient of friction	μ	0.5	-
Bond radius	R^b	0.5	mm
Bond normal stiffness	k_n^b	10	GN/m^3
Bond shear stiffness	k_s^b	0.6	GN/m^3
Wall Young's modulus	E_w	1.0	GPa
Wall friction	μ_w	0.5	-
Timestep	Δt	2.0	μs

6.3.2 Hopper flow setup

This work studies a wedge-shaped hopper, with the hopper half-angle α being 30° in particular. A sketch of the hopper is shown in Figure 6.3. In the corresponding DEM simulations, two surface meshes comprised of triangular elements are used to model the hopper walls. To minimize the computational cost, only a thin cross-section of the hopper is considered with a depth of $t_y = 0.01$ m in the y-direction, and a periodic boundary condition is prescribed for the domain boundaries in the y-direction. The initial particle packing is created following a rainfall method (Härtl and Ooi, 2008). In particular, a given number (or mass) of particles are repeatedly inserted in a region above the hopper. The particles are then allowed to fall down into the hopper under the gravity. Once the hopper is filled up to a target height (e.g. 0.18 m in this example problem), the particle insertion is stopped. Then, the particles in the hopper are allowed to sit for a while until the particle packing reaches equilibrium. A criterion of equilibrium is to monitor whether the maximum sphere velocity among all the inserted particles has decreased below a small value, e.g. 5 mm/s as specified in this work. Once the equilibrium is reached, the extra particles that are above the target

height are removed. Lastly, the particle packing is allowed to equilibrate again, in case that the action of particle removal induces disturbance to the packing.

(a)
(b)
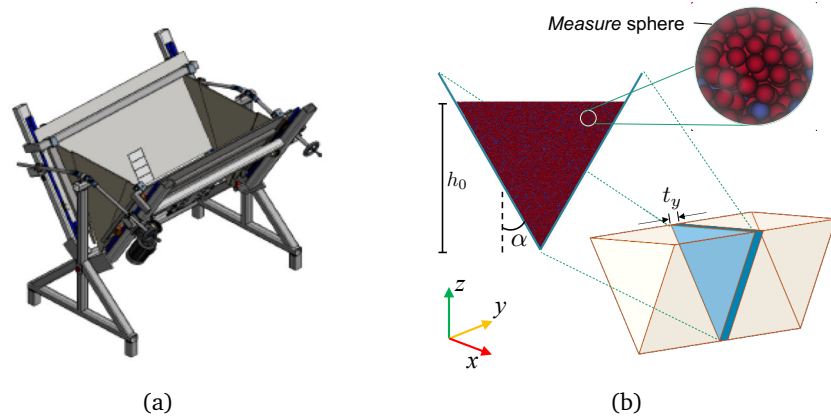
Figure 6.3: Sketch of the wedge-shaped hopper: (a) laboratory hopper flow tester (Westover et al., 2015), and (b) numerical DEM setup. For the example problem considered in this work, the following specifications are used: h_0=0.18 m, α=30°, and t_y=0.01 m.

For the discharging process, we follow a testing procedure similar to the laboratory experiments reported in (Westover et al., 2015), which is designed to measure the critical arching width of biomass materials under self-weight loading or extra surcharge compression by using an adjustable wedge-shaped hopper. To begin with, the hopper walls are gradually raised along their tangential direction at a speed of 0.1 m/min. The size of the hopper orifice is thus gradually enlarged in time. The material critical arching width is then approximated as the minimum orifice size at which particles can continuously flow out of the hopper. As it will be presented later, the particles in most simulation scenarios present a critical arching width smaller than 0.01 m. To facilitate a valid comparison of the discharge rate at steady state between different simulation scenarios, the walls are fixed when the orifice size reaches 0.01 m in width. Thus, the orifice width will be maintained at 0.01 m and the discharging will arrive at a steady state with constant discharge rates afterwards. The simulation ends when the hopper depletes of all particles or gets clogged.

6.3.3 Simulation scenarios

To demonstrate the impact of particle deformability and shape irregularity on granular hopper flow, the different simulation scenarios summarized in Table 6.2 are considered in this study. The first three scenarios consider different types of particles: scenario I – spherical particles, scenario II – rigid-irregular particles, and scenario III – deformable-irregular particles. Herein, the rigid-irregular particles are represented by clumps, i.e., collections of spheres (or other simple geometries such as ellipsoids) but with just rigid connections between the spheres (Lu and McDowell, 2007). In scenario II, the rigid-irregular particles have the same sphere configurations as the deformable-irregular particles shown in Figure 6.2, but consider no particle-wise deformation. These three scenarios indicate an increasing accuracy in describing particles in DEM that, on the top of scenario I for spherical particles, scenario II includes the shape irregularity and scenario III further incorporate the particle deformability.

Table 6.2: Simulation scenarios. E is the particle Young's modulus, and when a different particle Young's modulus is used, the bond normal and shear stiffness are also scaled by the same factor.

Scenarios	Description
I	Spherical particles of radius 0.5 mm, E=1e7 Pa
II	Rigid-irregular particles, fiber 85%, plate 15%, E=1e7 Pa
III	Deformable-irregular particles, fiber 85%, plate 15%, E=1e7 Pa
E-1	Deformable-irregular particles, fiber 85%, plate 15%, E=1e6 Pa
E-2	Deformable-irregular particles, fiber 85%, plate 15%, E=1e8 Pa
S-1	Deformable-irregular particles, fiber 15%, plate 85%, E=1e7 Pa
S-2	Deformable-irregular particles, fiber 30%, plate 70%, E=1e7 Pa
S-3	Deformable-irregular particles, fiber 50%, plate 50%, E=1e7 Pa
S-4	Deformable-irregular particles, fiber 70%, plate 30%, E=1e7 Pa

For deformable particles, their deformation can occur as a cause of not only external loading, but also their intrinsic properties such as particle stiffness and particle shape. For example, the fiber-shaped particles are easier to deflect than the plate-shaped particles under the same external loading. To gain a further insight into the particle deformability effects, two additional types of simulations that consider different particle stiffness or particle shapes are conducted. In scenario E-1 and E-2, particles are specified with different Young's modulus

(the bond normal and tangential stiffness are also scaled by the same factor). In scenarios S-1, S-2, S-3 and S-4, the hopper is initially charged with different ratio combinations of fiber-shaped and plate-shaped particles. Except for the differences summarized in Table 6.2, all simulations in different simulation scenarios takes the same charging and discharging procedures. As the fabric of particle packing may also affect the hopper flow behavior, each simulation scenario is carried out with five different realizations of initial packing to achieve statistically consistent results.

6.3.4   Field property post-processing

To obtain the continuum-sense properties of the flow media, such as porosity and Cauchy stress, which are not directly available from LIGGGHTS, a specific post-processing method is developed in this study. In particular, a virtual *measure* sphere is created, with its center located at the position of interest, and radius being five times the radius of base spheres, as sketched in Figure 6.3. The *measure* sphere would contain about 400~600 base spheres, which are deemed to be sufficient for a representative element volume (RVE) (Mollon and Zhao, 2013a; Guo and Zhao, 2014). The field properties (e.g., the porosity or Cauchy stress) at the position of interest are then integrated from all spheres in the *measure* sphere (i.e., the RVE). To evaluate the porosity, the number of base spheres in the RVE is counted. The solid volume fraction in the RVE is then calculated as the volume of all base spheres in the RVE divided by the volume of the RVE, and the porosity is one minus the solid volume fraction. It should be pointed out that, in the current approach, the volume of contact overlapping is not excluded when calculating the solid volume of all base spheres. However, the volume of contact overlapping is negligible considering the low compressive pressure in the current hopper flow system. To evaluate the Cauchy stress, the virial stress of each atom is first computed in LIGGGHTS. The Cauchy stress in the RVE is then calculated as the summation of the virial stress of all base spheres in the RVE divided by the volume of the RVE.

6.4   Results and discussion

This section reports the results and discussion about the hopper flow behavior in different scenarios. We will first describe the flow characteristics (e.g., packing porosity, flow pattern, and particle velocity) for the scenarios where different types of particles are used to demonstrate the effects and importance of particle deformability. Then, we will probe the particle stress and wall stress to achieve a better understanding of the stress distribution and evolution of the hopper system during discharging. Following is a more quantitative analysis about the particle stress and wall stress, as well as the discharge rate, which will be compared with classical solutions: Walker's theory and extended Beverloo's formula. Finally, we will put together the results of discharge profiles in the scenarios of different particle stiffness and shape combinations, to further explore the effects of particle size, shape and deformability on granular hopper flow.

6.4.1   Flow characteristics

The results of flow characteristics presented in this subsection were obtained from the first three scenarios described in Table 6.2: scenario I – spherical particles, scenario II – rigid-irregular particles, and scenario III – deformable-irregular particles. For these three scenarios, the results of five realizations exhibited quite similar flow characteristics with no significant deviations within the five different realizations. Thus, only one realization selected at random was used to prepare the following results.

To begin with, we display the field porosity of the initial particle packing in Figure 6.4 for these three scenarios. As it can be observed, the packing of spherical particles exhibits the lowest average porosity with a value of about 0.4, which is fairly close to the statistical lower limit 0.37 for a random packing with mono-size, smooth and rigid spheres. By including the shape irregularity into the particles, the packing porosity for rigid-irregular particles increases to 0.61. If particle deformability is further incorporated, the packing porosity only increases to 0.51, as it is in the scenario of deformable-irregular particles. It can be seen

129

that the particle deformability accounts for a porosity decrease by about 10%, based on the comparison between deformable-irregular particles and rigid-irregular particles. Overall, among the three types of particles, the packing of deformable-irregular particles presents the medium average porosity and middle level of spatial variations in the porosity field.

(a) Spherical particles   (b) Rigid-irregular particles   (c) Deformable-irregular particles
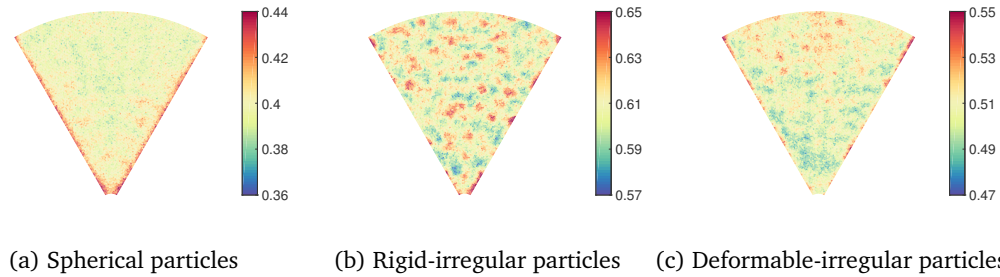
Figure 6.4: Field porosity of the initial particle packing: (a) scenario I – spherical particles, (b) scenario II – rigid-irregular particles, and (c) scenario III – deformable-irregular particles.

Recalling the testing procedures described in Section 6.3.2, the hopper walls are first raised up gradually, and then fixed when orifice width reaches 0.01 m. From the simulation results, it was observed that the hopper system in scenario I (i.e., spherical particles) and scenario III (i.e., deformable-irregular particles) displayed continuous discharging until it depleted of all particles. While in scenario II with rigid-irregular particles, the clogging issue happened right when the hopper walls stopped moving. The discharge profile over time will be further analyzed in subsequent sections. Herein, we first present and compare the flow pattern of the particles in these three scenarios. To visualize the flow pattern, the particles are colored in layers. Snapshots of the hopper flow system during discharging are taken when the percent discharge reaches 30%, 50%, 70%, and 90%, as displayed in Figure 6.5. Compared to the scenario where spherical particles are used, two main characteristics are observed in the scenario of deformable-irregular particles. First, the top surface of particle packing is concave in the middle part for deformable-irregular particles, while it is protruding for spherical particles. Second, the lateral shoulders of the packing surface are not exactly leveled during the discharging, but rather seesawing downwards with one side lower than

the other side alternately (e.g., the surface profiles at 70% and 90% discharge shown in Figure 6.5b).

(a) Spherical particles

(b) Deformable-irregular particles
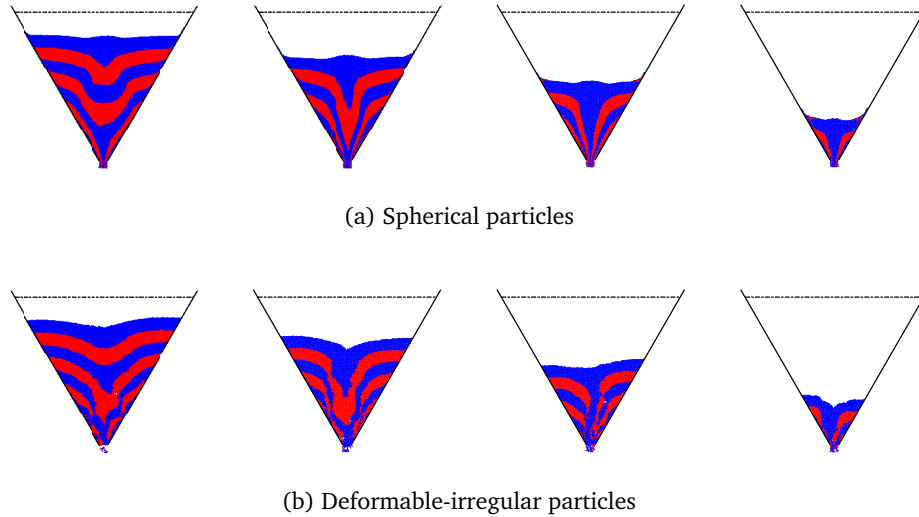
Figure 6.5: Snapshots showcasing the flow patterns when the percent discharge is at 30%, 50%, 70%, and 90%. Top row for spherical particles, and bottom row for deformable-irregular particles.

Similarly, the eventual flow pattern of rigid-irregular particles at clogging is displayed in Figure 6.6a. In this scenario, during the period when the hopper walls were raising up, particles near hopper orifice were being pushed out due to the raise of hopper wall, which accounted for about 12% of discharging. But when the walls stopped moving, the particles immediately reached equilibrium and formed stable arches, which can be reflected from the arch-shaped force chains shown in Figure 6.6b. Since then, no more particles could flow out due to the arching effects. In the work of Walker (1966), it is proposed that the critical arching (or bridging) width of a granular material is proportional to its shear strength. As rigid particles cannot deform, they exhibit more sturdy interlocking fabrics leading in a higher shear strength. The simulations and analyses imply that rigid particles exhibit a larger critical arching width than deformable particles of the same shape. The potential of clogging for a granular material in hopper flow will be overestimated by a DEM simulation if particle deformability is not considered in the model.

(a) Flow pattern   (b) Force chains
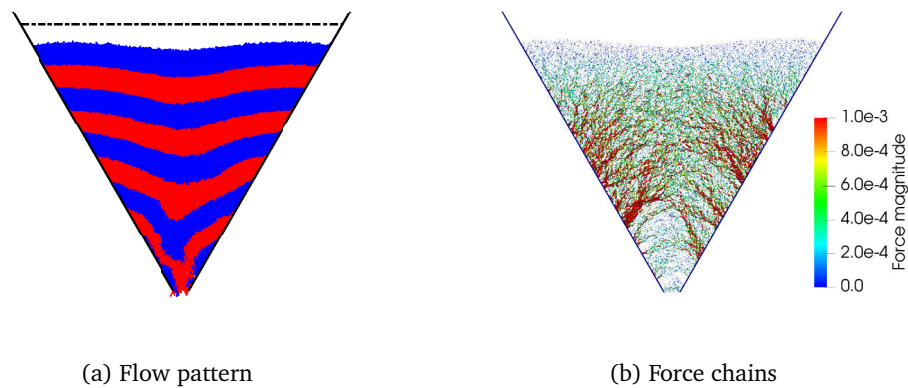
Figure 6.6: The eventual flow pattern (a) and force chains (b) in the hopper flow with rigid-irregular particles, at t = 10 s after the stable clogging issue happened.

Figure 6.7 compares the vertical velocity filed between the spherical particles and deformable-irregular particles at the state of 60% discharge. Overall, the deformable-irregular particles exhibit smaller vertical velocities than the spherical particles. In addition, the spherical particles in most ares of the hopper are mobilized with considerable large velocities. By contrast, the deformable-irregular particles that possess a velocity larger than average are more concentrated in the center and orifice areas of the hopper. As illustrated in (Lai and Chen, 2017), the particle irregularity, by enhancing the particle interlocking behaviors, can increase the mobilized friction and coordinate number, thus resulting in more kinetic energy dissipation. Compared to the spherical particles, the deformable-irregular particles would dissipate great larger amounts of kinetic energy through contact friction and collision damping, which results in the smaller vertical velocity. The velocity field and microscopic mechanisms in behind provide us an essential understanding and interpretation to help correlate hopper discharge rate with particles properties.

6.4.2   Particle and wall stresses

The particle stress and wall stress in granular hopper flow are important metrics for the design of hopper geometry or operation conditions. To get a better understanding of the

(a) Spherical particles   (b) Deformable-irregular particles
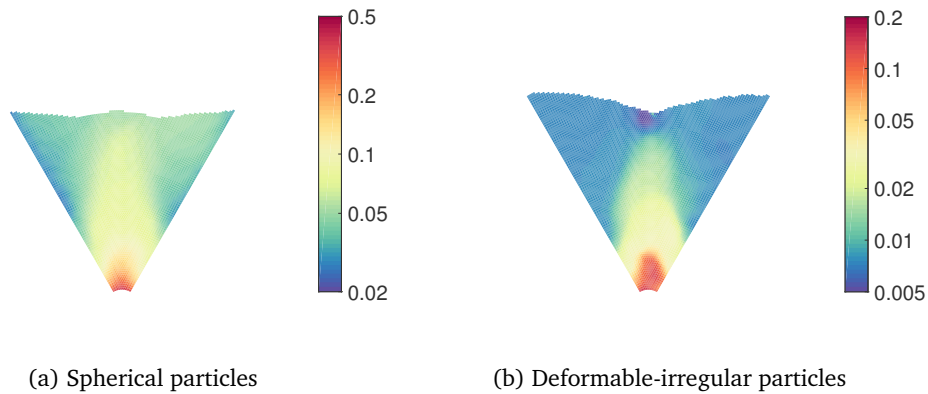
Figure 6.7: The distribution of the vertical velocity (m/s) of particles at 60% discharge: (a) spherical particles, and (b) deformable-irregular particles.

stress distribution and evolution during discharging, the particle stress and wall stress will be probed in this subsection with a focus on deformable-irregular particles only. Figure 6.8 shows the particle stress distribution in the scenario of deformable-irregular particles. In the initial packing, the horizontal and vertical stresses of the particles present an increasing gradient from top to bottom (see Figure 6.8a and Figure 6.8b). Since there is no shear stress on vertical planes, the vertical stress at any level is equivalent to self-weight of overhead particles, and the horizontal stress equals the corresponding vertical stress multiplied by a constant related to particle friction. An exception occurs in orifice vicinity where there is a slight decrease in both the vertical and horizontal stresses. This phenomenon is a result of the arching effects due to the convergent hopper walls (Walker, 1966; Nedderman, 1992). Immediately after the discharge is initiated, the particles exhibit large variations in the vertical and horizontal stresses. Most of the particles would transit from active state at which the vertical stress is the major principal stress, to passive state at which the horizontal stress turns into the major principal stress (Nedderman, 1992). As a consequence, the particles at hopper center are subject to horizontal stresses that are larger than the vertical counterparts. The contours of horizontal stress present arch-like profiles (see Figure 6.8c). As to the particles in orifice vicinity, they get little pressure due to the outflow of particles. There are also some particles near wall that present relatively large vertical stress, which may be due to

the wall friction and stagnant effects. In addition, the stress profiles also present significant fluctuations with a clear spectrum-like pattern, as it can be observed in Figure 6.8d. Such phenomenon in DEM simulations was consistent with laboratory experimental observations, which might be the outcome of decompression waves that propagate upwards at a much higher speed than the flow itself (Baxter et al., 1989).

(a) Horizontal stress, initial state

(b) Vertical stress, initial state

(c) Horizontal stress, 60% discharge

(d) Vertical stress, 60% discharge
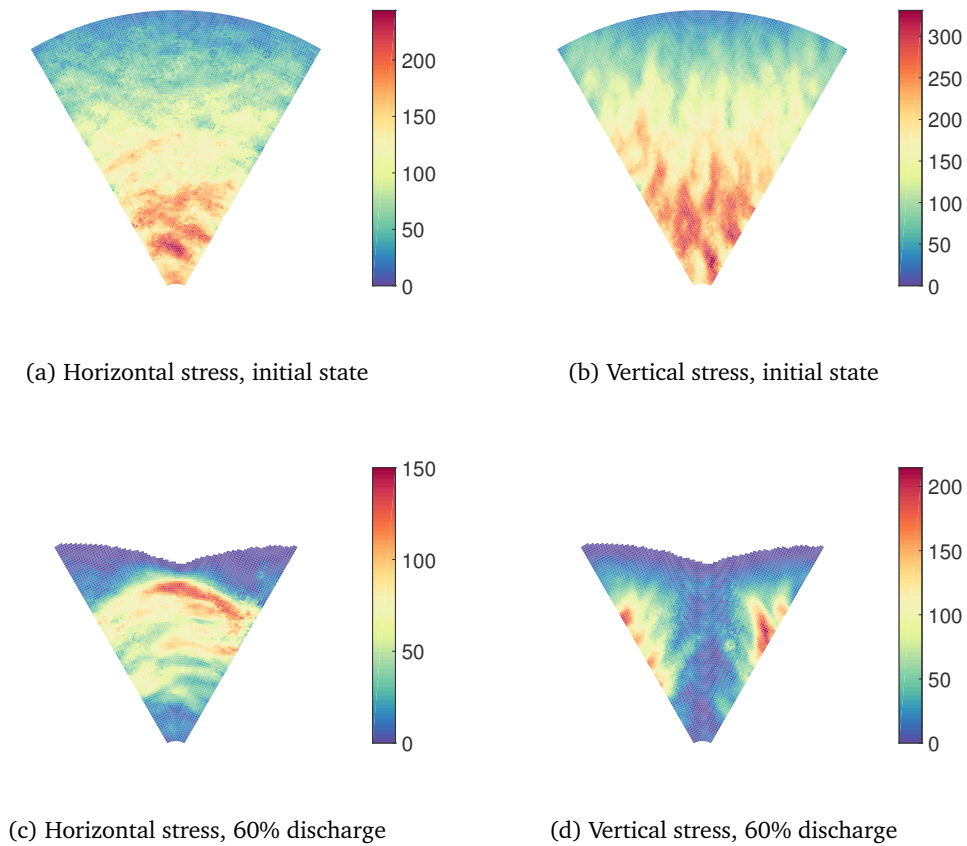
Figure 6.8: The distribution of the horizontal and vertical stresses (Pa) of particles at initial state and 60% discharge for scenario III – deformable-irregular particles.

Figure 6.9a shows the normal and shear stresses of the hopper wall at a certain location during the entire discharging process. The location being probed is about 0.035 m high from the orifice. Temporal fluctuations are clearly observed in the normal and shear stress profiles over time. The average of the stresses over time (e.g., from 10 s to 20 s), however, is asymptotically stable, which indicates a rather steady discharging. In order to

trace the correlation between the normal and shear stresses, the mobilized wall friction that defined as the ratio of shear stress to normal stress is plotted in Figure 6.9b. The mobilized wall friction over time averages out to about 0.47, which is almost equal to the specified wall friction coefficient 0.5. As a comparison, the average mobilized wall friction of spherical particles is only about 0.29 though the same wall friction is specified. The results indicate that about 40% of the wall friction cannot not mobilized without the consideration of shape irregularity effects.

(a) Normal and shear stresses   (b) Mobilized wall friction
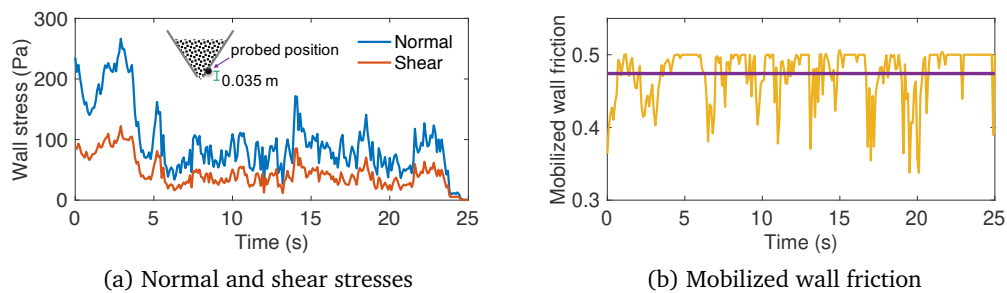
Figure 6.9: Results of (a) the normal and shear stresses of the hopper wall, and (b) the mobilized wall friction over the entire simulation for scenario I – deformable-irregular particles. The solid line in (b) indicates the average mobilized wall friction.

6.4.3   Simulations vs classical theories

To demonstrate the reliability of present DEM model, the particle stress, wall stress, and discharge rate from DEM simulations will be compared to their corresponding analytic or empirical solutions available in literature. In particular, we adopt the analytic solution developed by Walker (1966) as a benchmark for the vertical stress of particles at hopper center, and normal stress of hopper walls. As to the discharge rate, the popular empirical solution, Beverloo's formula (Beverloo et al., 1961; Nedderman, 1992), is adopted. The formulations of Walker's solution and Beverloo's formula are briefly described in Section A and Section B, respectively. Table 6.3 summaries the parameters of the Walker's solution and Beverloo's formula that will be used in the later calculations. In this table, the bulk friction angle ϕ of the particles is obtained from additional angle of repose tests, and the wall

friction angle ϕ_w is estimated from the mobilized wall friction in the hopper flow simulations. The stagnant angle ϕ_d is assumed to have the same value as the wall friction angle. The Beverloo's parameters C and λ are determined based on their empirical values as well as the simulation fittings. For detailed descriptions about these parameter, see the appendices.

Table 6.3: Parameters used in the Walker's solution (e.g., Equation 6.8) to calculate particle stress and wall stress, and in the extended Beverloo's formula (e.g., Equation 6.16) to calculate the discharge rate.

	h_0 (m)	ρ_b (kg/m^3)	α	ϕ	ϕ_w	D	C	λ	ϕ_d
Spherical particles	0.18	258	30°	18°	16°	1	0.62	1.5	16°
Deformable-irregular particles	0.18	209	30°	42°	26°	1	0.58	3.7	42°

We first present the comparison results for the scenario of spherical particles. Figure 6.10 shows the particle stress and wall stress obtained from the Walker's solution and DEM simulations for spherical particles. The stresses are calculated at the very beginning when the hopper walls just start to raise up. At this time, the particle packing transit from active state to passive state where the Walker's theory applies. As it can be observed, the particle stress and wall stress present similar profiles with an clear trend of increasing and then decreasing from top to bottom. There are some fluctuations existing in the stress profiles of DEM simulations, but not in the Walker's solution. Such fluctuations are not numerical artifacts but the facts of discrete nature and dynamic responses of granular hopper flow (Cleary and Sawley, 2002; Mollon and Zhao, 2013a). Overall, both the simulated particle stress and wall stress for the scenario of spherical particles exhibit perfect agreements with the corresponding Walker's solution.

Similarly, the particle stress and wall stress for the scenario of deformable-irregular particles are shown in Figure 6.11. The stress profiles for deformable-irregular particles exhibit quite a similar pattern as spherical particles. However, at the regions with height to head ratio around 0.2-0.4, both the simulated particle stress and wall stress are slightly higher than the counterparts of Walker's solution. A possible reason may lie in the hopper charging process. To charge the hopper, the particles are rain-falling into the hopper from a certain

(a) Vertical stress of particles (b) Normal stress along the wall
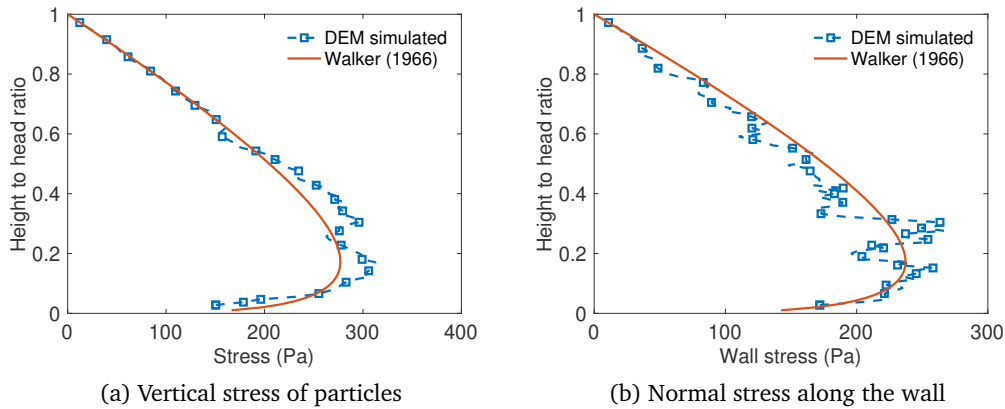
Figure 6.10: The vertical stress of the particles along the vertical cutline through hopper center (a), and normal stress along the hopper wall (b), for the model with spherical particles.

height. The particle kinetic energy would prestress the particles when they collide with each other or the hopper walls, and the prestress remains as a fact of particle interlocking. In addition to the hydrostatic pressure due to self-weight, the extra prestresses due to collision and interlocking makes the particles exhibit higher stresses than the analytical results predicted by Walker's solution. This phenomenon could be even severer for deformable-irregular particles as they exhibit stronger particle interlocking than spherical particles. Nevertheless, the simulated particle stress and wall stress exhibit reasonable consistency with the Walker's solution. The results suggest that the Walker's theory can still be used to approach a reliable estimation of the particle stress or wall stress in the granular hopper flow of deformable-irregular particles.

The results of discharge rate obtained from DEM simulations and extended Beverloo's formula are presented in Figure 6.12. Recalling the testing procedures, the hopper walls are gradually raising up during the first 6 s. In this stage, the discharge rate keeps increasing due to the increasing orifice size (i.e., from 0 to 0.01 m). Afterwards, the hopper walls are stopped moving and the orifice width is fixed at 0.01 m. During this period, the hopper maintains a constant discharge rate most of the time, except for the short period close to the end of discharging in which discharge rate starts to decrease. For both scenarios

(a) Vertical stress of particles   (b) Normal stress along the wall
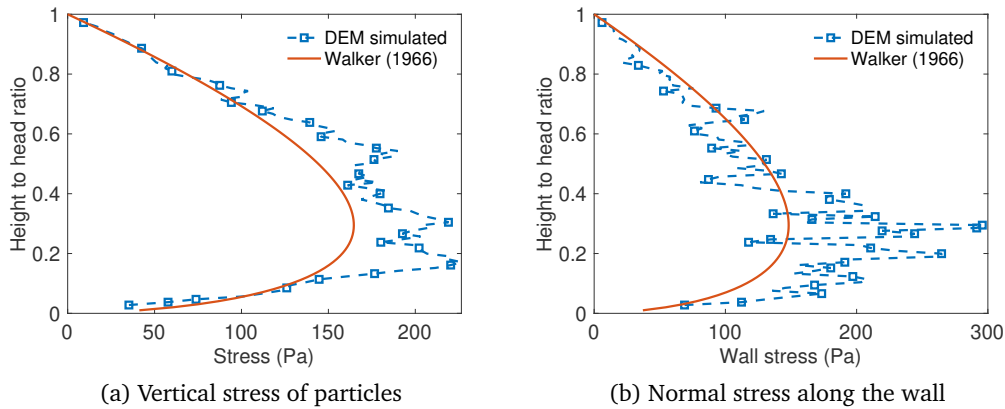
Figure 6.11: Results of (a) the vertical stress of the particles along the vertical cutline through hopper center, and (b) the normal stress of hopper wall, for scenarios III – deformable-irregular particles.

(spherical particles or deformable-irregular particles), the simulated discharge rate matches very well with the empirical results predicted by the extended Beverloo's formula. It should be pointed out that, though the parameters C and λ in the Beverloo's formula are fitted from DEM simulation, they are consistent with the suggested values reported in (Beverloo et al., 1961; Nedderman, 1992). By comparing the values of C and λ for deformable-irregular particles and spherical particles, we can identify the effects of shape irregularity on the discharge rate from two aspects. First, the shape irregularity would contribute to a granular material exhibiting a higher bulk fraction, leading to larger values of parameter C. Second, it increases empty annulus effect and thus leads to larger values of parameter λ. A quantitative correlation between shape irregularity and Beverloo's parameters would be of great value to industrial hopper design and merits more detailed study in future.

6.4.4   Effects of particle stiffness

Particle stiffness has a direct effect on the extent of particle deformation. In order to gain more insights into the effects of particle stiffness on granular hopper flow, we conducted more simulations regarding the deformable-irregular particles with different stiffness (i.e., E=1e7, 1e8 and 1e9), as summary in Table 6.2. At this time, only the results of packing

(a) Spherical particles   (b) Deformable-irregular particles
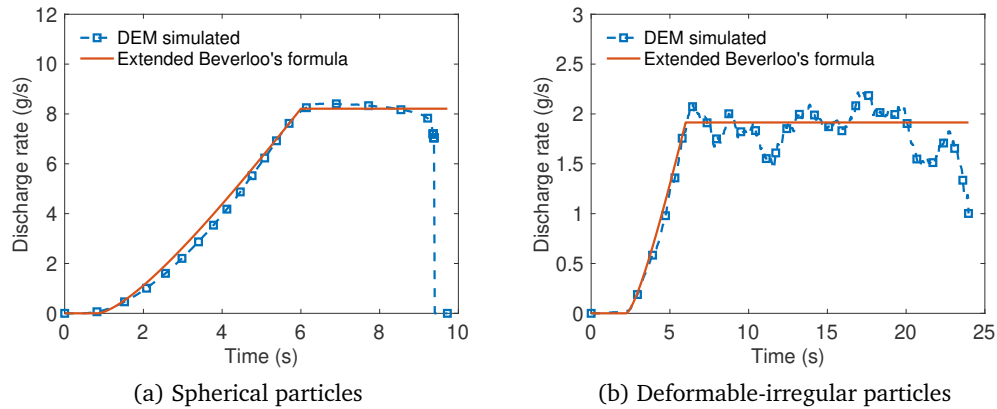
Figure 6.12: The discharge rate from DEM simulations and extended Beverloo's formula for both models: (a) spherical particles, and (b) deformable-irregular particles.

porosity and discharge profile are presented. Figure 6.13 shows the average porosity of initial packing packing for deformable-irregular particles with different stiffness, along with the porosity of spherical and rigid-irregular particles for comparison purpose. For deformable-irregular particles with different stiffness, their packing porosity all falls between the porosity of spherical particles and rigid-irregular particles. Moreover, the porosity of deformable-irregular particles exhibits a linear increasing trend as the stiffness turns higher. In fact, the particles exhibit greater potentials to form stable arches, thus leading to more voids in the packing. If the particle stiffness got extremely high, a deformable particle (i.e., the bonded spheres) would behave as a rigid one that exhibits little particle-wise deformation; and if the stiffness turned extremely low, the bonded spheres would behavior as independent spheres with rather weak constraints in between. On the whole, the deformable-irregular particles can be regarded as an intermediate state between spherical particles and rigid-irregular particles.

Figure 6.14 shows the results of discharge profile for scenarios of: deformable-irregular particles with different particle stiffness, spherical particles and rigid-irregular particles. As mentioned before, clogging issues happened in the scenarios of rigid-irregular particles, as it can be observed from the eventually unchangeable percent discharge in Figure 6.14e. For the scenarios of deformable-irregular particles with different particle
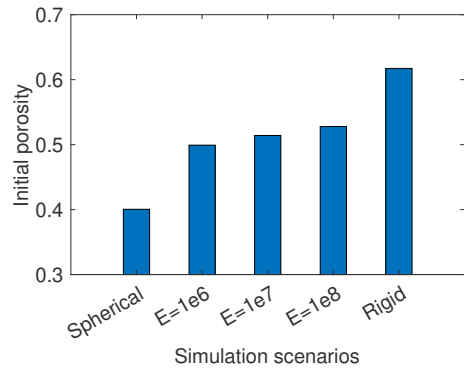
Figure 6.13: The packing porosity of deformable-irregular particles with different particle stiffness, with comparison from spherical particles and rigid-irregular particles. The x-labels $E = $ 1e6, 1e7 or 1e8 indicate the particle Young's modulus of deformable-irregular particles.

stiffness, the five different realizations present pretty consistent discharge profiles (see Figure 6.14a – Figure 6.14c). A weak trend that higher particle stiffness results in slightly greater variations in the discharge profiles between each realization is also observed though. By comparing the discharge profiles of deformable-irregular particles with different particle stiffness, it is found that the time needed for full discharge increases as the particle stiffness gets higher. That is to say, the discharge rate of granular hopper flow is negatively correlated to the particle stiffness for deformable-irregular particles.

6.4.5 Effects of particle size and shape

Lastly, we will discuss about the effects of particle size and shape on granular hopper flow on the premise of deformable-irregular particles. The simulation scenarios regarding different combinations of shape templates have been described in Table 6.2. Again, we will place the focuses on the packing porosity and discharge profiles. Figure 6.15 plots the porosity of particle packing with different particle combinations. It is observed that, the packing porosity decreases as the corresponding particle packing contains more fiber-shaped particles. In another word, more fiber-shaped particles consisting in the packing makes the packing denser. Actually, the fiber-shaped particles get smaller bending stiffness (i.e., moment of inertia). They would exhibit greater deflection under the same external loading,

140
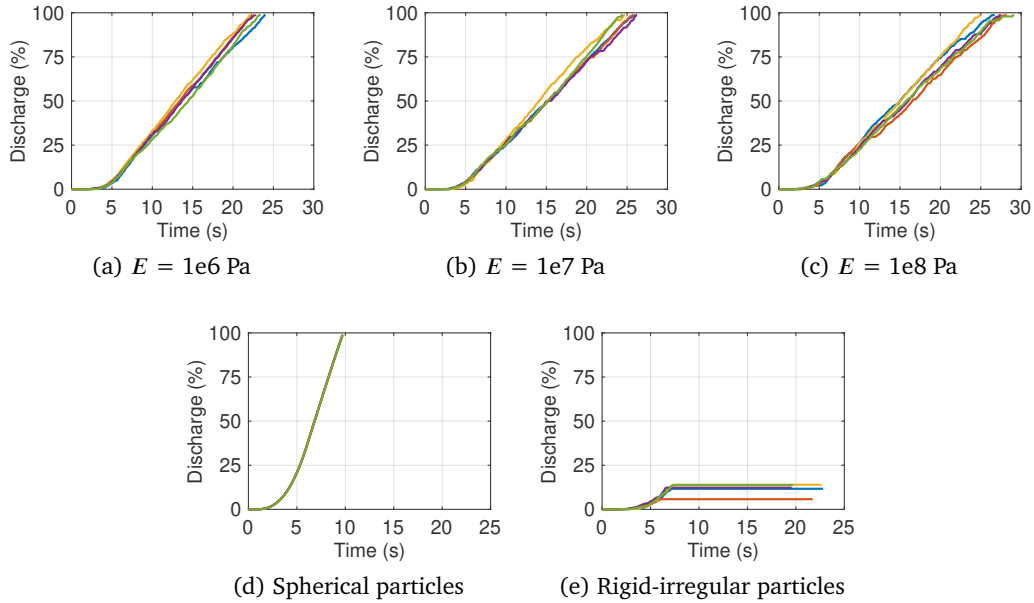
Figure 6.14: The discharge profiles in different simulation scenarios: (a-c) deformable-irregular particles with different particle stiffness, i.e., E=1e6, 1e7 and 1e8, respectively, (d) spherical particles, and (d) rigid-irregular particles.

and thus it becomes more difficult for them to form wide-range arch structures to support the pore spaces. The collapse of the pore voids leads to a denser packing.

The discharge profiles for deformable-irregular particles with different shape combinations are gathered in Figure 6.16. The effects of shape combinations on the discharge profile can be classified into two types, depending on whether the fiber-shaped particles or the plate-shaped particles are dominating the packing (e.g., have a mass ratio greater than 50%). First, if the plate-shaped particles are dominating the packing like the scenarios of Figure 6.16(a-c), more plate-shaped particles in the packing would lead to a greater tendency of clogging. This phenomenon can be partially interpreted by the fact that the plate-shaped particles have a greater geometric size than the fiber-shaped particles, more plate-shaped particles would require a relative larger orifice size to maintain a continuous outflow. Second, if the fiber-shaped particles are dominating the packing, to increase the fraction of fiber-shaped particles would result in a reduced discharge rate, which is supported by the observation in Figure 6.16(c-e) that the model with higher fraction of fiber-shaped
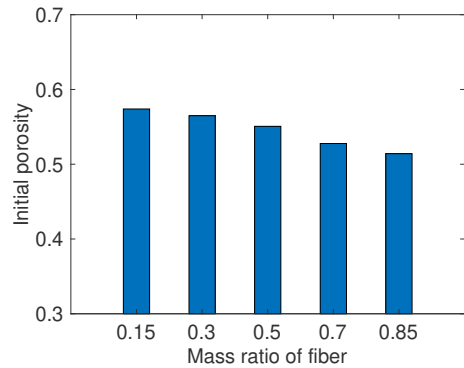
Figure 6.15: The packing porosity of deformable-irregular particles with different fractions of fiber-shaped and plate-shapes particles.

particles requires a longer time for full discharge. This phenomenon could be essentially related to the particle kinetic energy and dissipation. The fiber-shaped particles have larger aspect ratio, which would greatly increase the particle inter-locking, which leads to more energy dissipation and thus hinders the discharging. The observations and conclusions on the basis of these scenarios shed partial light on the effects of particle size and shape on granular hopper flow, although these scenarios only involved limited variants of particle size and shape.

6.5 Conclusions

In this work, the irregular shape and particle-wise deformation of a flexible particle was able to be captured in DEM with employment of the bonded-sphere model. Based on the bonded-sphere DEM approach, the flow behaviors of deformable-irregular particles in a wedge-shaped hopper have been studied. Three sets of simulation scenarios have been considered: 1) spherical particles vs. rigid-irregular particles vs. deformable-irregular particles, 2) deformable-irregular particles of different particle stiffness, and 3) deformable-irregular particles of different shape combinations. On the basis of these simulations, qualitative as well as quantitative analyses have been performed for the hopper flow characteristics, includ-

142

(a) 15% fiber, 85% plate   (b) 30% fiber, 70% plate   (c) 50% fiber, 50% plate

(d) 70% fiber, 30% plate   (e) 85% fiber, 15% plate
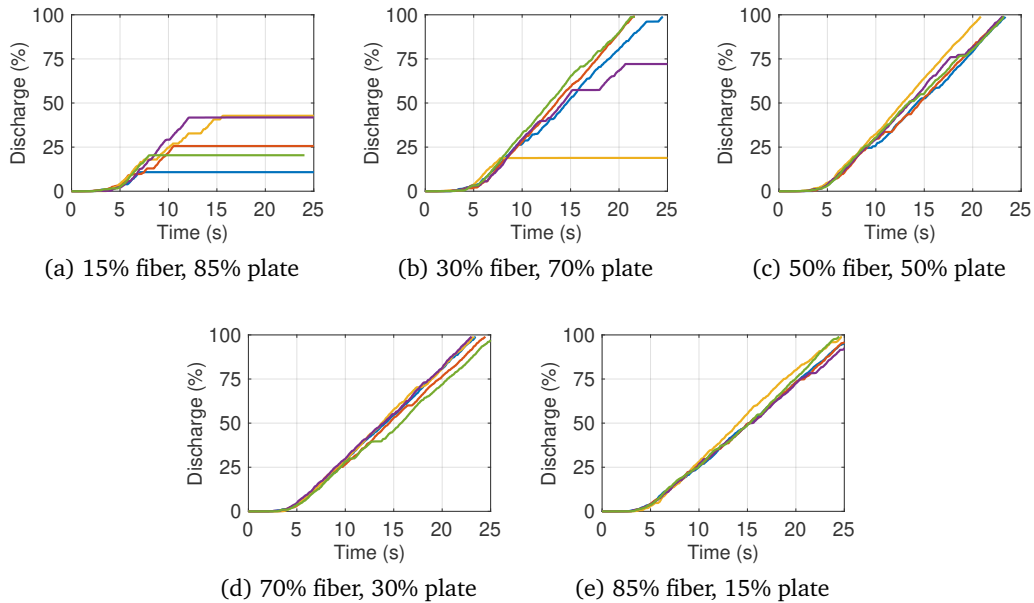
Figure 6.16: The discharge profiles of deformable-irregular particles with different fractions of fiber-shaped and plate-shapes particles.

ing packing porosity, flow pattern, particle velocity, particle and wall stress, and discharge profiles. The main findings of this work are concluded as follows:

1. Compared to rigid-irregular particles, deformable-irregular particles show lower packing porosity and smaller critical arching width. Without the consideration of particle deformability, the potential of clogging for a granular material in hopper flow will be overestimated by a DEM simulation.

2. The particle stress and wall stress for deformable-irregular particles exhibit significant temporal and spatial fluctuations, but find themselves in reasonable agreement with the Walker's solution. The discharge rate can be well fitted by the extended Beverloo's formula, while the correlation between particle properties (e.g., size, shape and deformability) and Beverloo's parameters merits further study.

3. On the premise of deformable-irregular particles, stiffer particles would result in higher packing porosity, and smaller discharge rate. The flow behavior of stiffer particles show

larger variations among different simulation realizations, indicating greater sensitivity to the particle fabrics.

4. For packings of fiber-shaped and plate-shape particles, the porosity is decreasing with the increasing ratio of fiber-shaped particles. More plate-shaped particles would contribution to higher potential of clogging, while more fiber-shaped particles would result in smaller discharge rate.

The present work, by considering deformable-irregular particles, sheds partial light on the effects of particle size, shape and deformability on granular hopper flow. The importance of taking into account the particle deformability in hopper flow simulations regarding flexible granular materials has been demonstrated. Preliminary investigations of the particle size and shape effects on discharge rate have been made but merit further quantitative analyses. Future work will be to polish the current DEM model by including a wider range of sizes and a greater variety of shapes, and to approach quantitative relations between discharge rate and particle properties that are suitable to flexible granular materials.

Appendix A   Particle and wall stress: Walker's theory

To calculate the particle stress or wall stress during discharging, Walker (1966) developed an analytic solution based on the slice element method. According to (Walker, 1966), the average vertical stress $\bar{\sigma}_v$ of the particles, and the normal stress σ_n of hopper wall at any height h, can be calculated as

$$\bar{\sigma}_v = \frac{\rho_b g h}{\xi - 1} \left[1 - \left(\frac{h}{h_0} \right)^{\xi - 1} \right] \tag{6.7}$$

$$\sigma_n = D\bar{\sigma}_v \frac{1 + \sin\phi \cos 2\beta}{1 - \sin\phi \cos 2(\alpha + \beta)} \tag{6.8}$$

in which

$$\beta = \frac{1}{2}\left[\phi_w + \arcsin\left(\frac{\sin\phi_w}{\sin\phi}\right)\right] \tag{6.9}$$

$$\xi = \frac{D\sin\phi\sin 2(\alpha+\beta)}{\tan\alpha[1-\sin\phi\cos 2(\alpha+\beta)]} \tag{6.10}$$

where h_0 is the initial filled height; ρ_b is the bulk density; g is the acceleration; α is the hopper half-angle; ϕ is the angle of internal friction of the bulk material; ϕ_w is the angle of internal friction between the bulk material and the hopper; D is the stress distribution factor, which may take unity for simplicity (Walker, 1966).

Appendix B   Discharge rate: extended Beverloo's formula

Based on the experimental results of various materials and hopper geometries, Beverloo et al. (1961) proposed an empirical formula predicting the discharge rate W_B of granular hopper flow, that

$$W_B = C\rho_b\sqrt{g}(D_0 - \lambda d)^{2.5} \tag{6.11}$$

where C is a unit-less coefficient that depends on the particle friction and wall friction, D_0 is the diameter of the orifice, λ is a shape factor accounting for the particle shape effects, and d is the particle diameter. The friction relevant parameter C normally takes a value in the range from 0.58 (for high-friction particles) to 0.64 (for exceptionally smooth particles) (Nedderman, 1992). The shape factor λ is about 1.4 for spherical particles, and may take larger values for angular particles (e.g., 2.9 for sand) (Beverloo et al., 1961; Nedderman, 1992).

Beverloo's formula is also applicable to non-circular orifices, such as square, rectangle or triangle, by taking the modified form Nedderman (1992)

$$W_B = \frac{4C}{\pi}\rho_b A'\sqrt{gD_h'} \tag{6.12}$$

where A' and D'_h are the effective area and effective hydraulic diameter of the orifice after the removal of empty annulus. For the example of a $b \times l$ rectangle orifice, the A' and D'_h are calculated as

$$A' = (b - \lambda d)(l - \lambda d) \tag{6.13}$$

$$D'_h = \frac{A'}{(b + l - 2\lambda d)/2} \tag{6.14}$$

As pointed out by Nedderman (1992), the Beverloo's formula is applicable only for bunkers or hoppers with funnel flow behavior. In the case of mass flow, the effect of the hopper half-angle α becomes important. Thus, Nedderman (1992) proposed to extend the Beverloo's formula with a mass flow coefficient $F(\alpha, \phi_d)$, such that

$$W = W_B F(\alpha, \phi_d) \tag{6.15}$$

in which

$$F(\alpha, \phi_d) = \begin{cases} (\tan \alpha \tan \phi_d)^{-0.35}, & \text{if } \alpha < 90° - \phi_d \\ 1, & \text{otherwise} \end{cases} \tag{6.16}$$

where W is the modified outflow rate, and ϕ_d is the angle between the stagnant zone boundary and the horizontal. The condition $\alpha < 90° - \phi_d$ can be regarded as a mass flow criterion.

Chapter 7

Conclusions and recommendations

7.1   Summary of conclusions

In this dissertation, discrete element modeling of the grading- and shape-dependent behavior of granular materials has been performed. A framework to reconstruct granular particles from X-ray computed tomography (X-ray CT) using the Trainable Weka Seg- mentation (TWS) machine learning tool and the level set method has been proposed (Chapter 3). DEM models have been developed with the consideration of particle size, shape and deformability. The behavior of granular materials in representative problems, i.e., direct shear (Chapter 4), cyclic compression (Chapter 5) and hopper flow (Chapter 6), are simulated and studied. Special attentions have been paid to study the effects of particle size, shape and deformability on the bulk mechanical behavior of granular materials. The key features and findings for the main chapters (chapters 3 to 6) are summarized as follows:

Chapter 3, reconstructing granular particles from X-ray computed tomography using the TWS machine learning tool and the level set method:

A novel machine learning and level set-based framework is proposed to segment X-ray CT images of granular geomaterials and to reconstruct realistic 3D particle shapes. In particular, a feature-based machine learning technique termed the Trainable Weka Segmentation is implemented and utilized to segment X-ray CT images. The resultant probability

map is then used as the basis for the subsequent 3D edge-based level set method to approach an accurate shape representation of real particles. Realistic 3D particles of the Mojave Mars simulant regolith are successfully reconstructed from raw CT images. Quantitative accuracy analyses are performed for the proposed framework and a conventional watershed method. The analyses show that the proposed framework has superior performance in both pixel-based classification accuracy and particle-based segmentation accuracy. The particle size distribution using the reconstructed particles are also validated and compared well with results from a lab sieve analysis. In addition, the morphological features, e.g., sphericity, roundness, and roughness, of real particle shapes are well captured. Quantitative particle morphology analyses are performed to provide more insights into the morphological features of the granular material.

<u>Chapter 4</u>, characterization and discrete element simulation of grading- and shape-dependent behavior of JSC-1A Martian regolith simulant:

The physical and mechanical properties of JSC-1A Martian regolith simulant (MRS) are characterized, including specific gravity, particle sizes, particle shapes and shear strength. X-ray CT technique is used to obtain particle images, upon which particle shape data are characterized by a series of imaging processing techniques and are further used to generated irregularly-shaped numerical particles through the domain overlapping filling method. DEM simulations of the direct shear test have been conducted by using irregular particles, spherical particles with or without rolling resistance. It is found that the calibrated grading and shape-dependent DEM model can well capture the behavior of the regolith simulant in a direct shear test, in particular, the peak shear strength and the maximum friction angle. The particle shape effect accounts for approximately 40% of the shear resistance of the JSC-1A MRS. The irregular particles would increase the mobilized contact friction and the number of particle contacts within the assembly when compared with an assembly with the same number of disc-shaped particles. The additional shear resistance caused by the irregular

particle shape effect cannot be fully replicated by solely increasing the micro-friction between particles but can be captured through a calibration of rolling resistance contact model.

[Chapter 5]{.chapter-ref}, discrete element modeling of deformable pinewood chips in cyclic loading test:

A bonded-sphere DEM model based simulation approach has been presented for studying the mechanical behavior of bulk flexible, deformable pinewood chips. Clustered spheres that can bend and twist via elastic bonds have been used to model irregular-shape pinewood particles. Based on the bonded-sphere DEM model, simulations of cyclic compression tests have been conducted to predict the bulk mechanical properties of pinewood chips. With careful calibration, the bulk densities and compressive moduli of elasticity obtained in the simulations have reached good agreements with the experimental results. However, it has been found challenging for the present DEM model to accurately predict the overall stress-strain behavior of bulk pinewood chips, especially the large sustained plastic deformation during the unloadings. Compared with most past DEM works that simulated the bulk flow of woodchips with simple rigid spheres, rods or blocks, the present work has demonstrated the importance for a DEM model to account for the particle irregular shapes and deformability, in order to better predict the mechanical behavior of bulk woodchips. The simulation results provide valuable information to help improve the design of biomass feeding and handling equipment.

[Chapter 6]{.chapter-ref}, discrete element modeling the granular hopper flow of deformable-irregular particles:

The granular hopper flow with deformable-irregular particles under different simulation conditions (e.g., different particle stiffness and shape combinations) is simulated and the flow characteristics are studied based on the bonded-sphere DEM model. The same hopper flow simulation while using spherical particles or rigid-irregular particles are also conducted as comparisons. The simulation results indicate that deformable-irregular particles exhibit similar flow characteristics to those that are typically observed in laboratory

experiments or DEM simulations of general granular materials. Compared to rigid-irregular particles, deformable-irregular particles show lower packing porosity and smaller critical arching width. The particle stress and wall stress for deformable-irregular particles exhibit significant temporal and spatial fluctuations but find themselves in reasonable agreement with the Walker's solution. The discharge rate can be well fitted by the extended Beverloo's formula. On the premise of deformable-irregular particles, stiffer particles would result in a higher packing porosity and a smaller discharge rate. For packings of fiber-shaped and plate-shaped particles, the porosity is decreasing with the increasing ratio of fiber-shaped particles. More plate-shaped particles would contribute to a higher potential of clogging, while more fiber-shaped particles would result in a smaller discharge rate. These simulation results, by considering deformable-irregular particles, shed lights on the effects of particle size, shape and deformability on the granular hopper flow and would be of useful reference for industrial hopper design.

7.2   Recommendations for future research

There are several possible improvements to the studies presented in this dissertation. As shown in Chapter 3, the machine learning technique exhibits great potentials in segmenting CT images of geomaterials with complex constituents. The current work applied machine learning technique to process 2D images. An immediate step would be to promote the current 2D machine learning approach into the 3D regime, where image features from the third dimension are included in the segmentation process synchronously. It is also noticed that there are several competing machine learning-based image segmentation algorithms. It would be interesting to explore alternative methods and compare their performances when applied to granular geomaterials. As an initial study, Chapter 4 performed the DEM modeling of Martian soil simulant in 2D. Compared to 3D simulations, the 2D simulations require much less computational expenses, while they could still capture most of the typical

characteristics and mechanisms in shearing granular materials. An improvement would be to directly perform the 3D DEM simulations following the same workflow.

By employing the bonded-sphere model, the irregular shape and particle-wise deformation of a flexible particle such as a pine woodchip can be captured by the DEM simulations conducted in Chapter 5 and Chapter 6. However, it was observed from laboratory experiments that the pinewood chip samples exhibited large sustained plastic deformation after unloading, which may due to continuously pore collapse during loading. This phenomenon was not well captured by the current DEM model. One way to promote the modeling fidelity is to employ smaller particles in order to create more complex-shape particles that can maintain a highly porous meanwhile quasi-stable DEM specimen. One that other hand, elasto-plastic models such as the works of Luding (2005a,b) could be incorporated to help sustain large plastic deformation after unloading. To promote the merits of hopper flow simulation results in Chapter 6 to industrial hopper design, further work is required to approach quantitative relations between the particle characteristics (e.g., size, shape or stiffness) and the discharge rate. In this regard, the particle size and shape should be quantified and more parametric studies by varying grading, shape and particle stiffness would be involved.

Lastly, as DEM based numerical simulations are highly-computationally intensive, it becomes a great challenge to achieve a balance between model complexity and computational expenses and to scale the DEM simulations up to pilot-scale production applications. To approach this challenge, one direction is to simplify the DEM model by just accounting for the most sensitive physical properties of particles (e.g., the size, shape, and deformability). This is, however, not possible without better understandings of the effects of the various particle physical and morphological properties on granular flow behaviors. Another direction is to couple with large-scale continuum methods such as finite element method or material point method through multiscale frameworks. The research outcomes of addressing this challenge would also help enhance the modeling fidelity of the DEM simulations performed in this work and promote their merits to engineering and industrial systems.

Bibliography

Abbaspour-Fard, M. (2004). Theoretical validation of a multi-sphere, discrete element model suitable for biomaterials handling simulation. *Biosystems Engineering,* 88(2):153–161. (p. 88)

Al-Kofahi, Y., Lassoued, W., Lee, W., and Roysam, B. (2010). Improved automatic detection and segmentation of cell nuclei in histopathology images. *IEEE Transactions on Biomedical Engineering*, 57(4):841–852. (p. 25)

Allaire, S. and Parent, L. (2003). Size guide number and Rosin–Rammler approaches to describe particle size distribution of granular organic-based fertilisers. *Biosystems engineering,* 86(4):503–509. (p. 63, 64)

Allen, C., Jager, K., Morris, R., Lindstrom, D., Lindstrom, M., and Lockwood, J. (1998). JSC Mars-1: a Martian soil simulant. In *Space 98*, pages 469–476. American Society of Civil Engineers. (p. 58, 60)

Alonso-Marroquín, F. and Herrmann, H. (2002). Calculation of the incremental stress-strain relation of a polygonal packing. *Physical Review E*, 66(2):021301. (p. 72)

Alonso-Marroquin, F., Luding, S., Herrmann, H., and Vardoulakis, I. (2005). Role of anisotropy in the elastoplastic response of a polygonal packing. *Physical Review E*, 71(5):051304. (p. 82)

Alonso-Marroquín, F. and Wang, Y. (2009). An efficient algorithm for granular dynamics simulations with complex-shaped objects. *Granular Matter,* 11(5):317–329. (p. 74)

Andò, E., Viggiani, G., Hall, S., and Desrues, J. (2013). Experimental micro-mechanics of granular media studied by X-ray tomography: recent results and challenges. *Géotechnique Letters*, 3(3):142–146. (p. 24)

Andrade, J. and Avila, C. (2012). Granular element method (GEM): linking inter-particle forces with macroscopic loading. *Granular Matter*, 14(1):51–61. (p. 7)

Andrade, J., Chen, Q., Le, P., Avila, C., and Evans, T. (2012a). On the rheology of dilative granular media: bridging solid-and fluid-like behavior. *Journal of the Mechanics and Physics of Solids*, 60(6):1122–1136. (p. 7, 13, 57)

Andrade, J., Lim, K., Avila, C., and Vlahinić, I. (2012b). Granular element method for computational particle mechanics. *Computer Methods in Applied Mechanics and Engineering*, 241:262–274. (p. 74)

Andrade, J., Vlahinić, I., Lim, K., and Jerves, A. (2012c). Multiscale 'tomography-to-simulation' framework for granular matter: the road ahead. *Géotechnique Letters*, 2(3):135–139. (p. 24, 45)

Arasan, S., Akbulut, S., and Hasiloglu, A. (2011). The relationship between the fractal dimension and shape properties of particles. *KSCE Journal of Civil Engineering*, 15(7):1219–1225. (p. 78)

Arganda-Carreras, I., Kaynig, V., Rueden, C., Eliceiri, K., Schindelin, J., Cardona, A., and Sebastian Seung, H. (2017). Trainable Weka Segmentation: a machine learning tool for microscopy pixel classification. *Bioinformatics*, 33(15):2424–2426. (p. 27, 31, 32)

Arganda-Carreras, I., Turaga, S., Berger, D., Cireşan, D., Giusti, A., Gambardella, L., Schmidhuber, J., Laptev, D., Dwivedi, S., Buhmann, J., et al. (2015). Crowdsourcing the creation of image segmentation algorithms for connectomics. *Frontiers in Neuroanatomy*, 9(14):1–13. (p. 46)

Aubert, G. and Kornprobst, P. (2006). *Mathematical problems in image processing: partial differential equations and the calculus of variations - 2nd edition*, volume 147. Springer Science & Business Media. (p. 37)

Avendi, M., Kheradvar, A., and Jafarkhani, H. (2016). A combined deep-learning and deformable-model approach to fully automatic segmentation of the left ventricle in cardiac MRI. *Medical Image Analysis*, 30:108–119. (p. 26)

Balevičius, R., Kačianauskas, R., Mróz, Z., and Sielamowicz, I. (2008). Discrete-particle investigation of friction effect in filling and unsteady/steady discharge in three-dimensional wedge-shaped hopper. *Powder Technology*, 187(2):159–174. (p. 118)

Balevičius, R., Kačianauskas, R., Mroz, Z., and Sielamowicz, I. (2011). Analysis and DEM simulation of granular material flow patterns in hopper models of different shapes. *Advanced Powder Technology*, 22(2):226–235. (p. 118)

Barletta, D. and Poletto, M. (2013). An assessment on silo design procedures for granular solid biomass. *Chemical Engineering Transactions*, 32:2209–2214. (p. 86)

Baxter, G., Behringer, R., Fagert, T., and Johnson, G. (1989). Pattern formation in flowing sand. *Physical Review Letters*, 62(24):2825. (p. 134)

Behraftar, S., Galindo Torres, S., Scheuermann, A., Williams, D., Marques, E., and Janjani Avarzaman, H. (2017). A calibration methodology to obtain material parameters for the representation of fracture mechanics based on discrete element simulations. *Computers and Geotechnics*, 81:274–283. (p. 78)

Belheine, N., Plassiard, J., Donzé, F., Darve, F., and Seridi, A. (2009). Numerical simulation of drained triaxial test using 3D discrete element modeling. *Computers and Geotechnics*, 36(1):320–331. (p. 78)

Berger, K. and Hrenya, C. (2014). Challenges of DEM: II. Wide particle size distributions. *Powder Technology*, 264:627–633. (p. 7)

Beverloo, W., Leniger, H., and Van de Velde, J. (1961). The flow of granular solids through orifices. *Chemical Engineering Science*, 15(3-4):260–269. (p. 135, 138, 145)

Blott, S. and Pye, K. (2008). Particle shape: a review and new methods of characterization and classification. *Sedimentology*, 55(1):31–63. (p. 39)

Brendel, L. and Dippel, S. (1998). Lasting contacts in molecular dynamics simulations. In *Physics of dry granular media*, pages 313–318. Springer. (p. 72)

Bruchon, J., Pereira, J., Vandamme, M., Lenoir, N., Delage, P., and Bornert, M. (2013). Full 3D investigation and characterisation of capillary collapse of a loose unsaturated sand using X-ray CT. *Granular Matter*, 15(6):783–800. (p. 24)

Brunskill, C., Patel, N., Gouache, T., Scott, G., Saaj, C., Matthews, M., and Cui, L. (2011). Characterisation of martian soil simulants for the ExoMars rover testbed. *Journal of Terramechanics*, 48(6):419–438. (p. 58)

Bui, D., Hu, J., and Stroeven, P. (2005). Particle size effect on the strength of rice husk ash blended gap-graded portland cement concrete. *Cement and concrete composites*, 27(3):357–366. (p. 2)

Carranza, S., Makel, D., Blizman, B., and El-Genk, M. (2006). In situ manufacturing of plastics and composites to support H&R exploration. In *AIP Conference Proceedings*, volume 813, pages 1122–1129. AIP. (p. 57)

Chehreghani, S., Noaparast, M., Rezai, B., and Shafaei, S. (2017). Bonded-particle model calibration using response surface methodology. *Particuology*, 32:141–152. (p. 20, 124)

Chen, C., Luo, J., and Parker, K. (1998). Image segmentation via adaptive K-mean clustering and knowledge-based morphological operations with biomedical applications. *IEEE transactions on image processing*, 7(12):1673–1683. (p. 67)

Chen, Q. (2011). *Multiscale Modeling of Failure in Granular Media: From Continuum Scales to Granular Scale*. PhD thesis, Northwestern University. (p. 7)

Chen, Q., Andrade, J., and Samaniego, E. (2011). AES for multiscale localization modeling in granular media. *Computer Methods in Applied Mechanics and Engineering*, 200(33):2473–2482. (p. 57)

Cheng, L., Cord-Ruwisch, R., and Shahin, M. (2013). Cementation of sand soil by microbially induced calcite precipitation at various degrees of saturation. *Canadian Geotechnical Journal*, 50(1):81–90. (p. 23)

Cho, G., Dodds, J., and Santamarina, J. (2006). Particle shape effects on packing density, stiffness, and strength: natural and crushed sands. *Journal of Geotechnical and Geoenvironmental Engineering*, 132(5):591–602. (p. 2)

Cho, N., Martin, C., and Sego, D. (2007). A clumped particle model for rock. *International Journal of Rock Mechanics and Mining Sciences*, 44(7):997–1010. (p. 88)

Chung, Y. (2006). *Discrete element modelling and experimental validation of a granular solid subject to different loading conditions*. PhD thesis, University of Edinburgh. (p. x, 9, 10, 15, 91, 123)

Cleary, P. (2009). Industrial particle flow modelling using discrete element method. *Engineering Computations*, 26(6):698–743. (p. 6)

Cleary, P. and Sawley, M. (2002). DEM modelling of industrial granular flows: 3D case studies and the effect of particle shape on hopper discharge. *Applied Mathematical Modelling*, 26(2):89–111. (p. 88, 118, 136)

Coetzee, C. (2017). Review: Calibration of the discrete element method. *Powder Technology*, 310:104–142. (p. 20, 88, 124)

Colombo, A., Cusano, C., and Schettini, R. (2006). 3D face detection using curvature analysis. *Pattern recognition*, 39(3):444–455. (p. 41)

Cox, M. and Budhu, M. (2008). A practical approach to grain shape quantification. *Engineering Geology*, 96(1):1–16. (p. 24)

Cundall, P. and Strack, O. (1979). A discrete numerical model for granular assemblies. *Géotechnique*, 29(1):47–65. (p. 2, 6, 8, 11, 16, 24, 57, 72, 87, 91, 117, 123)

Dadda, A., Geindreau, C., Emeriault, F., du Roscoat, S., Garandet, A., Sapin, L., and Filet, A. (2017). Characterization of microstructural and physical properties changes in biocemented sand using 3D X-ray microtomography. *Acta Geotechnica*, 12(5):955–970. (p. 23)

D'Addetta, G., Kun, F., and Ramm, E. (2002). On the application of a discrete model to the fracture process of cohesive granular materials. *Granular matter*, 4(2):77–90. (p. 13)

Dai, B., Yang, J., and Zhou, C. (2015). Observed effects of interparticle friction and particle size on shear behavior of granular materials. *International Journal of Geomechanics*, 16(1):04015011. (p. 3)

Das, N. (2007). *Modeling three-dimensional shape of sand grains using discrete element method*. PhD thesis, University of South Florida. (p. 13, 69, 74)

DeJong, J., Soga, K., Kavazanjian, E., Burns, S., Van Paassen, L., Al Qabany, A., Aydilek, A., Bang, S., Burbank, M., Caslake, L., et al. (2013). Biogeochemical processes and geotechnical applications: progress, opportunities and challenges. *Géotechnique*, 63(4):287–301. (p. 23)

Desrues, J., Viggiani, G., and Besuelle, P. (2010). *Advances in X-ray tomography for geomaterials*, volume 118. John Wiley & Sons. (p. 24)

Di Renzo, A. and Di Maio, F. (2005). An improved integral non-linear model for the contact of particles in distinct element simulations. *Chemical Engineering Science*, 60(5):1303–1312. (p. 8, 17, 93, 123)

Ding, L., Gao, H., Deng, Z., Nagatani, K., and Yoshida, K. (2011). Experimental study and analysis on driving wheels' performance for planetary exploration rovers moving in deformable soil. *Journal of Terramechanics*, 48(1):27–45. (p. 57)

Ding, X., Zhang, L., Zhu, H., and Zhang, Q. (2014). Effect of model scale and particle size distribution on PFC3D simulation results. *Rock mechanics and rock engineering*, 47(6):2139–2156. (p. 3)

Dobrohotoff, P., Azeezullah, S., Maggi, F., and Alonso-Marroquin, F. (2012). Optimal description of two-dimensional complex-shaped objects using spheropolygons. *Granular Matter*, pages 1–8. (p. 74)

Ersoy, A. and Waller, M. (1995). Textural characterisation of rocks. *Engineering Geology*, 39(3-4):123–136. (p. 39)

Estrada, N. (2016). Effects of grain size distribution on the packing fraction and shear strength of frictionless disk packings. *Physical Review E*, 94(6):062903. (p. 3)

Faber, V. (1994). Clustering and the continuous k-means algorithm. *Los Alamos Science*, 22(138144.21). (p. 67)

Feng, K., Montoya, B., and Evans, T. (2017a). Discrete element method simulations of bio-cemented sands. *Computers and Geotechnics*, 85:139–150. (p. 73, 79)

Feng, Y., Han, K., and Owen, D. (2017b). A generic contact detection framework for cylindrical particles in discrete element modelling. *Computer Methods in Applied Mechanics and Engineering*, 315:632–651. (p. 12)

Fernández-Delgado, M., Cernadas, E., Barro, S., and Amorim, D. (2014). Do we need hundreds of classifiers to solve real world classification problems. *J. Mach. Learn. Res*, 15(1):3133–3181. (p. 28)

Fleissner, F., Gaugele, T., and Eberhard, P. (2007). Applications of the discrete element method in mechanical engineering. *Multibody System Dynamics*, 18(1):81. (p. 121)

Gao, H. and Chae, O. (2010). Individual tooth segmentation from CT images using level set method with shape and intensity prior. *Pattern Recognition*, 43(7):2406–2417. (p. 25)

Garboczi, E. (2011). Three dimensional shape analysis of JSC-1A simulated Lunar regolith particles. *Powder Technology*, 207(1):96–103. (p. 24)

Garcia, X., Akanji, L., Blunt, M., Matthai, S., and Latham, J. (2009). Numerical study of the effects of particle shape and polydispersity on permeability. *Physical Review E*, 80(2):021304. (p. 3)

Gibson, S. (1998). Constrained elastic surface nets: Generating smooth surfaces from binary segmented data. In Wells, W., Colchester, A., and Delp, S., editors, *Medical Image Computing and Computer-Assisted Intervention-MICCAI'98*, volume 1496, pages 888–898. Springer, Berlin, Heidelberg. (p. 26)

Gilkes, R. and Suddhiprakarn, A. (1979). Biotite alteration in deeply weathered granite. I. morphological, mineralogical, and chemical properties. *Clays and Clay Minerals*, 27(5):349–360. (p. 23)

Gleaton, J., Xiao, R., Lai, Z., McDaniel, N., Johnstone, C., Burden, B., Chen, Q., and Zheng, Y. (2018). Biocementation of martian regolith simulant with in-situ resources. In *Proceedings of the ASCE Earth and Space 2018: Engineering for Extreme Environments*. ASCE. (p. 23)

Goda, T. and Ebert, F. (2005). Three-dimensional discrete element simulations in hoppers and silos. *Powder Technology*, 158(1-3):58–68. (p. 117)

González-Montellano, C., Ramirez, A., Gallego, E., and Ayuga, F. (2011). Validation and experimental calibration of 3D discrete element models for the simulation of the discharge flow in silos. *Chemical Engineering Science*, 66(21):5116–5126. (p. 118)

Gouache, T., Patel, N., Brunskill, C., Scott, G., Saaj, C., Matthews, M., and Cui, L. (2011). Soil simulant sourcing for the ExoMars rover testbed. *Planetary and Space Science*, 59(8):779–787. (p. 58)

Govender, N., Wilke, D., Kok, S., and Els, R. (2014). Development of a convex polyhedral discrete element simulation framework for NVIDIA Kepler based GPUs. *Journal of Computational and Applied Mathematics*, 270:386–400. (p. 74)

Guo, N. and Zhao, J. (2014). A coupled FEM/DEM approach for hierarchical multiscale modelling of granular media. *International Journal for Numerical Methods in Engineering*, 99(11):789–818. (p. 128)

Guo, N. and Zhao, J. (2016). Multiscale insights into classical geomechanics problems. *International Journal for Numerical and Analytical Methods in Geomechanics*, 40(3):367–390. (p. 7)

Guo, P. and Su, X. (2007). Shear strength, interparticle locking, and dilatancy of granular materials. *Canadian Geotechnical Journal*, 44(5):579–591. (p. 23)

Guo, Y., Wassgren, C., Curtis, J., and Xu, D. (2018). A bonded sphero-cylinder model for the discrete element simulation of elasto-plastic fibers. *Chemical Engineering Science*, 175:118–129. (p. 89, 121)

Guo, Y., Wassgren, C., Hancock, B., Ketterhagen, W., and Curtis, J. (2013). Validation and time step determination of discrete element modeling of flexible fibers. *Powder Technology*, 249:386–395. (p. 89)

Guo, Y., Wassgren, C., Hancock, B., Ketterhagen, W., and Curtis, J. (2015). Computational study of granular shear flows of dry flexible fibres using the discrete element method. *Journal of Fluid Mechanics*, 775:24–52. (p. 89, 120)

Hall, M., Frank, E., Holmes, G., Pfahringer, B., Reutemann, P., and Witten, I. (2009). The WEKA data mining software: an update. *ACM SIGKDD explorations newsletter*, 11(1):10–18. (p. 28)

Haralock, R. and Shapiro, L. (1991). *Computer and robot vision*. Addison-Wesley Longman Publishing Co., Inc. (p. 67)

Hart, R., Cundall, P., and Lemos, J. (1988). Formulation of a three-dimensional distinct element model–Part II. Mechanical calculations for motion and interaction of a system composed of many polyhedral blocks. *International Journal of Rock Mechanics and Mining Sciences & Geomechanics Abstracts*, 25(3):117–125. (p. 11)

Härtl, J. and Ooi, J. (2008). Experiments and simulations of direct shear tests: porosity, contact friction and bulk friction. *Granular Matter*, 10(4):263. (p. 125)

Härtl, J. and Ooi, J. (2011). Numerical investigation of particle shape and particle friction on limiting bulk friction in direct shear tests and comparison with experiments. *Powder Technology*, 212(1):231–239. (p. 71, 80, 83)

Hashemi, M., Khaddour, G., François, B., Massart, T., and Salager, S. (2014). A tomographic imagery segmentation methodology for three-phase geomaterials based on simultaneous region growing. *Acta Geotechnica*, 9(5):831–846. (p. 24, 25)

Hehar, G., Fasina, O., Adhikari, S., and Fulton, J. (2014). Ignition and volatilization behavior of dust from loblolly pine wood. *Fuel Processing Technology*, 127:117–123. (p. 110)

Hentschel, M. and Page, N. (2003). Selection of descriptors for particle shape characterization. *Particle & Particle Systems Characterization*, 20(1):25–38. (p. 39)

Hernandez, S., Westover, T., Matthews, A., Ryan, J., and Williams, L. (2017). Feeding properties and behavior of hammer-and knife-milled pine. *Powder Technology*, 320:191–201. (p. 86, 87, 94)

Hertz, H. (1882). Uber die Beruhrung fester elastischer Korper und Uber die Harte. *Verhandlung des Vereins zur Beforderung des GewerbefleiBes, Berlin*, page 449. (p. 8, 17, 93, 123)

Hobson, D., Carter, R., and Yan, Y. (2009). Rule based concave curvature segmentation for touching rice grains in binary digital images. In *2009 IEEE Instrumentation and Measurement Technology Conference*, pages 1685–1689. IEEE. (p. 25)

Höhner, D., Wirtz, S., and Scherer, V. (2012). A numerical study on the influence of particle shape on hopper discharge within the polyhedral and multi-sphere discrete element method. *Powder Technology*, 226:16–28. (p. 87, 89, 118)

Höhner, D., Wirtz, S., and Scherer, V. (2015). A study on the influence of particle shape on the mechanical interactions of granular media in a hopper using the discrete element method. *Powder Technology*, 278:286–305. (p. 89)

Hopkins, M., Johnson, J., and Sullivan, R. (2008). Discrete element modeling of a rover wheel in granular material under the influence of Earth, Mars, and Lunar gravity. In *Earth & Space 2008: Engineering, Science, Construction, and Operations in Challenging Environments*, pages 1–7. American Society of Civil Engineers. (p. 57)

Hopkins, M., Knuth, M., and Green, A. (2012). Discrete element method simulations of digging in JSC-1A. In *Earth and Space 2012: Engineering, Science, Construction, and Operations in Challenging Environments*, pages 65–73. American Society of Civil Engineers. (p. 57)

Horabik, J. and Molenda, M. (2014). Mechanical properties of granular materials and their impact on load distribution in silo: a review. *Scientia Agriculturae Bohemica*, 45(4):203–211. (p. 117)

Horabik, J. and Molenda, M. (2016). Parameters and contact models for DEM simulations of agricultural granular materials: a review. *Biosystems Engineering*, 147:206–225. (p. 88)

Iagnemma, K., Shibly, H., and Dubowsky, S. (2005). A laboratory single wheel testbed for studying planetary rover wheel-terrain interaction. *MIT field and space robotics laboratory Technical Report*, 1:05–05. (p. 57)

Igwe, O., Sassa, K., and Wang, F. (2007). The influence of grading on the shear strength of loose sands in stress-controlled ring shear tests. *Landslides*, 4(1):43. (p. 2)

Ilic, D., Williams, K., Farnish, R., Webb, E., and Liu, G. (2018). On the challenges facing the handling of solid biomass feedstocks. *Biofuels, Bioproducts and Biorefining*, 12(2):187–202. (p. 118)

Itasca Consulting Group, Inc (2014). PFC – Particle Flow Code, Ver. 5.0. Minneapolis: Itasca. (p. 9, 10, 14, 16, 77, 78, 91, 123)

Iwashita, K. and Oda, M. (1998). Rolling resistance at contacts in simulation of shear band development by DEM. *Journal of engineering mechanics*, 124(3):285–292. (p. 16, 72)

Jaccard, N. (2015). *Development of an image processing method for automated, non-invasive and scale-independent monitoring of adherent cell cultures*. PhD thesis, University College London. (p. x, 26, 30)

Jiang, M., Chen, H., and Crosta, G. (2015a). Numerical modeling of rock mechanical behavior and fracture propagation by a new bond contact model. *International Journal of Rock Mechanics and Mining Sciences*, 78:175–189. (p. 121)

Jiang, M., Jiang, T., Crosta, G., Shi, Z., Chen, H., and Zhang, N. (2015b). Modeling failure of jointed rock slope with two main joint sets using a novel DEM bond contact model. *Engineering Geology*, 193:79–96. (p. 121)

Jiang, M., Yu, H., and Harris, D. (2005). A novel discrete model for granular material incorporating rolling resistance. *Computers and Geotechnics*, 32(5):340–357. (p. 8, 16, 72)

Jiang, M., Zhu, F., Liu, F., and Utili, S. (2014). A bond contact model for methane hydrate-bearing sediments with interparticle cementation. *International Journal for Numerical and Analytical Methods in Geomechanics*, 38(17):1823–1854. (p. 121)

Johnson, J., Kulchitsky, A., Duvoy, P., Iagnemma, K., Senatore, C., Arvidson, R., and Moore, J. (2015). Discrete element method simulations of Mars Exploration Rover wheel performance. *Journal of Terramechanics*, 62:31–40. (p. 59)

Kawamoto, R., Andò, E., Viggiani, G., and Andrade, J. (2016). Level set discrete element method for three-dimensional computations with triaxial case study. *Journal of the Mechanics and Physics of Solids*, 91:1–13. (p. 13, 74)

Ketcham, R. and Carlson, W. (2001). Acquisition, optimization and interpretation of X-ray computed tomographic imagery: applications to the geosciences. *Computers & Geosciences*, 27(4):381–400. (p. 24)

Ketterhagen, W., Curtis, J., Wassgren, C., and Hancock, B. (2008). Modeling granular segregation in flow from quasi-three-dimensional, wedge-shaped hoppers. *Powder Technology*, 179(3):126–143. (p. 118)

Ketterhagen, W., Curtis, J., Wassgren, C., and Hancock, B. (2009). Predicting the flow mode from hoppers using the discrete element method. *Powder Technology*, 195(1):1–10. (p. 117)

Kim, B., Park, S., and Kato, S. (2012). DEM simulation of collapse behaviours of unsaturated granular materials under general stress states. *Computers and Geotechnics*, 42:52–61. (p. 73)

Kloss, C., Goniva, C., Hager, A., Amberger, S., and Pirker, S. (2012). Models, algorithms and validation for opensource DEM and CFD–DEM. *Progress in Computational Fluid Dynamics, an International Journal*, 12(2-3):140–152. (p. 14, 104, 123)

Knuth, M., Johnson, J., Hopkins, M., Sullivan, R., and Moore, J. (2012). Discrete element modeling of a Mars Exploration Rover wheel in granular material. *Journal of Terramechanics*, 49(1):27–36. (p. 59)

Kobyłka, R., Horabik, J., and Molenda, M. (2017). Numerical simulation of the dynamic response due to discharge initiation of the grain silo. *International Journal of Solids and Structures*, 106:27–37. (p. 118)

Kruggel-Emden, H., Rickelt, S., Wirtz, S., and Scherer, V. (2008). A study on the validity of the multi-sphere Discrete Element Method. *Powder Technology*, 188(2):153–165. (p. 88)

Kruggel-Emden, H., Sudbrock, F., Wirtz, S., and Scherer, V. (2012). Experimental and numerical investigation of the bulk behavior of wood pellets on a model type grate. *Granular Matter*, 14(6):681–693. (p. 89)

Lai, Z. and Chen, Q. (2017). Characterization and discrete element simulation of grading and shape-dependent behavior of JSC-1A Martian regolith simulant. *Granular Matter*, 19(4):69. (p. 24, 118, 132)

Langston, P., Kennedy, A., and Constantin, H. (2015). Discrete element modelling of flexible fibre packing. *Computational Materials Science*, 96:108–116. (p. 89, 120)

Leblicq, T., Smeets, B., Ramon, H., and Saeys, W. (2016a). A discrete element approach for modelling the compression of crop stems. *Computers and Electronics in Agriculture*, 123:80–88. (p. 89, 120)

Leblicq, T., Smeets, B., Vanmaercke, S., Ramon, H., and Saeys, W. (2016b). A discrete element approach for modelling bendable crop stems. *Computers and Electronics in Agriculture*, 124:141–149. (p. 89, 120)

Lenaerts, B., Aertsen, T., Tijskens, E., De Ketelaere, B., Ramon, H., De Baerdemaeker, J., and Saeys, W. (2014). Simulation of grain–straw separation by discrete element modeling with bendable straw particles. *Computers and Electronics in Agriculture*, 101:24–33. (p. 89, 120)

Li, C., Xu, C., Gui, C., and Fox, M. (2005a). Level set evolution without re-initialization: a new variational formulation. In *Computer Vision and Pattern Recognition, 2005. CVPR 2005. IEEE Computer Society Conference on*, volume 1, pages 430–436. IEEE. (p. 34, 35, 37)

Li, C., Xu, C., Gui, C., and Fox, M. (2010). Distance regularized level set evolution and its application to image segmentation. *IEEE Transactions on Image Processing*, 19(12):3243–3254. (p. 34, 35, 37, 44)

Li, G., Liu, Y.-J., Dano, C., and Hicher, P.-Y. (2014). Grading-dependent behavior of granular materials: from discrete to continuous modeling. *Journal of Engineering Mechanics*, 141(6):04014172. (p. 3)

Li, Y., Xu, Y., and Thornton, C. (2005b). A comparison of discrete element simulations and experiments for 'sandpiles' composed of spherical particles. *Powder Technology*, 160(3):219–228. (p. 11)

Lim, J. (1990). *Two-dimensional Signal and Image Processing*. Prentice-Hall, Inc., Upper Saddle River, NJ, USA. (p. 65)

Lin, X. and Ng, T. (1997). A three-dimensional discrete element model using arrays of ellipsoids. *Géotechnique*, 47(2):319–329. (p. 13)

Liu, P. and Hrenya, C. (2014). Challenges of DEM: I. Competing bottlenecks in parallelization of gas–solid flows. *Powder Technology*, 264:620–626. (p. 7)

Liu, S., Zhou, Z., Zou, R., Pinson, D., and Yu, A. (2014a). Flow characteristics and discharge rate of ellipsoidal particles in a flat bottom hopper. *Powder Technology*, 253:70–79. (p. 118)

Liu, Y., Captur, G., Moon, J., Guo, S., Yang, X., Zhang, S., and Li, C. (2016). Distance regularized two level sets for segmentation of left and right ventricles from cine-MRI. *Magnetic Resonance Imaging*, 34(5):699–706. (p. 26)

Liu, Y.-J., Li, G., Yin, Z.-Y., Dano, C., Hicher, P.-Y., Xia, X.-H., and Wang, J.-H. (2014b). Influence of grading on the undrained behavior of granular materials. *Comptes Rendus Mécanique*, 342(2):85–95. (p. 3)

Lombardot, B. (2017). Interactive H-Watershed. `https://imagej.net/Interactive_Watershed`. Accessed: 2018-04-30. (p. 47)

Lorensen, W. and Cline, H. (1987). Marching cubes: a high resolution 3D surface construction algorithm. In *Proceedings of the 14th Annual Conference on Computer Graphics and Interactive Techniques*, SIGGRAPH '87, pages 163–169, New York, USA. ACM. (p. 26, 44)

Lu, M. and McDowell, G. (2007). The importance of modelling ballast particle shape in the discrete element method. *Granular matter*, 9(1-2):69. (p. 127)

Luding, S. (2005a). Anisotropy in cohesive, frictional granular media. *Journal of Physics: Condensed Matter*, 17(24):S2623. (p. 114, 151)

Luding, S. (2005b). Shear flow modeling of cohesive and frictional fine powder. *Powder Technology*, 158(1-3):45–50. (p. 114, 151)

Luding, S. (2008). Cohesive, frictional powders: contact models for tension. *Granular matter*, 10(4):235–246. (p. 17, 73)

Luerkens, D., Beddow, J., and Vetter, A. (1982). Morphological fourier descriptors. *Powder Technology*, 31(2):209–215. (p. 45)

Ma, H., Xu, L., and Zhao, Y. (2017). CFD-DEM simulation of fluidization of rod-like particles in a fluidized bed. *Powder Technology*, 314:355–366. (p. 88)

Mack, S., Langston, P., Webb, C., and York, T. (2011). Experimental validation of polyhedral discrete element model. *Powder Technology*, 214(3):431–442. (p. 74)

Madra, A., El Hajj, N., and Benzeggagh, M. (2014). X-ray microtomography applications for quantitative and qualitative analysis of porosity in woven glass fiber reinforced thermoplastic. *Composites Science and Technology*, 95:50–58. (p. 49)

Maione, R., De Richter, S., Mauviel, G., and Wild, G. (2015). DEM investigation of granular flow and binary mixture segregation in a rotating tumbler: Influence of particle shape and internal baffles. *Powder Technology*, 286:732–739. (p. 88, 89)

Maione, R., De Richter, S., Mauviel, G., and Wild, G. (2017). Axial segregation of a binary mixture in a rotating tumbler with non-spherical particles: experiments and DEM model validation. *Powder Technology*, 306:120–129. (p. 89)

Mani, S., Tabil, L., Sokhansanj, S., and Roberge, M. (2003). Mechanical properties of corn stover grind. In *2003 ASAE Annual Meeting*, page 1. American Society of Agricultural and Biological Engineers. (p. 119)

Masson, S. and Martinez, J. (2000). Effect of particle mechanical properties on silo flow and stresses from distinct element simulations. *Powder Technology*, 109(1-3):164–178. (p. 117, 118)

Matsushima, T., Katagiri, J., Uesugi, K., Tsuchiyama, A., and Nakano, T. (2009). 3D shape characterization and image-based DEM simulation of the lunar soil simulant FJS-1. *Journal of Aerospace Engineering*, 22(1):15–23. (p. 24, 25, 47)

Meijering, E. (2012). Cell segmentation: 50 years down the road [life sciences]. *IEEE Signal Processing Magazine*, 29(5):140–145. (p. 25)

Meyer, F. (1994). Topographic distance and watershed lines. *Signal processing*, 38(1):113–125. (p. 67)

Mindlin, R. (1953). Elastic spheres in contact under varying oblique forces. *Journal of Applied Mechanics*, 20:327–344. (p. 8, 17, 93, 123)

Mollon, G. and Zhao, J. (2012). Fourier–Voronoi-based generation of realistic samples for discrete modelling of granular materials. *Granular Matter*, 14(5):621–638. (p. 69)

Mollon, G. and Zhao, J. (2013a). Characterization of fluctuations in granular hopper flow. *Granular Matter*, 15(6):827–840. (p. 118, 128, 136)

Mollon, G. and Zhao, J. (2013b). Generating realistic 3D sand particles using Fourier descriptors. *Granular Matter*, 15(1):95–108. (p. 24)

Moses, R. and Bushnell, D. (2016). Frontier In-Situ Resource Utilization for Enabling Sustained Human Presence on Mars. Technical Report NASA-TM-2016-219182, NASA Langley Research Center. (p. 57)

Nassauer, B., Liedke, T., and Kuna, M. (2013). Polyhedral particles for the discrete element method. *Granular Matter*, 15(1):85–93. (p. 13)

Nedderman, R. (1992). *Statics and kinematics of granular materials*. Cambridge University Press, Cambridge. (p. 133, 135, 138, 145, 146)

Oevermann, M., Gerber, S., and Behrendt, F. (2009). Euler–Lagrange/DEM simulation of wood gasification in a bubbling fluidized bed reactor. *Particuology*, 7(4):307–316. (p. 89)

Office, B. T. (2016). Strategic plan for a thriving and sustainable bioeconomy. Technical report, U.S. Department of Energy Bioenergy Technologies Office. (p. 86)

Olatunde, G., Fasina, O., Adhikari, S., McDonald, T., and Duke, S. (2016). Size measurement method for Loblolly Pine grinds and influence on predictability of fluidization. *Canadian Biosystems Engineering*, 58. (p. 110)

Olson, E. (2011). Particle shape factors and their use in image analysis-part 1: Theory. *Journal of GXP Compliance*, 15(3):85. (p. 70)

Osher, S. and Sethian, J. (1988). Fronts propagating with curvature-dependent speed: algorithms based on Hamilton-Jacobi formulations. *Journal of Computational Physics*, 79(1):12–49. (p. 34)

O'Sullivan, C. (2011). Particle-based discrete element modeling: geomechanics perspective. *International Journal of Geomechanics*, 11(6):449–464. (p. 6)

Otsubo, M., O'Sullivan, C., and Shire, T. (2017). Empirical assessment of the critical time increment in explicit particulate discrete element method simulations. *Computers and Geotechnics*, 86:67–79. (p. 10, 11)

Papoulis, D., Tsolis-Katagas, P., and Katagas, C. (2004). Progressive stages in the formation of kaolin minerals of different morphologies in the weathering of plagioclase. *Clays and Clay Minerals*, 52(3):275–286. (p. 23)

Peters, G., Abbey, W., Bearman, G., Mungas, G., Smith, J., Anderson, R., Douglas, S., and Beegle, L. (2008). Mojave Mars simulant - Characterization of a new geologic Mars analog. *Icarus*, 197(2):470–479. (p. 41, 58)

Peters, J., Hopkins, M., Kala, R., and Wahl, R. (2009). A poly-ellipsoid particle for non-spherical discrete element method. *Engineering Computations*, 26(6):645–657. (p. 13)

Plassiard, J.-P., Belheine, N., and Donzé, F.-V. (2009). A spherical discrete element model: calibration procedure and incremental response. *Granular Matter*, 11(5):293–306. (p. 20, 78, 124)

Podlozhnyuk, A., Pirker, S., and Kloss, C. (2017). Efficient implementation of superquadric particles in discrete element method within an open-source framework. *Computational Particle Mechanics*, 4(1):101–118. (p. 13)

Potyondy, D. and Cundall, P. (2004). A bonded-particle model for rock. *International Journal of Rock Mechanics and Mining Sciences*, 41(8):1329–1364. (p. 8, 19, 92, 93, 120, 121)

Powers, M. (1953). A new roundness scale for sedimentary particles. *Journal of Sedimentary Research*, 23(2):117–119. (p. xi, 52, 53)

Quinlan, J. (1986). Induction of decision trees. *Machine learning*, 1(1):81–106. (p. 28)

Rackl, M., Top, F., Molhoek, C., and Schott, D. (2017). Feeding system for wood chips: A DEM study to improve equipment performance. *Biomass and Bioenergy*, 98:43–52. (p. 88)

Redding, T., Hannam, K., Quideau, S., and Devito, K. (2005). Particle density of aspen, spruce, and pine forest floors in Alberta, Canada. *Soil Science Society of America Journal*, 69(5):1503–1506. (p. 110)

Rosin, P. and Rammler, E. (1933). The laws governing the fineness of powdered coal. *Journal of the Institute of Fuel*, 7:29–36. (p. 63)

Rousé, P., Fannin, R., and Shuttle, D. (2008). Influence of roundness on the void ratio and strength of uniform sand. *Géotechnique*, 58(3):227–231. (p. 2)

Santamarina, J. and Cho, G. (2004). Soil behaviour: The role of particle shape. In *Advances in geotechnical engineering: The skempton conference*, volume 1, pages 604–617. Citeseer. (p. 2, 23)

Scherer, V., Mönnigmann, M., Berner, M., and Sudbrock, F. (2016). Coupled DEM–CFD simulation of drying wood chips in a rotary drum–baffle design and model reduction. *Fuel*, 184:896–904. (p. 88, 89)

Schott, D., Tans, R., Dafnomilis, I., Hancock, V., and Lodewijks, G. (2016). Assessing a durability test for wood pellets by discrete element simulation. *FME Transactions*, 44:279–284. (p. 89)

Schulze, D. (2008). *Powders and bulk solids*. Springer, Heidelberg, Germany. (p. 20)

Scott, A., Oze, C., Tang, Y., and O'Loughlin, A. (2017). Development of a Martian regolith simulant for in-situ resource utilization testing. *Acta Astronautica*, 131:45–49. (p. 58)

Semnani, S. and Borja, R. (2017). Quantifying the heterogeneity of shale through statistical combination of imaging across scales. *Acta Geotechnica*, 12(6):1193–1205. (p. 46)

Sen, S., Carranza, S., and Pillay, S. (2010). Multifunctional Martian habitat composite material synthesized from in situ resources. *Advances in Space Research*, 46(5):582–592. (p. 57)

Sezgin, M. and Sankur, B. (2004). Survey over image thresholding techniques and quantitative performance evaluation. *Journal of Electronic imaging*, 13(1):146–168. (p. 24)

Shi, C., Li, D., Xu, W., and Wang, R. (2015). Discrete element cluster modeling of complex mesoscopic particles for use with the particle flow code method. *Granular Matter*, 17(3):377–387. (p. x, xi, 13, 14, 74, 75)

Simoni, A. and Houlsby, G. (2006). The direct shear strength and dilatancy of sand–gravel mixtures. *Geotechnical & Geological Engineering*, 24(3):523–549. (p. 62)

Sitharam, T. and Nimbkar, M. (2000). Micromechanical modelling of granular materials: effect of particle size and gradation. *Geotechnical & Geological Engineering*, 18(2):91–117. (p. 2)

Sleutel, S., Cnudde, V., Masschaele, B., Vlassenbroek, J., Dierick, M., Van Hoorebeke, L., Jacobs, P., and De Neve, S. (2008). Comparison of different nano-and micro-focus X-ray computed tomography set-ups for the visualization of the soil microstructure and soil organic matter. *Computers & Geosciences*, 34(8):931–938. (p. 25)

Smith, W. and Peng, H. (2013). Modeling of wheel–soil interaction over rough terrain using the discrete element method. *Journal of Terramechanics*, 50(5):277–287. (p. 59)

Soille, P. (2013). *Morphological image analysis: principles and applications*. Springer Science & Business Media. (p. 64)

Sommer, C. and Gerlich, D. (2013). Machine learning in cell biology–teaching computers to recognize phenotypes. *Journal of Cell Science*, 126(24):5529–5539. (p. 26)

Stark, N., Hay, A., Cheel, R., and Lake, C. (2014). The impact of particle shape on the angle of internal friction and the implications for sediment dynamics at a steep, mixed sand-gravel beach. *Earth Surface Dynamics*, 2(2):469–480. (p. 23)

Stasiak, M., Molenda, M., Bańda, M., and Gondek, E. (2015). Mechanical properties of sawdust and woodchips. *Fuel*, 159:900–908. (p. 86, 119)

Stukowski, A. (2009). Visualization and analysis of atomistic simulation data with OVITO–the Open Visualization Tool. *Modelling and Simulation in Materials Science and Engineering*, 18(1):015012. (p. 100)

Sullivan, R., Anderson, R., Biesiadecki, J., Bond, T., and Stewart, H. (2011). Cohesions, friction angles, and other physical properties of Martian regolith from Mars Exploration Rover wheel trenches and wheel scuffs. *Journal of Geophysical Research: Planets*, 116(E2). E02006. (p. 57)

Sun, W., Andrade, J., and Rudnicki, J. (2011a). Multiscale method for characterization of porous microstructures and their impact on macroscopic effective permeability. *International Journal for Numerical Methods in Engineering*, 88(12):1260–1279. (p. 35)

Sun, W., Andrade, J., Rudnicki, J., and Eichhubl, P. (2011b). Connecting microstructural attributes and permeability from 3d tomographic images of in situ shear-enhanced compaction bands using multiscale computations. *Geophysical Research Letters*, 38(10). (p. 35)

Tagliaferri, F., Waller, J., Andò, E., Hall, S., Viggiani, G., Bésuelle, P., and DeJong, J. (2011). Observing strain localisation processes in bio-cemented sand using X-ray imaging. *Granular Matter*, 13(3):247–250. (p. 23)

Thornton, C. (2000). Numerical simulations of deviatoric shear deformation of granular media. *Géotechnique*, 50(1):43–53. (p. 11)

Tijskens, E., Ramon, H., and De Baerdemaeker, J. (2003). Discrete element modelling for process simulation in agriculture. *Journal of sound and vibration*, 266(3):493–514. (p. 6)

Ting, J., Khwaja, M., Meachum, L., and Rowell, J. (1993). An ellipse-based discrete element model for granular materials. *International Journal for Numerical and Analytical Methods in Geomechanics*, 17(9):603–623. (p. 13)

Torskaya, T., Shabro, V., Torres-Verdín, C., Salazar-Tio, R., and Revil, A. (2014). Grain shape effects on permeability, formation factor, and capillary pressure from pore-scale modeling. *Transport in porous media*, 102(1):71–90. (p. 3)

Tsomokos, A. and Georgiannou, V. (2010). Effect of grain shape and angularity on the undrained response of fine sands. *Canadian Geotechnical Journal*, 47(5):539–551. (p. 23)

Tu, X., Andrade, J., and Chen, Q. (2009). Return mapping for nonsmooth and multiscale elastoplasticity. *Computer Methods in Applied Mechanics and Engineering*, 198(30):2286–2296. (p. 57)

Vangla, P. and Latha, G. (2015). Influence of particle size on the friction and interfacial shear strength of sands of similar morphology. *International Journal of Geosynthetics and Ground Engineering*, 1(1):6. (p. 2)

Verlet, L. (1967). Computer "experiments" on classical fluids. I. thermodynamical properties of Lennard-Jones molecules. *Physical Review*, 159(1):98. (p. 9, 92, 122)

Viggiani, G., Andò, E., Takano, D., and Santamarina, J. (2015). Laboratory X-ray tomography: a valuable experimental tool for revealing processes in soils. *Geotechnical Testing Journal*, 38(1):61–71. (p. 24)

Vincent, L. and Soille, P. (1991). Watersheds in digital spaces: an efficient algorithm based on immersion simulations. *IEEE Transactions on Pattern Analysis & Machine Intelligence*, 13(6):583–598. (p. 47)

Vlahinić, I., Andò, E., Viggiani, G., and Andrade, J. (2014). Towards a more accurate characterization of granular media: extracting quantitative descriptors from tomographic images. *Granular Matter*, 16(1):9–21. (p. 24, 25)

Wadell, H. (1933). Sphericity and roundness of rock particles. *The Journal of Geology*, 41(3):310–331. (p. 40, 41)

Walker, D. (1966). An approximate theory for pressures and arching in hoppers. *Chemical Engineering Science*, 21(11):975–997. (p. 131, 133, 135, 144, 145)

Wan, J., Wang, F., Yang, G., Zhang, S., Wang, M., Lin, P., and Yang, L. (2018). The influence of orifice shape on the flow rate: A DEM and experimental research in 3D hopper granular flows. *Powder Technology*, 335:147–155. (p. 118)

Wan, L., Wendner, R., and Cusatis, G. (2016). A novel material for in situ construction on Mars: experiments and numerical simulations. *Construction and Building Materials*, 120:222–231. (p. 57)

Wang, H., Zhang, H., and Ray, N. (2012). Clump splitting via bottleneck detection and shape classification. *Pattern Recognition*, 45(7):2780–2787. (p. 25)

Wang, Y., Alonso-Marroquin, F., Xue, S., and Xie, J. (2015). Revisiting rolling and sliding in two-dimensional discrete element models. *Particuology*, 18:35–41. (p. 17, 73)

Wang, Z., Jacobs, F., and Ziegler, M. (2014a). Visualization of load transfer behaviour between geogrid and sand using PFC^{2D}. *Geotextiles and Geomembranes*, 42(2):83–90. (p. 73, 79)

Wang, Z., Ruiken, A., Jacobs, F., and Ziegler, M. (2014b). A new suggestion for determining 2D porosities in DEM studies. *Geomechanics and Engineering*, 7(6):665–678. (p. 77)

Weerasekara, N., Powell, M., Cleary, P., Tavares, L., Evertsson, M., Morrison, R., Quist, J., and Carvalho, R. (2013). The contribution of DEM to the science of comminution. *Powder Technology*, 248:3–24. (p. 88)

Wensrich, C. and Katterfeld, A. (2012). Rolling friction as a technique for modelling particle shape in DEM. *Powder Technology*, 217:409–417. (p. 88)

Westover, T. and Hartley, D. (2018). Biomass Handling and Feeding. In Nageswara-Rao, M. and Soneji, J. R., editors, *Advances in Biofuels and Bioenergy*, chapter 6. IntechOpen, Rijeka. (p. 86)

Westover, T., Phanphanich, M., and Ryan, J. (2015). Comprehensive rheological characterization of chopped and ground switchgrass. *Biofuels*, 6(5-6):249–260. (p. xiii, 118, 126)

Westover, T., Xia, Y., and Klinger, J. (2018). Understanding and solving biomass feeding and handling challenges. *Agricultural Research & Technology: Open Access Journal*, 16(2):001–003. (p. 115, 118)

Williams, J. and Pentland, A. (1992). Superquadrics and modal dynamics for discrete elements in interactive design. *Engineering Computations*, 9(2):115–127. (p. 13)

Wood, D. and Maeda, K. (2008). Changing grading of soil: effect on critical states. *Acta Geotechnica*, 3(1):3. (p. 3)

Wu, M., Schott, D., and Lodewijks, G. (2011). Physical properties of solid biomass. *Biomass and Bioenergy*, 35(5):2093–2105. (p. 119)

Xu, P., Duan, X., Qian, G., and Zhou, X. (2015). Dependence of wall stress ratio on wall friction coefficient during the discharging of a 3d rectangular hopper. *Powder Technology*, 284:326–335. (p. 118)

Yu, Y. and Saxén, H. (2011). Discrete element method simulation of properties of a 3D conical hopper with mono-sized spheres. *Advanced Powder Technology*, 22(3):324–331. (p. 118)

Yu, Y. and Saxén, H. (2014). Segregation behavior of particles in a top hopper of a blast furnace. *Powder Technology*, 262:233–241. (p. 118)

Zeng, X., Li, X., Wang, S., Li, S., Spring, N., Tang, H., Li, Y., and Feng, J. (2015). JMSS-1: a new Martian soil simulant. *Earth, Planets and Space*, 67(1):1–10. (p. 58)

Zhang, B., Regueiro, R., Druckrey, A., and Alshibli, K. (2018a). Construction of poly-ellipsoidal grain shapes from SMT imaging on sand, and the development of a new DEM contact detection algorithm. *Engineering Computations*, 35(2):733–771. (p. 13)

Zhang, Y., Jia, F., Zeng, Y., Han, Y., and Xiao, Y. (2018b). DEM study in the critical height of flow mechanism transition in a conical silo. *Powder Technology*, 331:98–106. (p. 117)

Zhao, B. and Wang, J. (2016). 3D quantitative shape analysis on form, roundness, and compactness with μCT. *Powder Technology*, 291:262–275. (p. 26)

Zhao, S., Evans, T., and Zhou, X. (2018a). Effects of curvature-related DEM contact model on the macro-and micro-mechanical behaviours of granular soils. *Géotechnique*, 17:158. (p. 21)

Zhao, Y., Yang, S., Zhang, L., and Chew, J. (2018b). DEM study on the discharge characteristics of lognormal particle size distributions from a conical hopper. *AIChE Journal*, 64(4):1174–1190. (p. 118)

Zheng, J. and Hryciw, R. (2016). Segmentation of contacting soil particles in images by modified watershed analysis. *Computers and Geotechnics*, 73:142–152. (p. 47)

Zheng, J. and Hryciw, R. (2017a). An image based clump library for DEM simulations. *Granular Matter*, 2(19):26. (p. 24)

Zheng, J. and Hryciw, R. (2017b). Soil particle size and shape distributions by stereophotography and image analysis. *Geotechnical Testing Journal*, 40(2):317–328. (p. 24)

Zheng, J., Hryciw, R., and Ventola, A. (2017). Compressibility of sands of various geologic origins at pre-crushing stress levels. *Geotechnical and Geological Engineering*, 35(5):2037–2051. (p. 23)

Zhong, W., Yu, A., Liu, X., Tong, Z., and Zhang, H. (2016). DEM/CFD-DEM modelling of non-spherical particulate systems: theoretical developments and applications. *Powder Technology*, 302:108–152. (p. 7, 12, 88)

Zhou, B., Wang, J., and Wang, H. (2018). Three-dimensional sphericity, roundness and fractal dimension of sand particles. *Géotechnique*, 68(1):18–30. (p. 24, 41, 51)

Zhou, W., Yang, L., Ma, G., Chang, X., Lai, Z., and Xu, K. (2016). Dem analysis of the size effects on the behavior of crushable granular materials. *Granular Matter*, 18(3):64. (p. 3)

Zhu, H., Yu, A., and Wu, Y. (2006). Numerical investigation of steady and unsteady state hopper flows. *Powder Technology*, 170(3):125–134. (p. 117)

Zhu, H., Zhou, Z., Yang, R., and Yu, A. (2008). Discrete particle simulation of particulate systems: a review of major applications and findings. *Chemical Engineering Science*, 63(23):5728–5770. (p. 87)

Zuiderveld, K. (1994). Contrast Limited Adaptive Histogram Equalization. In Heckbert, P. S., editor, *Graphics Gems IV*, pages 474–485. Academic Press Professional, Inc., San Diego, CA, USA. (p. 65)

Vita - Zhengshou Lai

Education

- Ph.D., Civil Engineering, Clemson University, SC, USA. December 2018.
- Ph.D. candidate, Engineering Mechanics, Sun Yat-sen University, Guangdong, China. April 2014.
- B.Sc., Civil Transportation Engineering, Sun Yat-sen University, Guangdong, China. June 2012.

Publications

1. **Lai, Z.** & Chen, Q. Reconstructing granular particles from X-ray computed tomography using the TWS machine learning tool and the level set method. *Acta Geotechnica*. Accepted.

2. Chen, Q. & **Lai, Z.** (2018). Hydromechanical modeling of CO_2 sequestration using a component-based multiphysics code. *Environmental Geotechnics*. Accepted.

3. **Lai, Z.** & Chen, Q. (2017). Characterization and discrete element simulation of grading and shape-dependent behavior of JSC-1A Martian regolith simulant. *Granular Matter*, 19(4), 69.

4. **Lai, Z.** & Chen, Q. (2017). Particle swarm optimization for numerical bifurcation analysis in computational inelasticity. *International Journal for Numerical and Analytical Methods in Geomechanics*, 41(3), 442-468.

5. Mota, A., Chen, Q., Foulk, J., Ostien, J., & **Lai, Z.** (2016). A Cartesian parametrization for the numerical analysis of material instability. *International Journal for Numerical Methods in Engineering*, 108(2), 156-180.

6. **Lai, Z.**, Chen, Q., Wang, C., & Zhou, X. Modeling dynamic responses of heterogeneous seabed with embedded pipeline through multiresolution random field and coupled hydromechanical simulations. In review.

7. Xia, Y., **Lai, Z.**, Westover, T., Klinger, J., Huang, H., and Chen, Q. Discrete element modeling of deformable pinewood chips in cyclic loading test. In review.

8. **Lai, Z.**, Xia, Y., Huang, H., Westover, T., and Chen, Q. Discrete element modeling the granular hopper flow of deformable-irregular particles. In review.

9. Chen, Q., **Lai, Z.**, Moysey, S., & Shen, M. (2018). Image-based shape characterization and three-dimensional discrete element modeling of a granular Martian regolith simulant. In *GeoShanghai International Conference 2018*. Shanghai, China.

10. Chen, Q., Wang, C., **Lai, Z.**, & Juang, C. (2018). Integration of heterogeneous data for multiscale regional liquefaction settlement mapping. In *Proceedings of the Geotechnical Earthquake Engineering and Soil Dynamics V 2018*. Austin, Texas, USA.

11. Gleaton, J., Xiao, R., **Lai, Z.**, McDaniel, N., Johnstone, C.A., Burden, B., Chen, Q., & Zheng, Y. (2018). Biocementation of Martian Regolith with In-Situ Resources. In *2018 ASCE Earth and Space Conference*. Cleveland, Ohio, USA.

12. **Lai, Z.** & Chen, Q. (2018). Discrete element modeling of Martian regolith simulants accounting for realistic particle shapes and particle size distributions. In *2018 ASCE Earth and Space Conference*. Cleveland, Ohio, USA.

13. Shukla, S., Agnihotri1, S., **Lai, Z.**, Kousaalya, A., Pilla, S., & Chen, Q. (2018). Creation and characterization of regolith-based functional blocks with simulated in-situ Martian materials. In *2018 ASCE Earth and Space Conference*. Cleveland, Ohio, USA.